UNIVERSITY OF CALIFORNIA, SAN DIEGO

Dense Water Formation

on the Northwestern Shelf of the Okhotsk Sea

A dissertation submitted in partial satisfaction of the

requirements for the degree Doctor of Philosophy

in Oceanography

by

Andrey Shcherbina

Committee in charge:

Lynne D. Talley, Chair
David M. Checkley
Bruce D. Cornuelle
Daniel L. Rudnick
Sutanu Sarkar
Detlef B. Stammer

2004

The dissertation of Andrey Shcherbina is approved, and it is acceptable in quality and form for publication on microfilm:

_____

_____

_____

_____

_____

_____

Chair

University of California, San Diego

2004

TABLE OF CONTENTS

LIST OF FIGURES AND TABLES

ACKNOWLEDGEMENTS

I owe a great deal to colleagues, mentors, and fellow students who, through their own research, comments and questions have encouraged, supported and inspired me. My biggest thanks go to Lynne Talley and Daniel Rudnick who conceived and carried out the experimental part of the Okhotsk Sea shelf project and thus built a solid foundation for the research covered by this thesis. I also thank them for their continuous guidance and support throughout my work on this project. It was my privilege to have Lynne as my graduate advisor. She gave me all the freedom I could hope for in pursuing my ideas, while providing unfailing support and encouragement. I am also tremendously indebted to her for the care and patience with which she reviewed all of my manuscripts, including this thesis.

The modeling part of this work would not have been possible without the generous help from D. Haidvogel and H. Arango, who taught me the art of numerical modeling using the Regional Oceanic Modeling System and answered my numerous questions. I am also grateful to Emanuele Di Lorenzo for his patience and encouragement during our endless discussions on the subtleties of the numerical modeling.

I sincerely appreciate all the help, guidance and constructive critique from the members of my doctoral committee: David Checkley, Bruce Cornuelle, Sutanu Sarkar, and Detlef Stammer.

Many thanks to C. Winant, S. Gladyshev, K. Ohshima, S. Martin, M. Visbeck, P. Spain, and S. Maier for insightful discussion of the various aspects of this project.

To all the above individuals, and to many others who has helped me along the way and whose names would be impossible to list here, I feel very much indebted.

This work was supported in part through the National Science Foundation grant OCE-9811958 and by Hokkaido University (ship support). Technical support was provided by the Oceanographic Data Facility and the Instrument Development Group at Scripps Institution of Oceanography (SIO), and by the captain and crew of the R/V Professor Khromov.

The text of Chapter I, in full, is a reprint of the material as it appears in Shcherbina, A. Y., L. D. Talley, and D. L. Rudnick, 2004: Dense water formation on the northwestern shelf of the Okhotsk Sea: 1. Direct observations of brine rejection, *J. Geophys. Res.*, **109**, C09S08, doi:10.1029/2003JC002196. The dissertation author was the primary researcher and author, and the co-authors listed in this publication directed and supervised the research which forms the basis for this chapter.

The text of Chapter II, in full, is a reprint of the material as it appears in Shcherbina, A. Y., L. D. Talley, and D. L. Rudnick, 2004: Dense water formation on the northwestern shelf of the Okhotsk Sea: 2. Quantifying the transports, *J. Geophys. Res.*, **109**, C09S09, doi:10.1029/2003JC002197. The dissertation author was the primary researcher and author, and the co-authors listed in this publication directed and supervised the research which forms the basis for this chapter.

The text of Chapter V, in full, is a reprint of the material as it appears in Shcherbina, A. Y., L. D. Talley, and D. L. Rudnick, Ice-Draft Profiling from Moored ADCP Data, *J. Atmos. Ocean. Tech.*, (submitted). The dissertation author was the primary researcher and author, and the co-authors listed in this publication directed and supervised the research which forms the basis for this chapter.

VITA

1995-1998	Research Assistant, Moscow Institute of Physics and Technology, Moscow, Russia
1998	M.S., Moscow Institute of Physics and Technology, Moscow, Russia
1998-2004	Graduate Student Researcher, Scripps Institution of Oceanography, University of California, San Diego
2004	Ph.D., Scripps Institution of Oceanography, University of California, San Diego

PUBLICATIONS

Shcherbina, A. Y., L. D. Talley, and D. L. Rudnick. Dense water formation on the northwestern shelf of the Okhotsk Sea: 1. Direct observations of brine rejection, *J. Geophys. Res.*, 109, C09S08, doi:10.1029/2003JC002196, 2004.

Shcherbina, A. Y., L. D. Talley, and D. L. Rudnick. Dense water formation on the northwestern shelf of the Okhotsk Sea: 2. Quantifying the transports, *J. Geophys. Res.*, 109, C09S09, doi:10.1029/2003JC002197, 2004.

Shcherbina, A. Y., L. D. Talley, and D. L. Rudnick. Direct Observations of North Pacific Ventilation: Brine Rejection in the Okhotsk Sea, *Science* 302(5652), 1952-1955, 2003.

Shcherbina, A.Y., L. D. Talley, E. Firing, and P. Hacker. Near-Surface Frontal Zone Trapping and Deep Upward Propagation of Internal Wave Energy in the Japan/East Sea. *Journal of Phys. Oceanogr*. 33, 900-912, 2003.

Maksimenko, N. A., A. Y. Shcherbina, R. I. Gus'kina, and A. I. Kharlamov. Spatial structure and dynamics of the Northwest Pacific Intermediate Water, *Okeanologiya* [*Oceanology.*], 37(6), 805-811, 1997.

Maksimenko, N. A. and A. Y. Shcherbina. Fine structure of intermediate water in the north-west Pacific, *Meteorologiya I Gidrologiya* [*Meteorology and Hydrology.*], 7, 71-77, 1996.

Shcherbina, A. Y. and L. D. Talley. Direct observations of the current structure in the Japan/East Sea. CREAMS 2000, Vladivostok, extended abstract, 2000.

Maximenko N.A. and A. Y. Shcherbina. Fine-structure of the North Pacific Intermediate Water layer. Proceedings of the Workshop on the Okhotsk Sea and Adjacent Areas, PICES Scientific Report No.6, 104-110, 1996.

ABSTRACT OF THE DISSERTATION

Dense Water Formation

on the Northwestern Shelf of the Okhotsk Sea

by

Andrey Shcherbina

Doctor of Philosophy in Oceanography

University of California, San Diego, 2004

Professor Lynne D. Talley, Chair

The present study investigates formation, evolution and export of Okhotsk Sea Dense Shelf Water (DSW) using in-situ mooring and hydrographic observations combined with remote sensing and process-oriented numerical modeling.

Direct wintertime observations made by a bottom mooring array during 1999-2000 confirmed that the brine rejection associated with ice formation in a coastal polynya is a primary mechanism of DSW ventilation. The relatively fresh water inshore of the tidal mixing front was the precursor of the DSW, aided by the late-autumn offshore transition of the front. A steady salinity and density increase continued for over a month, with the maximum density σ_θ=26.92 kg m^{-3} reached during this period. The density increase terminated abruptly in late February possibly due to the onset of baroclinic instability of the density front at the polynya edge.

An estimated 8.6×10^{12} m^3 of DSW was formed during the winter of 1999-2000 (annual production rate of 0.3 Sv). The export rate of DSW from the formation region

varied seasonally from negligibly small in autumn, to 0.75 Sv in winter, with the mean export rate of 0.27 Sv.

The tidal bottom boundary layer structure on the northwestern shelf of the Okhotsk Sea is investigated using the acoustic Doppler current Profiler (ADCP) data. Clear Ekman spiraling is evident in rotary tidal components at M_2 tidal frequency. Vertical and temporal variations of vertical eddy viscosity coefficient are inferred from the parameters of this spiraling.

Processes of formation and evolution of tidal mixing front, as well as wintertime DSW formation are studied using a range of analytical and numerical models. Special attention is given to reproduction and interpretation of the observed structure of the tidal mixing front. The observations of wintertime internal tide intensification and eddy diffusivity decrease are also reproduced.

A procedure for ice-draft profiling using an upward-looking ADCP is developed. The effects of atmospheric pressure changes, sound speed variation, finite instrument beamwidth, hardware signal processing, instrument tilt, beam misalignment and vertical sensor offset are quantified. The developed algorithms are tested using the data from the winter-long ADCP deployment on the northwestern shelf of the Okhotsk Sea.

CHAPTER I

Direct Observations of Brine Rejection

The text of this chapter, in full, is a reprint of the material as it appears in Shcherbina, A. Y., L. D. Talley, and D. L. Rudnick. Dense water formation on the northwestern shelf of the Okhotsk Sea: 1. Direct observations of brine rejection, *J. Geophys. Res.*, 109, C09S08, doi:10.1029/2003JC002196, 2004. The dissertation author was the primary researcher and author, and the co-authors listed in this publication directed and supervised the research which forms the basis for this chapter.

Abstract. Dense Shelf Water (DSW) formation due to brine rejection in the coastal polynya on the northwestern shelf of the Okhotsk Sea was studied using two bottom moorings during the winter of 1999-2000. A steady salinity and density increase that continued for over a month was observed at the shallower mooring. The maximum density of σ_θ=26.92 kg m^{-3} was reached during this period. The density increase terminated abruptly in late February while the active brine rejection continued for several more weeks based on indirect evidence from water properties and ice cover. This termination was possibly due to the onset of baroclinic instability of the density front at the polynya edge facilitating offshore eddy transport of the density anomaly. Observed periodic baroclinic tide intensification events are hypothesized to be an indicator of the presence of such baroclinic eddies. No significant density increase was observed at the deeper, offshore mooring, indicating a robust demarcation of the offshore extent of newly formed DSW. The relatively fresh water of the tidally-mixed zone inshore of the shelf front was the precursor of the DSW, aided by the late-autumn offshore transition of the front.

1 Introduction

The Okhotsk Sea is a marginal sea in the subpolar gyre of northwestern Pacific (Fig. 1.1a). It is separated from the open ocean by the chain of Kuril Islands with several fairly deep straits between them. Net inflow of the water through the deepest northern strait, Kruzenshtern (1.9 km deep), and net outflow through the deepest Bussol' strait (2.3 km deep), combined with positive windstress curl sets the general cyclonic circulation in the basin [*Ohshima et al.*, 2004].

A combination of harsh wintertime conditions, wide shelves and relatively high background salinities makes the Okhotsk Sea the principal ventilation site for the intermediate density waters of North Pacific [*Talley*, 1991]. This overturn is driven by brine rejection, accompanying ice formation on the northern shelves of the sea.

Seasonal ice cover extends virtually over the whole basin during the winter; however no multi-year ice is present. Prevailing offshore winds create several fairly large and persistent polynyas along the northern and northwestern coasts (Fig. 1.1b). Rapid frazil ice formation in the polynyas leads to brine rejection and formation of dense shelf water (DSW) in these regions [*Kitani*, 1973; *Alfultis and Martin*, 1987; *Martin et al.*, 1998; *Gladyshev et al.*, 2000]. Subsequently, this cold, oxygen-rich, but relatively fresh water is advected southward along the coast of Sakhalin island and through Bussol' strait into open ocean. Along the way it undergoes significant modification through mixing and entertainment, forming Okhotsk Sea Mode Water (OSMW) [*Yasuda*, 1997; *Gladyshev et al.*, 2003]. Ultimately, OSMW provides the low salinity and high oxygen features of the North Pacific Intermediate Water (NPIW), marking the highest ventilated density levels in the North Pacific [*Talley*, 1991].

Of all the polynyas contributing to OSMW, only the one located on the northwestern shelf produces the densest water (26.8-27.2 σ_θ), with density reaching that of North Pacific Intermediate Water (NPIW) [*Kitani*, 1973; *Gladyshev et al.*, 2000]. The special role of the northwestern polynya (NWP) is likely due to its downstream location with respect to the other northern shelf polynyas, which allows the NWP to augment the brine accumulation started upstream.

Due to the difficulty of wintertime access, all past information regarding the details of DSW formation in the Okhotsk Sea polynyas was derived from satellite remote sensing, warm season in situ observations, and water mass analyses. The present paper summarizes the results of the first direct observation of brine rejection on the northwestern shelf of the Okhotsk Sea, obtained with bottom moorings during the winter of 1999-2000. These observations were described briefly by Shcherbina *et al.* [2003]. Section 2 below presents the hydrographic and mooring data used in the study. An overview of the watermass structure on the shelf in autumn and spring based on the two hydrographic surveys is given in section 3. The ice cover is discussed in section 4. Evolution of bottom water properties and velocity fields in course of the winter is described in sections 5 and 6. Section 7 summarizes the main findings of the study and their implications. An accompanying paper [*Shcherbina et al.*, 2004] combines the direct mooring observations with the meteorological reanalysis and satellite ice-cover data to estimate the DSW formation and export rates.

2 Data

In situ observation of the processes inside the NWP during wintertime convection was made using an array of four bottom moorings deployed on the shelf of Shantarskiy

Bay (Fig. 1.1) in September 1999, two of which were successfully recovered in June 2000. The two surviving moorings were located at (55°45'N, 138°54'E) and (55°39'N, 140°00'E) in 109 and 144 m of water correspondingly, and will be hereafter referred to as the "inshore" (western, shallower) and the "offshore" (eastern, deeper) moorings.

Each mooring was equipped with a Seabird Seacat CTD and an upward-looking 300-kHz broadband RD Instruments Acoustic Doppler Current Profiler (ADCP). Pressure, salinity, temperature and oxygen concentration were recorded with a 15-minute sampling interval. Both CTDs were calibrated before and after the deployment. Observed instrument drift was insignificant (of order of 2×10^{-4} °C yr^{-1} and 1×10^{-2} psu yr^{-1} for temperature and salinity correspondingly). In the final data calibration, the drifts were linearly distributed throughout the deployment period. The ADCPs provided velocity data with 4-m vertical and 16-minute temporal resolution. The first useable bin was located 14.1 m above the bottom. Due to the lack of scatterers in the water column throughout the year and especially in winter, only a 20-50% data return rate was observed in near-surface (maximum range) layers. The range of 95% data return rate was at 50 and 60 m above the bottom at the inshore and offshore moorings, respectively.

To establish the larger-scale context of the experiment, two hydrographic surveys were performed in September 1999 and June 2000. The surveys consisted of 86 and 111 stations correspondingly (Fig. 1.1) covering the northwestern and Sakhalin shelves as well as Bussol' Strait. They included CTD sampling of pressure, temperature and salinity and rosette sampling of salinity, oxygen, and nutrients (silicate, nitrate,

phosphate, nitrite, ammonium). A lowered ADCP was also mounted on the rosette frame.

3 Water properties of the northwestern Okhotsk Sea

The dominating topographic feature of the northwestern Okhotsk Sea is a relatively broad (200-300 km) shelf with typical depth of 100-200 m (Fig. 1.1a). This shelf is characterized by strong tides and accounts for a significant portion of global tidal energy dissipation [*Kowalik and Polyakov*, 1998; *Egbert and Ray*, 2000] (see also section 6.3). The mean cyclonic wind-driven circulation supplies this region with water of North Pacific origin, imported through the northern Kuril straits. Significant watermass modification occurs on the northern shelves due to brine rejection in coastal polynyas in winter, freshwater input from ice melt and river runoff in summer, and tidal and convective mixing. As a result, several distinct transitional watermasses are commonly observed in this region [*Moroshkin*, 1968], as described in the following sections based on our observations.

3.1 Dense Shelf Water (DSW)

Dense shelf water (DSW) is formed on the northern shelves of the basin each winter [*Kitani*, 1973; *Gladyshev et al.*, 2003]. Both surveys showed the presence of DSW as a bottom temperature minimum on the shelf north of Sakhalin, extending into the East Sakhalin current (Fig. 1.2). Even in autumn (Fig. 1.2a,c), the bottom potential temperature was within 0.1°C of freezing. The DSW layer was about 30 m thick and was located along the bottom between 100 and 160m depth with maximum density of 26.93 σ_θ observed at 150 m (Fig. 1.2b).

Property distributions observed in June 2000 (not shown) were qualitatively the same as in September 1999. However, the layer of dense water reached 50 m thickness and extended further inshore. The maximum density was lower (26.81 σ_θ) and was found near the bottom at a shallower (140 m) depth. This difference is the manifestation of interannual variability of the dense water production, which is strongly dependent on winter weather and ice conditions. The winter of 1999-2000 was considerably milder than the previous one, with the mean February 2000 temperature in the northwestern polynya more than 6°C higher than in 1999. Consequently, the dense water production was weaker, and the maximum density observed during the winter of our experiment (26.92 σ_θ, see section 5.1) was lower than during the previous winter.

3.2 Surface & nearshore waters

The offshore stratification during both surveys was capped by a warm and fresh surface mixed layer with densities as low as 21 σ_θ (Fig. 1.2b). In a narrow near-shore band (less than 100 m deep), this layer extended to the bottom likely due to vigorous tidal mixing. Summer sea ice melt likely provides most of the fresh water to this watermass. Even though the freshwater river discharge into the Sea of Okhotsk is quite high (463 km^3 per year), 68% of it comes from the Amur River [*Aota and Ishikawa*, 1991], whose estuary is located farther south (53°N) and likely has little influence on the northwestern shelf. The annual precipitation, which exceeds evaporation by 382 $km^3\ yr^{-1}$ and has a summer maximum [*Aota and Ishikawa*, 1991], may also take part in the near-shore and surface water freshening. For comparison, sea ice melt can be

estimated to yield about 500 km^3 of fresh water over the whole basin upon melting in early summer.

Even though in summer the lateral extent of this near-shore watermass is limited and it is separated from the DSW by a tidal mixing front (Fig. 1.2b), it likely plays a leading role in the dense water formation during the winter. As will be shown in the next section this fresh near-shore water was transformed into DSW by brine rejection during the ice formation season.

3.3 Tidal mixing front

An important feature of the water property distribution on the northern shelves is the 100-kilometer wide front separating the mixed near-shore waters (7.6°C, 31.5 psu in September 1999) from the offshore stratified region (–1.72°C, 33.16 psu at the bottom) (Fig. 1.2). The potential density difference along the bottom was approximately 2 kg m^{-3} implying a baroclinic Rossby deformation radius of order of 10 km. The offshore edge of the front was located approximately at the 110- and 90-meter isobaths in September 1999 and June 2000, respectively. Both in autumn and in spring the front extended from the bottom to the mixed layer (Fig. 1.2; spring is similar). Additionally, a region of anomalously cold and salty mixed layer water was associated with the top of the front (at approximately 139°E) in autumn (Fig. 1.2d-e). This region was also characterized by increased nutrient concentration. (The nitrate distribution is shown in Fig. 1.2f; phosphate and nitrite distributions are similar.) This suggests enhanced exchange between the surface and bottom layers near the front. It is

unclear whether this enhancement is due to upwelling or enhanced mixing, or a combination of the two.

The front is likely created by shoaling of the tidal bottom boundary layer. Similar fronts are commonly observed in tidally active shelf regions [*Simpson and Hunter*, 1974; *Simpson*, 1981]. There are also accounts of increased vertical mixing within such fronts [*Ullman et al.*, 2003]. The boundary layer is clearly seen in the density distribution (Fig. 1.2c) as a region of low stratification along the bottom, thickening towards the shore. At approximately 100-m depth the tidal mixing within the layer overcomes the stabilizing effect of the seasonal thermocline and penetrates to the surface, thus creating the front. Inshore of the front the tidal mixed layer spans the whole water column, eliminating much of the vertical stratification.

In late autumn 1999, the front shifted offshore, as evident from the satellite observations of sea surface temperature (Fig. 1.3). This transition was also registered in properties and velocities in mid-November by the inshore mooring, but not at the offshore mooring (see section 5.1 and Fig. 1.5 below). Apparently, the front stayed between 139°E and 140°E (between the moorings) until it was eliminated by the new dense water formation. As a result, the initial conditions at the beginning of ice formation and brine rejection at the two moorings were significantly different, which may account for differences in the watermass evolution observed at those sites.

Numerical modeling of tidal mixing fronts [*Simpson*, 1981] suggests that the movement of the front could be caused by the erosion of the shelf stratification due to surface cooling in autumn. Decreased stratification in autumn would facilitate vertical

mixing, allowing a thicker boundary layer. As a result, the boundary layer would shoal at a deeper location, leading to the offshore shift of the front.

4 Wintertime evolution: ice cover

Sea ice distribution throughout the winter was observed using the 25-km gridded Special Sensor Microwave Imager (SSM/I) brightness temperature data [*Maslanik and Stroeve*, 1990]. The "thin ice" algorithm [*Cavalieri*, 1994; *Kimura and Wakatsuchi*, 1999] was used to determine the ice extent and distinguish between the new, young and first year ice fractions. The classification is semi-empirical: the "new" ice fraction generally corresponds to frazil, grease, nilas, pancake ice types; "young" ice fraction corresponds to thin (gray) first-year ice; "first year" ice fraction corresponds to thick (white) or snow-covered first year ice [*Cavalieri*, 1994]. There is no multi-year ice present in the basin.

Freezing of the Okhotsk Sea in the winter of 1999-2000 started in late December (Fig. 1.4). Ice cover was first established in the Shelikhov and Shantarskiy bays and along the coast and then progressed into the middle of the basin. Maximum ice extent was reached in the middle of March, and the ice virtually disappeared by June.

The northwestern polynya (NWP), seen as an area of thinner ice over the northwestern shelf (Fig. 1.4), was active from late January to mid-March. Its counterpart, the northern polynya (NP), persisted until early April. Both polynyas closed briefly on 15 February. Even though the NP had a larger lateral and temporal extent, the ice was generally thinner inside the NWP, resulting in greater heat loss than in the NP [*Shcherbina et al.*, 2004].

5 Wintertime evolution: bottom water properties

The time series of bottom water properties recorded by the moorings are shown in Fig. 1.5. The records span 9 months of the annual cycle of DSW evolution, including the active brine rejection in winter, pre-conditioning phase in late autumn, and the summertime period of gradual export of dense water from the shelf region. The following subsections focus on various stages of this cycle, with a summary in section 5.5.

5.1 Brine rejection

Dense shelf water formation is evident in the bottom salinity, potential temperature and potential density time series (Fig. 1.5). A salinity increase associated with brine rejection started at the inshore (western) mooring on 20 January 2000, soon after ice cover at the site was established. A near linear salinity increase continued through 23 February, reaching a maximum salinity of 33.45 psu, for a total of 0.83 psu salinity increase in 35 days. This corresponds to a $\sigma_\theta = 0.68$ kg m^{-3} potential density increase, reaching a maximum potential density of 26.92 kg m^{-3}. A subsequent short-term salinity burst on 15 – 17 March produced an absolute maximum salinity of 33.49 psu (26.95 σ_θ).

DSW formation in 1999-2000 was confined to the area shoreward of the deeper, offshore mooring. No significant salinity increase was observed at the offshore mooring, indicating no active brine rejection penetrating to the bottom. This is a major contrast with the inshore mooring, even though the instruments were less than 70 km

apart. Instead, a slow, steady salinity increase was observed from 16 January to the end of the record in June, probably due to gradual export of dense water from the polynya.

It is worth noticing that the density difference between the two moorings was close to 0.3 kg m^{-3} both before and after the density increase period, although the signs of this difference were opposite. The Rossby deformation radius corresponding to this difference was approximately 5 km. Additionally, the density increase at the inshore mooring stopped briefly when it reached $\sigma_\theta = 26.58$, the density observed at the same time at the offshore mooring. It is presently unclear whether these matches are purely coincidental or are a result of the dynamics of the polynya region.

5.2 Pre-conditioning

The wintertime brine rejection at the inshore mooring was preceded by a sharp 0.5-psu salinity drop and a concurrent 2.5°C temperature increase in mid-November, associated with the transition of the tidal mixing front (see section 3.3) offshore of the mooring site (Fig. 1.5). Even though the temperature returned to near-freezing by mid-January, the salinity recovered only insignificantly. As a result, the density of the water present at the inshore mooring when ice formation started (DSW precursor water) was at least 0.25 kg m^{-3} lower than in early November. Taking into account the preceding density decrease in September and October, this water density is 0.43 kg m^{-3} lower than could be inferred from the September survey alone. This result shifts the attention to the fresh, well-mixed inshore water as the source for DSW formation.

5.3 Potential supercooling

Evidence of surface supercooling was observed during the brine rejection phase at the inshore mooring based on the near-bottom temperature record. The bottom potential temperature stayed $7x10^{-3}$ ºC below the surface freezing point (Fig. 1.6) from 24 January to 4 March, with a short break on 17 February. We term this effect "potential supercooling", as the bottom water with the observed temperature and salinity would be supercooled if shifted adiabatically to the surface. Using this term, we explicitly distinguish this effect from in situ supercooling, which was not observed at our moorings.

We assume that this cold water was brought from the surface by convection, probably driven by brine rejection. Additionally, we assume that the water column was well-mixed by such convection, so the potential temperature at the bottom was equal to the surface temperature or slightly higher due to the mixing of the convective plumes with warmer surrounding water. Consequently, we conclude that the surface water was supercooled by at least $7x10^{-3}$ ºC. No persistent potential supercooling was observed at the offshore mooring.

Surface supercooling of up to 0.1ºC-0.2ºC has been found experimentally to be a characteristic feature if not a necessary condition of frazil ice formation [*Ushio and Wakatsuchi*, 1993]. Episodical supercooling events associated with frazil ice formation have also been observed by *Drucker et al.* [2003] at 30-40 m below the surface. Unlike *Drucker et al.'s* observations, the potential temperatures observed during our experiment were below the surface freezing point, but above the in situ freezing point, so ice formation was not possible at the depth of our measurements. (The bottom

temperatures would be consistent with ice formation to a maximum depth of 10 m, assuming no admixing of warmer waters during convection.) Our observation of potential supercooling serves as an important indicator of active near-surface frazil ice formation at the mooring site. This is further supported by the general coincidence of supercooling events with the periods of thinner ice cover above the mooring (Fig. 1.6b).

It is worth noticing that the potential temperature at the inshore mooring dropped below the surface freezing point simultaneously with the start of the density increase, but then persisted for approximately 10 days after the density increase stopped. This suggests that the brine rejection and DSW formation continued at least through the beginning of March, but its last phase was not accompanied by densification.

5.4 Passage of a warm eddy through the offshore mooring site

An abrupt short-term temperature increase occurred at the eastern (offshore) mooring between 25 February and 6 March (Fig. 1.5). Potential temperature of up to -0.9˚C was observed during that period, which is an absolute maximum over the whole 9-month record at this site. The increase consisted of a series of bursts, between which the temperature recovered to its near-freezing values. The bursts were quasi-periodic with intervals of 12±2 hours between them, suggesting the tidal nature of the observed fluctuations. The temperature fluctuations were well compensated in their effect on density with corresponding salinity changes (Fig. 1.7b). Based on the autumn isopycnal distribution of temperature (not shown), such warm water likely originated from at least 60 km east of the mooring site. The warming was also accompanied by

clockwise rotation of the flow at this offshore mooring, which led to a period of onshore (north-westward) flow (Fig. 1.9). This likely indicates the passage of a warm-core eddy through the site of the mooring. Based on the velocity and temperature observations, the eddy size was of an order of 10 km with characteristic rotation velocity of about 5 cm s^{-1}. The observed tidal pulsation of temperature was likely due to the strong near-bottom stratification within the eddy.

5.5 DSW evolution cycle

Overall, the evolution of bottom water properties in the polynya region followed an annual cycle (Fig. 1.7a), consisting of several distinct phases.

1. During the first (winter) phase (late January to late February) the salinity rapidly increased due to brine rejection. The bottom potential temperature stayed slightly below the surface freezing point, suggesting that the surface water was supercooled (section 5.3).

2. The linear density increase terminated abruptly on 23 February, even though the polynya was still open and the active ice formation and brine rejection continued (as evident from ice observations and potential supercooling). This is further supported by the analysis of heat balance over the mooring sites (Fig. 1.8), which found no significant changes in the surface heat loss at the time of density increase termination. (Details of heat flux calculations are given in the accompanying paper [*Shcherbina et al.*, 2004].) Consequently, during the late stages of DSW formation, the salt influx would have been balanced by enhanced export of excess salt from the polynya region.

Similar abrupt termination of density increase under continuing buoyancy forcing has been modeled numerically [*Gawarkiewicz and Chapman*, 1995]. Their model predicts initial linear increase of density within the polynya region, leading to the formation of a sharp density front at its offshore boundary. Geostrophic adjustment of the front incites counter-rotating rim currents in the bottom and surface layers. Intrinsic instability of this system results in meandering and eventual formation of baroclinic eddies that transport brine-enriched water away from the polynya region while replacing it with fresher water from offshore. Enhanced cross-shelf exchange that results from this process balances salt flux driven by brine rejection in the polynya, leading to a dynamical equilibrium. The velocity record analyzed in the following section provides indirect evidence of such enhanced eddy activity at the inshore mooring between February and May 2000.

3. In spring and summer, salinity at the inshore mooring steadily decreased, suggesting gradual replacement of DSW with fresher water from the northern shelves. Such "flushing" would continue each year until late autumn: the same salinity decrease can be seen through autumn at the beginning of the record. The offshore transition of the tidal mixing front in late autumn brought a significant salinity drop and temperature increase to the inshore mooring. Early winter cooling then brought the temperature to the freezing point, concluding the cycle.

The exact path of the DSW cycle in temperature-salinity space must depend on the particular weather conditions for each given year. Projecting the spring 2000 salinity decrease to the autumn of 2000 would result in lower salinity than was observed in autumn of 1999. The salinity of 33.15 psu observed at the inshore mooring in

September 1999 was actually reached again by June 2000. This is a manifestation of the interannual variability of DSW properties and production rates. The winter of the experiment (1999-2000) was considerably milder than the previous one, with the mean February 2000 temperature in the region of northwestern polynya over 6°C higher than in 1999 (based on ECMWF data). Consequently, the DSW production was likely weaker and DSW properties were less extreme in early 2000 than during the previous winter.

The seasonal cycle of bottom water properties observed at the offshore mooring was radically different, even though the moorings were less than 70 km apart and both were located within the northwestern polynya. The period of thin ice cover (young and new ice types) over the offshore mooring was considerably shorter than over the inshore one. However the cumulative heat loss over these sites was almost identical until mid-February and differed by only 20% by the end of the season (Fig. 1.8). Despite that, both the pre-conditioning and brine rejection phases were missing from the offshore mooring record, and no DSW formation was observed there. The reason for the difference between the two sites is not clear, but may be due to the location of the winter tidal shelf front, and its feedback, through mixing, on the location of the thinnest ice in the NPW.

6 Wintertime evolution: velocity field

The velocity time series at the two moorings (Fig. 1.9) were well correlated with each other. Their mean values were nearly equal: 6.35 cm s^{-1} at the inshore mooring and 6.40 cm s^{-1} at the offshore one. The mean flow was directed southwest approximately along isobaths. (A detailed investigation of the relation of the flow to

the local topography is impossible due to lack of sufficient information about the latter.) This flow direction is consistent with the general cyclonic circulation in the Okhotsk Sea [*Ohshima et al.*, 2004]. The flow exhibited significant seasonal variations (section 6.1) and was generally much weaker than the barotropic tides. The tidal amplitudes were an order of magnitude larger than the long-period variability, so the tidal and subtidal flow variability will be discussed separately in section 6.3.

6.1 Subtidal horizontal flow variability

Low-frequency (subtidal) horizontal velocities measured at both moorings were fairly barotropic throughout the deployment period (Fig. 1.10). The records show a general increase of southward flow between October and January, with weaker flow during the ice-covered period that followed (Fig. 1.9b). Such variation is consistent with the seasonal changes of the basin circulation in response to the large-scale wind forcing variations [*Ohshima et al.*, 2004]. The strongest flow (over 50 cm s^{-1} on both stations) was registered during the storm of 12 December 1999 when the wind reached its maximum over the observation period (19 m s^{-1} based on ECMWF meteorological reanalysis).

6.2 Vertical velocity variability

Negative mean vertical velocity was measured at both moorings: -3.8 mm s^{-1} (inshore) and -1.7 mm s^{-1} (offshore). These values are too large and too depth-independent to be explained by the effects of the bottom slope (even though the exact local slopes are unknown due to poorly resolved topography) and are likely a measurement artifact. Similar negative bias in the vertical velocity ADCP record has

been previously reported by *Schott et al.* [1993]. The bias is assumed to be time-independent, so the seasonal variation of vertical flow with respect to the mean can still be investigated.

An intriguing feature of the vertical velocity recorded at the inshore mooring is the enhancement of downward flow in the upper 70 m of the water column between mid-January and late-April, followed by an upward flow anomaly near the bottom in May and June (Fig. 1.10c). The period of anomalous downward flow coincides remarkably well with the presence of ice cover over the mooring, as determined by the intensity of ADCP surface echoes (Fig. 1.5). The standard deviation of vertical velocity was also higher during this period (Fig. 1.11), and the distribution was noticeably skewed towards downward flow. Such vertical velocity behavior is similar to that observed during deep convection events in the Greenland Sea [*Schott et al.*, 1993] and might indicate the presence of convective cells under the ice. Numerical models predict anisotropy of the brine-driven convective cells leading to the downward velocities being several times larger than the upward ones [*Kampf and Backhaus*, 1998]. Such asymmetry would explain both the skewness and the negative mean of the velocity distribution. However the model also predicts that the scale of downward plumes would be considerably smaller than both the distance between them and the surface spreading of ADCP beams. Consequently, the plume observation is expected to be much more intermittent than the observed persistent anomalous downward flow. On the other hand, the downward flow anomaly at the offshore mooring during the ice-covered period was much weaker (Fig. 1.10f). As evident from the bottom water evolution (section 5.1), active brine rejection was observed only at the inshore

mooring. Consequently it is tempting to suggest that the observation of downward flow is associated with brine rejection and DSW formation. A direct connection, however, cannot be established with this dataset.

An upward flow anomaly was observed in May at the inshore mooring and, to a much smaller extent, at the offshore location (Fig. 1.10). The exact nature of this shift is also unknown. Vertical diurnal migration of zooplankton can provide a partial explanation for the skewness of the vertical velocity distribution towards positive values (most prominent in the near-bottom layers, Fig. 1.11). Such migration, resulting in apparent daily spikes of upward flow, is a known artifact in ADCP velocity measurements [*Schott and Johns*, 1987; *Wilson and Firing*, 1992]. Vigorous migration that is also seen in the ADCP echo strength signal (not shown) resumed right after the disappearance of ice cover in early May and caused the observed vertical velocity distribution skewness. The plankton migration hypothesis, however, explains neither the shift of the whole vertical velocity distribution towards positive values in May (Fig. 1.11), nor the virtual absence of such a shift at the other mooring. It also does not negate the observations of the anomalous downward flow during the ice-covered period. Even though the spring upward flow anomaly may have shifted the long-term vertical velocity average, thus increasing the apparent magnitude of the wintertime downward flow anomaly, the latter can be also traced with respect to the late-autumn flow (Fig. 1.10, Fig. 1.11).

6.3 Barotropic and baroclinic tides

The tidal signal at both moorings was much stronger than the mean flow, with amplitudes reaching 50 cm s^{-1}. The major tidal component was M2 with amplitudes of approximately 29 cm s^{-1} at the inshore mooring and 21 cm s^{-1} at the offshore one. The second largest component was S2, with amplitudes of 10 and 7 cm s^{-1}, correspondingly. All components exhibited strong elliptical polarization (ratio of the major to minor axis of about 6), with major axes nearly perpendicular to the isobaths (Fig. 1.12).

Tidal flow was predominantly barotropic with a typical mean vertical shear of about $3x10^{-3}$ s^{-1}. However, several bursts of high shear occurred at the inshore mooring in the second half of the record. The peaks in the root mean square vertical shear (Fig. 1.13) coincided remarkably well with prominent disturbances in the density trend. The most energetic event (19-27 February) was associated with the termination of the linear density increase associated with brine rejection in the polynya. (The shear intensification and density drop in mid-November were due to the transition of a tidal mixing front through the mooring site and should be analyzed separately from the winter events.) Several weaker events also occurred later, at quasi-regular intervals of 23-25 days. High shear events exhibited little correlation with the tidal cycle: while the first (24 February) and the last (6 May) of them roughly coincided with spring barotropic tides, the other two occurred closer to the neaps.

Investigation of the temporal frequency structure of vertical shear record (Fig. 1.14) shows that the shear variance peaks were caused by intensification of the semidiurnal internal tide component. Shear intensification was most prominent in the

30-40 m thick near-bottom layer (Fig. 1.15). Vertical propagation of the vertical shear maximum can be clearly seen during the two strongest events (shown in detail in Fig. 1.15), although the direction of such propagation was different. Such internal tide amplification is likely due to the instigation of vertical stratification associated with the baroclinic instability of the polynya rim current. Series of baroclinic eddies that appear at the later stages of adjustment of density anomaly under a polynya [*Gawarkiewicz and Chapman*, 1995] can create sharp stratified layers which may allow internal tide generation. Vertical propagation and temporal intermittency of patches of high shear likely reflect the corresponding changes of the high-stratification regions.

No wintertime internal tide intensification events were observed at the offshore mooring (Fig. 1.13b). On the contrary, typical shears at that site during January to March were half as large as during the rest of the record. Only slight shear intensification was associated with the warm eddy passing the mooring in the end of February (see section 5.4). This relatively "quiet" shear field at the offshore mooring yet again supports the conclusion that the two moorings were situated in radically different dynamical regimes, and that only the inshore mooring recorded actual DSW formation.

7 Summary

Dense shelf water formation on the northwestern shelf of the Okhotsk Sea was observed directly for the first time using wintertime bottom moorings. The relatively warm, fresh, well-homogenized water inshore of the shifting tidal mixing front was shown to be the precursor of DSW. This result calls for the reconsideration of DSW

formation rate estimates, which have been based on inadequate assumptions resulting from the lack of in-situ wintertime data [*Martin et al.*, 1998]. Formation rate estimates using our moored data and findings regarding the precursor DSW are given in the accompanying paper [*Shcherbina et al.*, 2004]. The nearly linear potential density increase associated with brine rejection continued for over a month in January - February 2000, reaching 26.92 kg m^{-3} (0.68 kg m^{-3} density increase).

The density increase terminated abruptly on 23 February 2000, while the ice formation continued for several more weeks based on the observed potential supercooling and heat flux analysis. The assumed continuing salt flux was likely balanced by the enhanced offshore exchange driven by baroclinic instability at the edge of the forcing region. In the present study indirect evidence for the presence of baroclinic eddies transporting the density anomaly offshore was provided by periodic intensification of near-bottom internal tides. It is suggested that such intensification indicates periods of high stratification within the eddies. This is further supported by numerical simulations of the process of internal tide generation accompanying the dense water formation [Shcherbina, in preparation].

In contrast with observations at the inshore (western) mooring, neither the density increase nor the baroclinic tide intensification was found at the offshore (eastern) mooring. These suggest that no DSW formation occurred at the offshore mooring site that winter, or at least that the DSW formed never penetrated to the bottom. Instead, the bottom water density increased slowly, likely due to gradual mixing with the dense water inside the polynya and advection from upsstream. This is surprising, since both moorings were located within the active heat loss area of the northwestern polynya,

and the density at the shallower inshore mooring was higher that at the offshore one. The mechanisms that set the offshore boundary of newly formed DSW between the two moorings need to be further investigated. In particular, the role of the final position of the tidal mixing front may prove to be important, as the structure of vertical mixing and amount of pre-conditioning are radically different on either side of it.

The findings of this study emphasize the need for including local shelf dynamics in addition to the external buoyancy forcing when estimating the dense shelf water formation rates. The first step towards this goal, utilizing the information of the observed variability of the advection field, is described in the accompanying paper [*Shcherbina et al.*, 2004].

Acknowledgements. This work was supported through the National Science Foundation grant OCE-9811958 and by Hokkaido University (ship support). Technical support was provided by the Oceanographic Data Facility and the Instrument Development Group at Scripps Institution of Oceanography (SIO), and by the captain and crew of the R/V Professor Khromov.

References:

Alfultis, M. A. and S. Martin, Satellite passive microwave studies of the Sea of Okhotsk ice cover and its relation to oceanic processes, *J. Geophys. Res.*, 92, 13013-13028, 1987.

Aota, M. and M. Ishikawa, Fresh water supply to the Sea of Okhotsk and volume transport of Soya Warm Current, *Bull. Hokkaido Natl. Fish. Res. Inst.*, 55, 109-113, 1991.

Cavalieri, D., A microwave technique for mapping thin sea ice, *J. Geophys. Res.*, 99, 12561-12572, 1994.

Drucker, R., S. Martin, and R. Moritz, Observations of ice thickness and frazil ice in the St. Lawrence Island polynya from satellite imagery, upward looking sonar, and salinity/temperature moorings, *J. Geophys. Res.*, 108(C5), 3149, 2003.

Egbert, G. D. and R. D. Ray, Significant dissipation of tidal energy in the deep ocean inferred from satellite altimeter data, *Nature*, 405(6788), 775-778, 2000.

Gawarkiewicz, G. and D. Chapman, A numerical study of dense water formation and transport on a shallow, sloping continental shelf, *J. Geophys. Res.*, 100, 4489-4507, 1995.

Gladyshev, S., S. Martin, S. Riser, and A. Figurkin, Dense water production on the northern Okhotsk shelves: comparison of ship-based spring-summer observations for 1996 and 1997 with satellite observations, *J. Geophys. Res.*, 105, 26281-26299, 2000.

Gladyshev, S., L. Talley, G. Kantakov, G. Khen, and M. Wakatsuchi, Distribution, formation, and seasonal variability of Okhotsk Sea Mode Water, *J. Geophys. Res.*, 108(C6), 3186, doi:10.1029/2001JC000877, 2003.

Kampf, J. and J. O. Backhaus, Shallow, brine-driven free convection in polar oceans - nonhydrostatic numerical process studies, *J. Geophys. Res.*, 103(C3), 5577-5593, 1998.

Kimura, N. and M. Wakatsuchi, Processes controlling the advance and retreat of sea ice in the Sea of Okhotsk, *J. Geophys. Res.*, 104(C5), 11137-11150, 1999.

Kitani, K., An oceanographic study of the Okhotsk Sea - particularly in regard to cold waters, *Bull. Far Seas Fish. Res. Lab.*, 9, 45-76, 1973.

Kowalik, Z. and I. Polyakov, Tides in the Sea of Okhotsk, *J. Phys. Oceanogr.,* 28(7), 1389-1409, 1998.

Martin, S., R. Drucker, and K. Yamashita, The production of ice and dense shelf water in the Okhotsk Sea polynyas, *J. Geophys. Res.*, 103, 27771-27782, 1998.

Maslanik, J. and J. Stroeve, DMSP SSM/I daily polar gridded brightness temperatures (CD-ROM). Boulder, CO: National Snow and Ice Data Center, 1990, updated 2003.

Moroshkin, K. V., *Water masses of the Sea of Okhotsk*, U.S. Dept. of Commerce Joint Publication Research Service, Washington, DC, 1968.

Ohshima, K., D. Simizu, M. Itoh, G. Mizuta, Y. Fukamachi, S. Riser, and M. Wakatsuchi, Sverdrup balance and the cyclonic gyre in the Sea of Okhotsk, *J. Phys. Oceanogr.*, 2004.

Schott, F., M. Visbeck, and J. Fischer, Observations of vertical currents and convection in the Central Greenland Sea during the winter of 1988-1989, *J. Geophys. Res.*, 98(C8), 14401-14421, 1993.

Schott, F. and W. Johns, Half-year-long measurements with a buoy-mounted acoustic Doppler current profiler in the Somali Current, *J. Geophys. Res.*, 92(C5), 5169-5176, 1987.

Shcherbina, A. Y., L. D. Talley, and D. L. Rudnick, Direct observations of North Pacific ventilation: brine rejection in the Okhotsk Sea, *Science*, 302(5652), 1952-1955, 2003.

Shcherbina, A. Y., L. D. Talley, and D. L. Rudnick, Dense water formation on the northwestern shelf of the Okhotsk Sea. Part II: quantifying the transports, *J. Geophys. Res.*, 2004.

Simpson, J. H., The shelf-sea fronts: implications of their existence and behaviour, *Phil. Trans. Roy. Soc. London*, A302(1472), 531-543, 1981.

Simpson, J. H. and J. R. Hunter, Fronts in the Irish Sea, *Nature*, 250, 404-406, 1974.

Talley, L. D., An Okhotsk water anomaly: implications for ventilation in the North Pacific, *Deep Sea Res.*, 38(Suppl. 1), S171-S190, 1991.

Ullman, D. S., A. C. Dale, D. Hebert, and J. A. Barth, The front on the northern flank of Georges Bank in spring: 2. Cross-frontal fluxes and mixing, *J. Geophys. Res.*, 108(C11), 8010, doi: 10.1029/2002JC001328, 2003.

Ushio, S. and M. Wakatsuchi, A laboratory study on supercooling and frazil ice production processes in winter coastal polynyas, *J. Geophys. Res.*, 98, 20321-20328, 1993.

Wilson, C. D. and E. Firing, Sunrise swimmers bias acoustic Doppler current profiles, *Deep Sea Res.*, 39(5), 885-892, 1992.

Yasuda, I., The origin of the North Pacific Intermediate Water, *J. Geophys. Res.*, 102, 893-909, 1997.

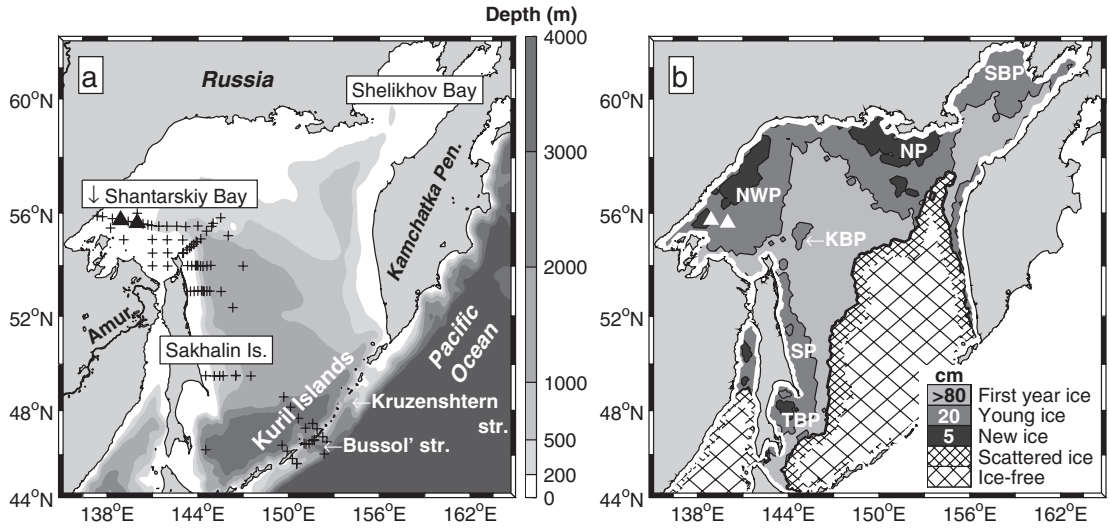

Fig. 1.1 The Okhotsk Sea. (a) The topographic map shows station positions of the September 1999 hydrographic survey (dots) and bottom mooring locations (triangles). Most of the stations were repeated during the June 2000 survey. (b) Ice distribution on 1 February 2000 shows the persistent polynyas: Shelikhov Bay (SBP), northern (NP), northwestern (NWP), Kashevarov Bank (KBP), Sakhalin (SP) and Terpeniya Bay (TBP). Ice classification based on National Snow and Ice Data Center SSM/I brightness temperatures. White triangles show the bottom mooring positions.

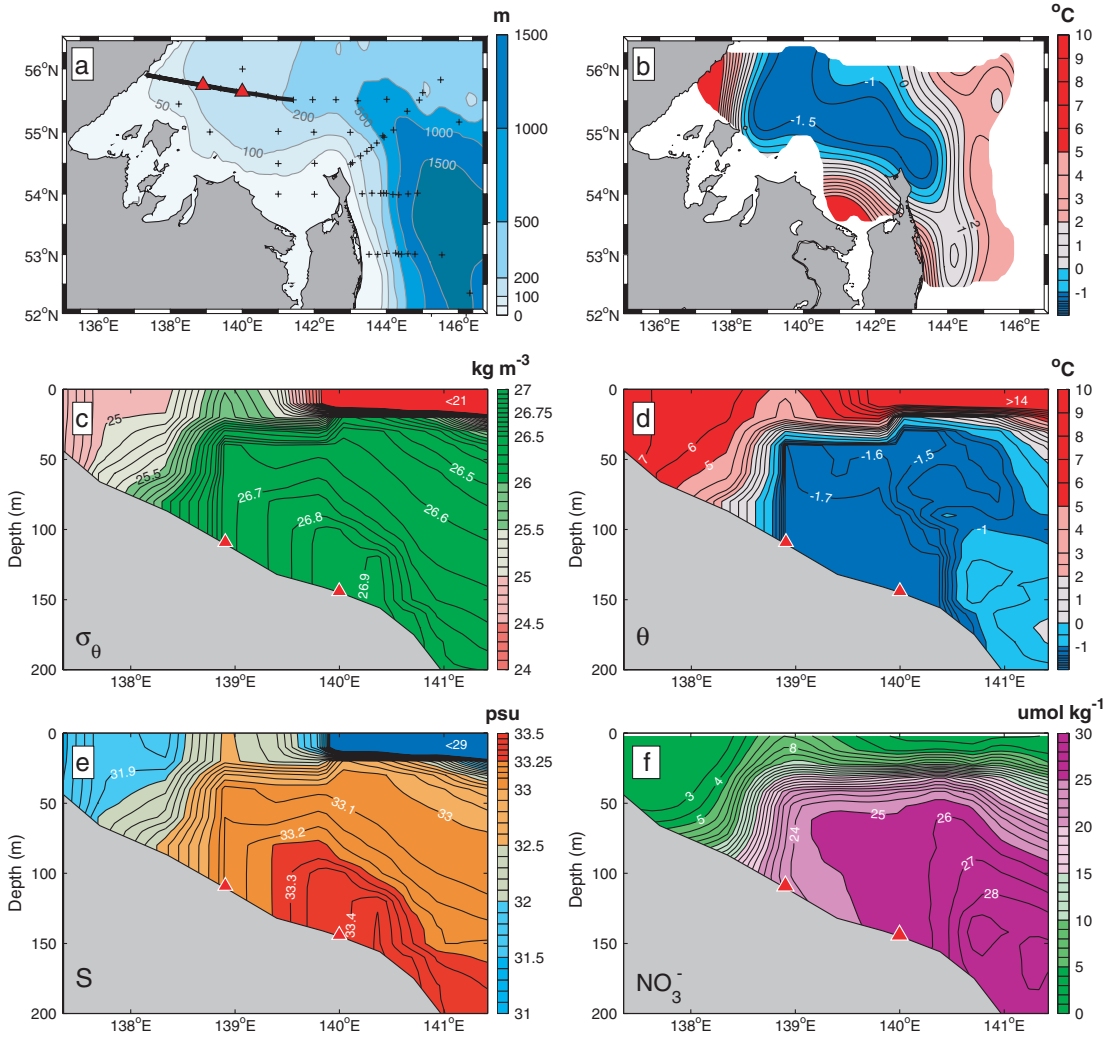

Fig. 1.2 Hydrography of the northwestern shelf in September 1999. (a) Topographic map showing station positions (crosses), bottom mooring locations (triangles), and cross-shelf section location (thick line). (b) Distribution of bottom potential temperature. Vertical cross-shelf sections of (c) potential density, (d) potential temperature, (e) salinity, and (f) nitrate concentration. Section location is marked by thick line in (a).

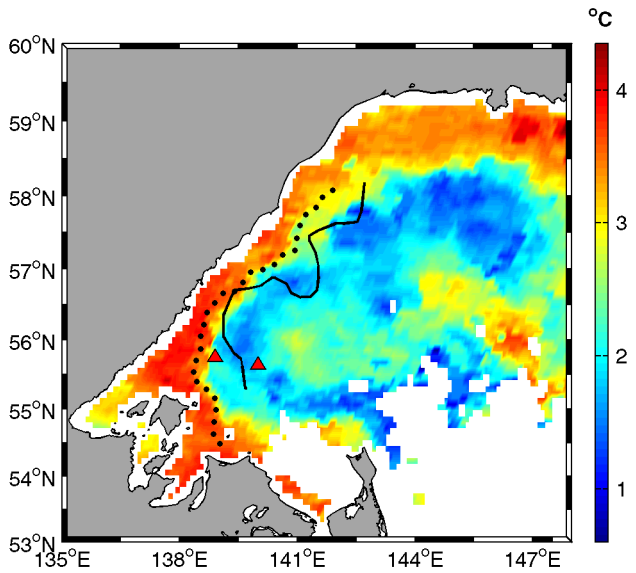

Fig. 1.3 Sea Surface Temperature on 3 November 1999. Front locations derived from the similar images taken on 19 October (dots) and 17 November (black line) are shown. Red triangles mark the mooring positions. Ocean Pathfinder AVHRR data were obtained from the NASA Physical Oceanography Distributed Active Archive Center at the Jet Propulsion Laboratory, California Institute of Technology.

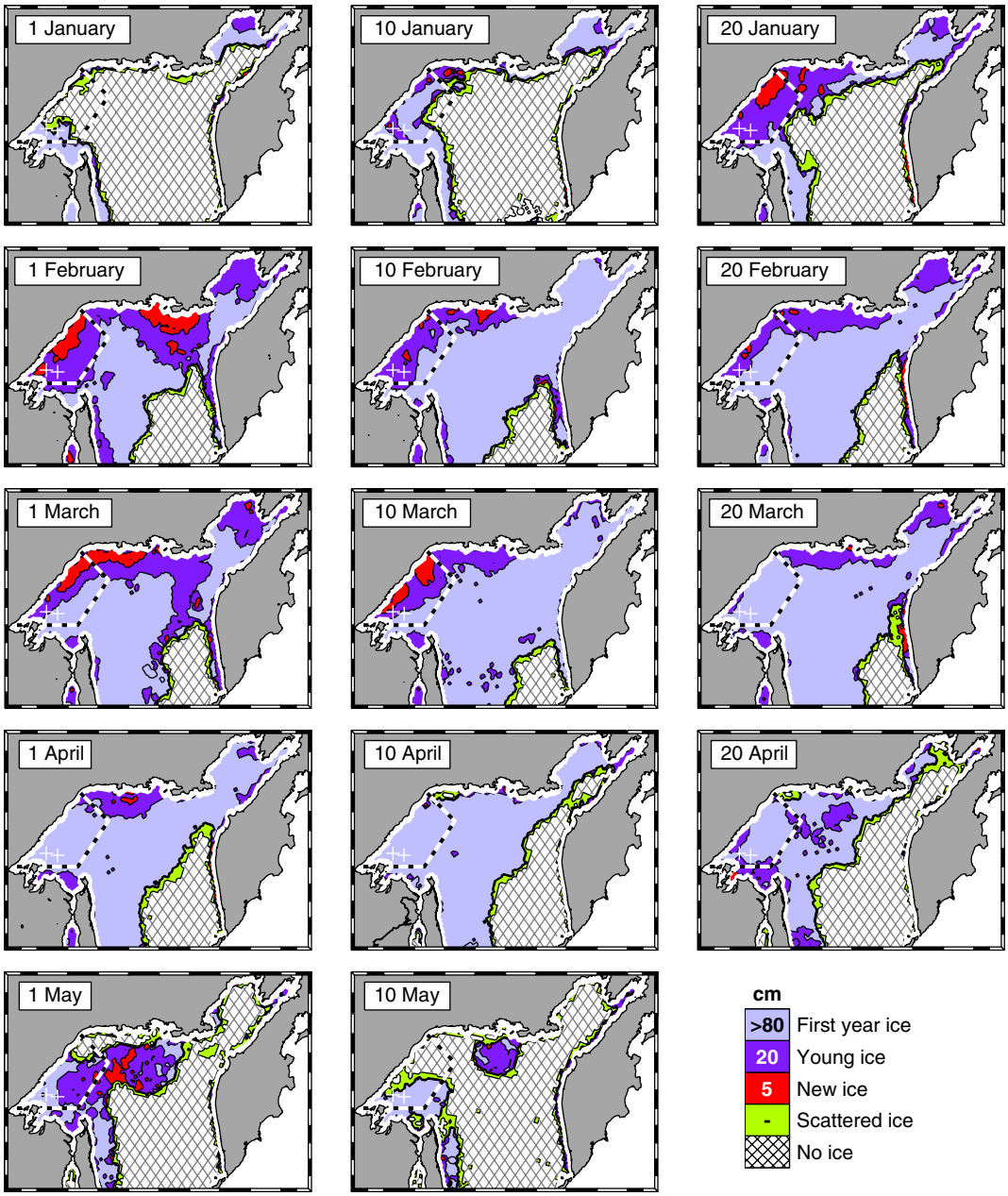

Fig. 1.4 Evolution of ice cover in the northern Okhotsk Sea in early 2000. Ice classification based on National Snow and Ice Data Center SSM/I brightness temperatures. Typical ice thickness (in cm) of the ice types is marked on the legend. Northwestern polynya region boundary is marked by dashed line. White crosses mark the mooring locations.

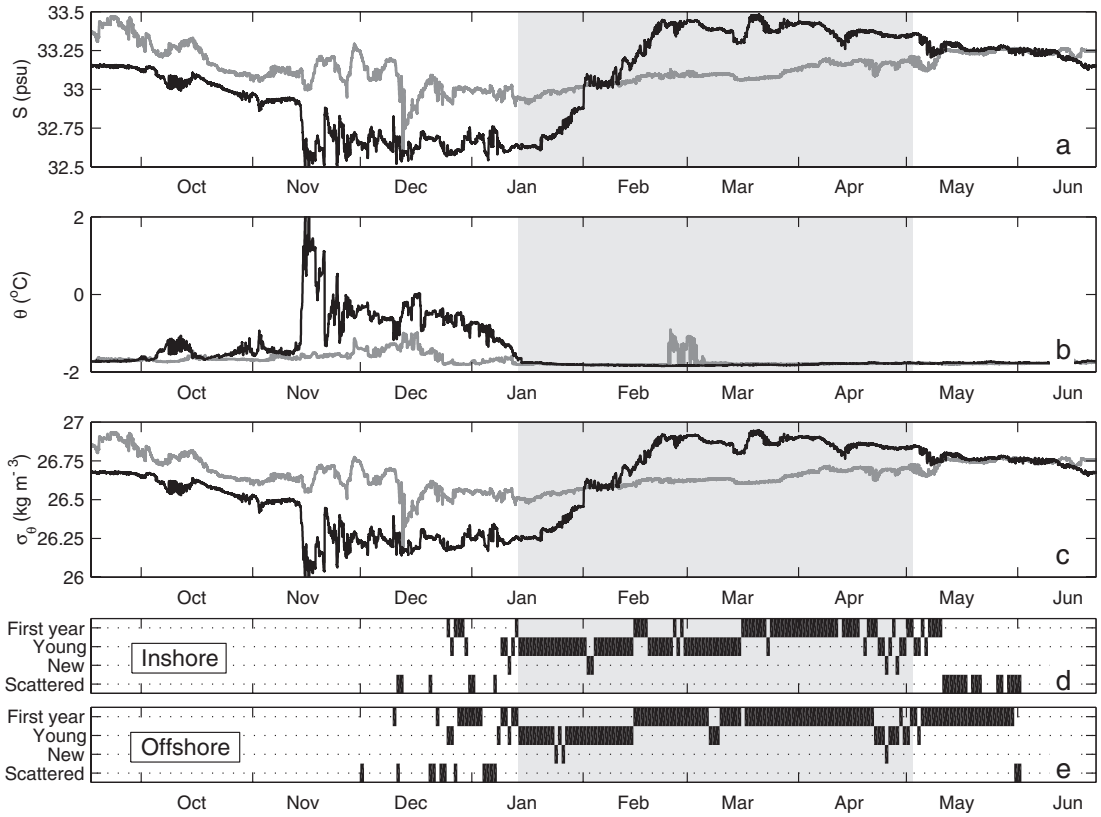

Fig. 1.5 Bottom water properties at the moorings. (a) Salinity, (b) potential temperature, (c) potential density on the inshore (black line) and offshore (gray line) bottom moorings. Gray shading represents the ice-covered period at the inshore mooring (based on ADCP surface reflection intensity). Ice classification at the (d) inshore and (e) offshore moorings based on SSM/I brightness temperatures is also shown. Black shading indicates presence of a given ice type. Ice types are the same as in the previous figure

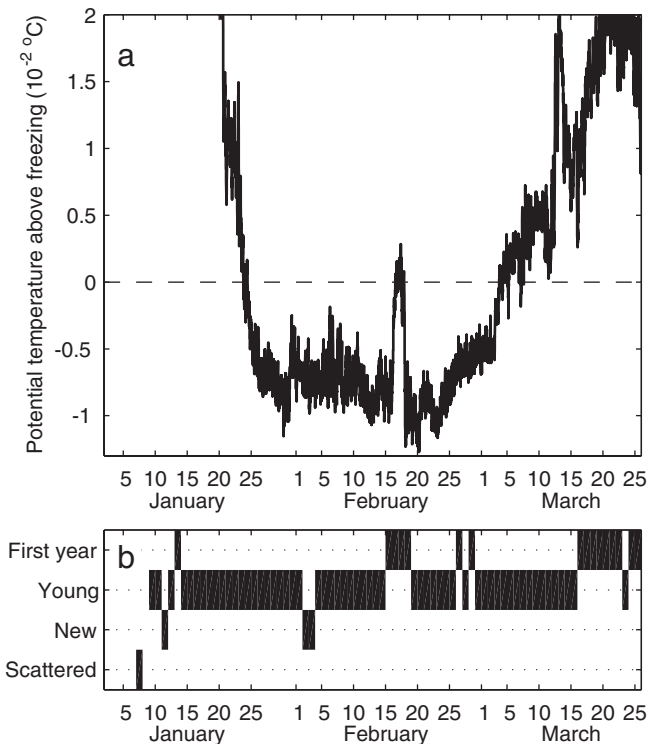

Fig. 1.6 "Potential supercooling" at the inshore mooring. (a) Difference between the bottom potential temperature and the freezing point at the bottom salinity and atmospheric pressure is plotted. (b) Ice classification based on SSM/I brightness temperature. Black shading indicate presence of a given ice type. Ice types are the same as in Fig. 1.4.

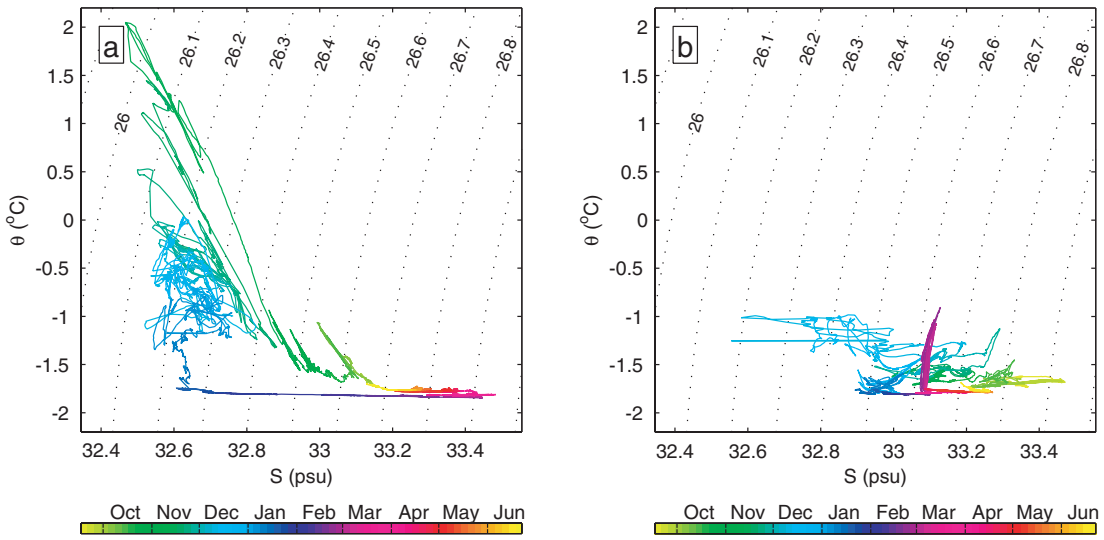

Fig. 1.7 Scatter plots of bottom water properties at (a) inshore mooring and (b) offshore moorings, color-coded with time. Dashed lines are isopycnal (σ_θ=const) contours (labeled in kg m^{-3}).

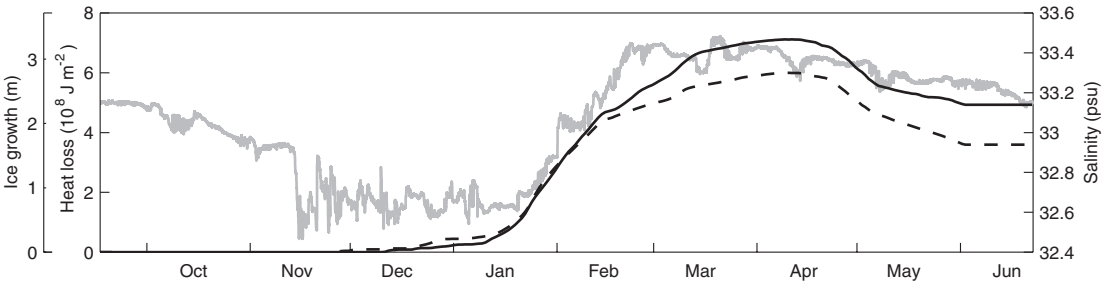

Fig. 1.8 Cumulative heat loss through the ice above the inshore (solid black line) and offshore (dashed black line) mooring site. The leftmost scale shows the ice growth equivalent to this heat loss. Salinity at the inshore mooring (gray line) is shown for reference. The estimates of heat fluxes and ice classification are based upon European Centre for Medium-Range Weather Forecasts (ECMWF) reanalysis meteorology and National Snow and Ice Data Center ice data, respectively.

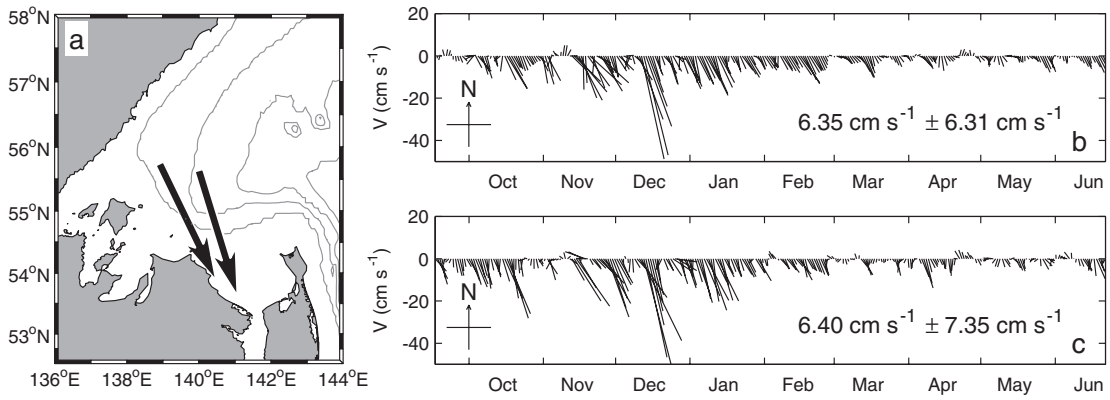

Fig. 1.9 (a) Mean flow and the velocity vector time series at (b) inshore and (c) offshore mooring (vertical mean, 48-hour Blackman filter low-pass). Both direction and amplitude are shown (north is up). Absolute mean and standard deviation is shown for each time series.

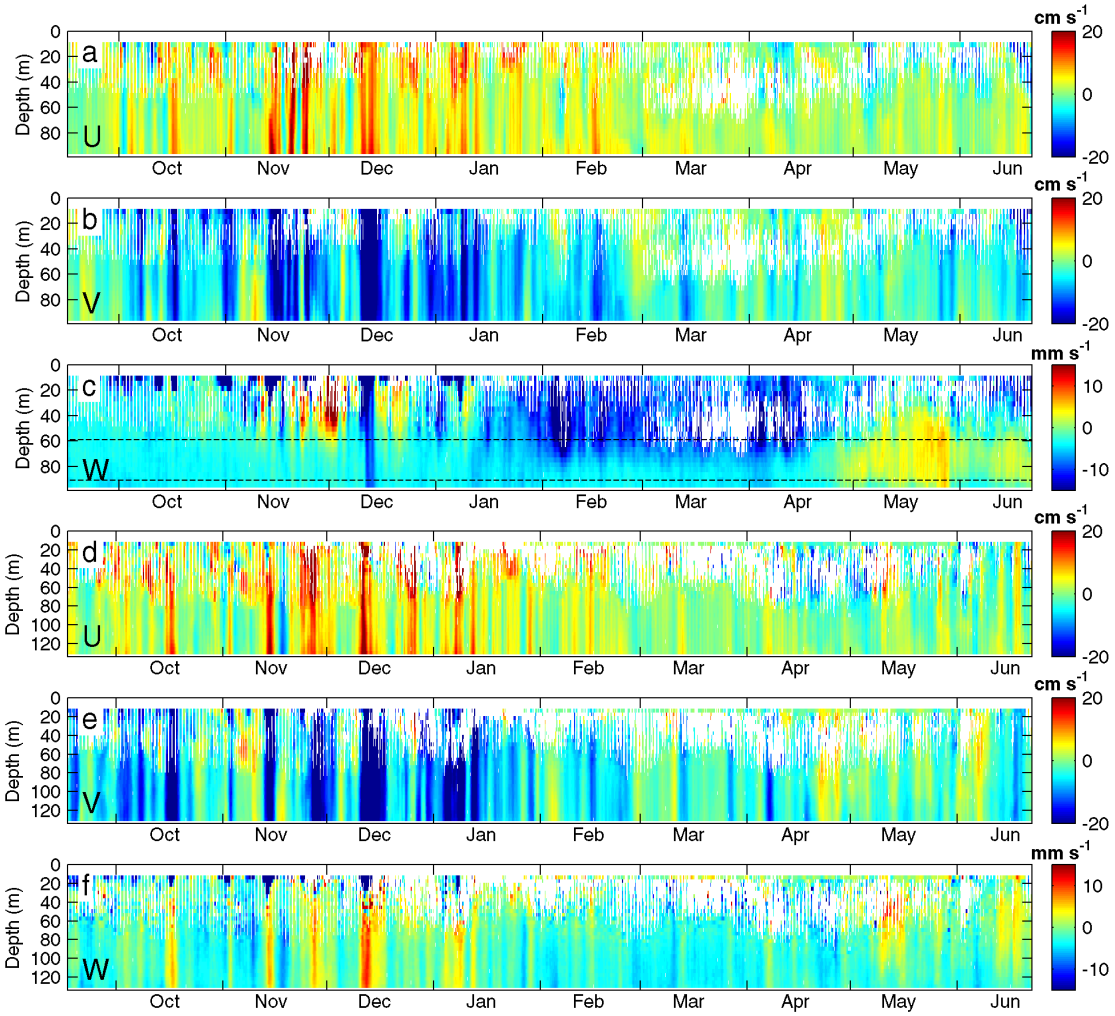

Fig. 1.10 ADCP velocity record at inshore (a-c) and offshore (d-f) moorings. Eastward (a,d), northward (b,e), and upward (c,f) velocities are shown. White areas indicate missing data. Data were low-passed with 48-hour Blackman filter. Bi-monthly histograms of vertical velocity distribution at the horizons marked by dashed line in (c) are shown in Fig. 1.11. Note different scales for horizontal and vertical velocity plots.

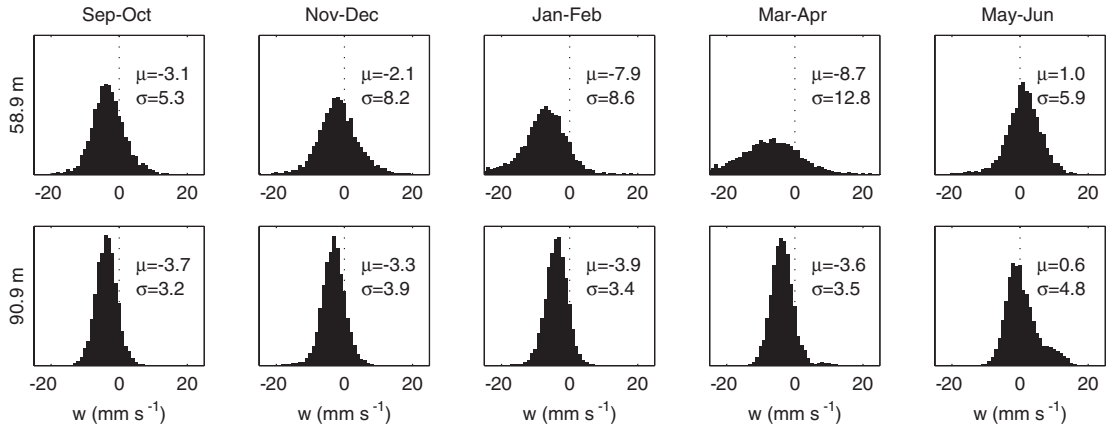

Fig. 1.11 Bi-monthly histograms of unfiltered vertical velocity at the inshore mooring at 59 m (top row) and 91 m (bottom row) depth levels (shown by dashed lines in Fig. 1.10c). Columns represent two-month periods as marked at the top. Mean (μ) and standard deviation (σ) values are given for each distribution (in mm s^{-1}).

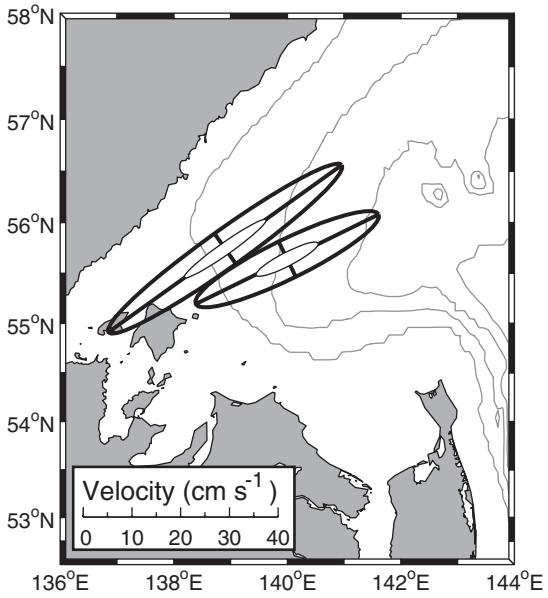

Fig. 1.12 Mean current ellipses for the M_2 (outer ellipse) and S_2 (inner white ellipse) tide.

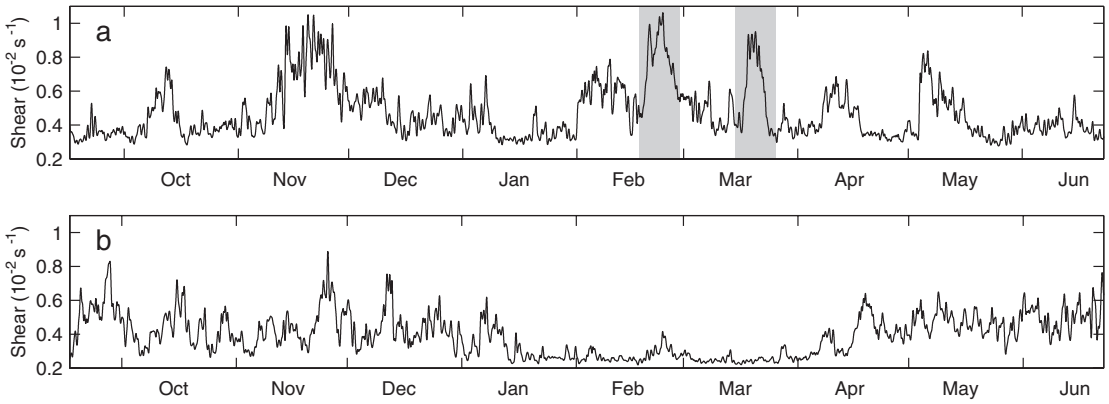

Fig. 1.13 Root mean square vertical shear at (a) inshore and (b) offshore moorings. Averaged within 50 m off the bottom and low-passed with 24-hour Blackman filter. Details of shaded events are shown in Fig. 1.15. 95% confidence limits are within 10% of the plotted values.

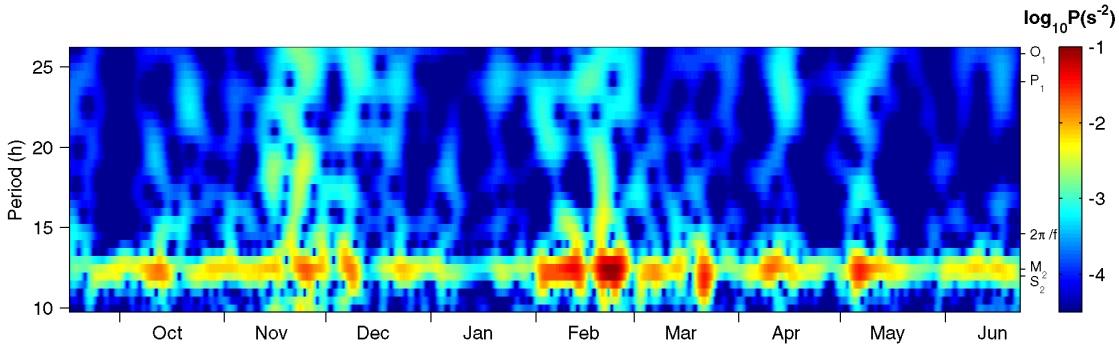

Fig. 1.14 Distribution of vertical shear variance as a function of time and period (clockwise-rotating). Data from 40 m off the bottom at the inshore mooring are shown. Periods of major tidal constituents as well as the inertial period ($2\pi/f$) are marked on the right. Rotary wavelet transform with Morlet wavelet of order c=20 was used.

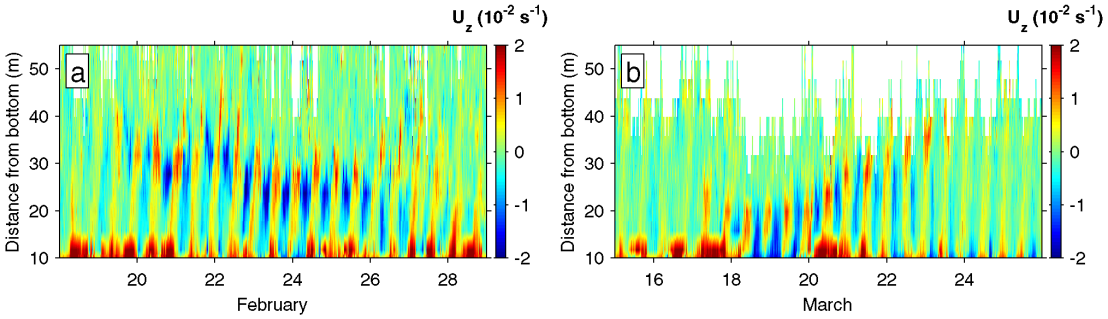

Fig. 1.15 Vertical shear at the inshore mooring during the internal tide intensification events: (a) 18-29 February 2000, and (b) 15-26 March 2000 (periods of these events are shaded in Fig. 1.13). Zonal component of the shear is shown (meridional is similar but offset by ¼ of the period).

CHAPTER II

Quantifying the Transports

The text of this chapter, in full, is a reprint of the material as it appears in Shcherbina, A. Y., L. D. Talley, and D. L. Rudnick. Dense water formation on the northwestern shelf of the Okhotsk Sea: 2. Quantifying the transports, *J. Geophys. Res.*, 109, C09S09, doi:10.1029/2003JC002197, 2004. The dissertation author was the primary researcher and author, and the co-authors listed in this publication directed and supervised the research which forms the basis for this chapter.

Abstract. A combination of direct bottom mooring measurements, hydrographic and satellite observations, and meteorological reanalysis was used to estimate the rate of formation of Dense Shelf Water (DSW) due to brine rejection on the Okhotsk Sea northwestern shelf and the rate of export of DSW from this region. Based on remote sensing data, an estimated 8.6×10^{12} m^3 of DSW was formed during the winter of 1999-2000, resulting in a mean annual production rate of 0.3 Sv. According to direct observations, the export rate of DSW during this period varied from negligibly small in autumn, to 0.75±0.27 Sv in winter (January-February), to 0.34±0.12 Sv in spring (March-April). From these observations the mean annual export rate can be estimated to be 0.27 Sv. The same relationships used to obtain the integral estimates were also applied differentially using an advective approach incorporating realistic flow and heat flux fields, which allowed direct comparison with the moored observations. The comparison highlights the importance of along-shelf advection and cross-shelf eddy transport to the accurate parameterization of DSW formation.

1 Introduction

The Okhotsk Sea is known to be the origin of the densest watermass formed in the North Pacific, its intermediate water (NPIW) [*Talley*, 1991; *Talley*, 1993; *Yasuda*, 1997]. The initial overturn is driven by brine rejection during ice formation in the northern coastal polynyas, leading to formation of dense shelf water (DSW) with densities of up to 27.2 σ_θ [*Kitani*, 1973; *Gladyshev et al.*, 2000].

A chain of persistent polynyas (Fig. 2.1) occurs along the northern and northwestern shelves of the Okhotsk Sea each winter due to the offshore winds. Intense heat loss inside the polynyas leads to intense ice formation and brine rejection into underlying waters. Newly formed DSW is advected by the large-scale wind-driven cyclonic circulation in the basin while each polynya in turn contributes to the density increase. The northwestern polynya (NWP) finishes this process, after which the DSW is transported southward by the East Sakhalin Current.

Annual formation of DSW gives rise to a layer of Okhotsk Sea mode water (OSMW) in the 26.7-27.0 σ_θ potential density range, characterized by low potential vorticity and high oxygen content [*Yasuda*, 1997]. *Gladyshev et al.* [2000] estimated the DSW contribution to OSMW to be 25 to 45% in the 26.65-26.85 σ_θ range. OSMW is subsequently modified in the Kuril basin, where the Soya Warm Current water affects the upper OSMW, and vertical mixing extends its signature downward to 27.1-27.6 σ_θ [*Kitani*, 1973; *Talley*, 1991; *Gladyshev et al.*, 2003]. OSMW is eventually exported into the open ocean through Bussol strait leading to the ventilation of NPIW in both the subpolar and subtropical gyres.

Estimation of the dense shelf water formation rates is consequently important for parameterization of the whole downward branch of the North Pacific thermohaline circulation. *Yasuda* [1997] estimated a rate of outflow of OSMW through the Bussol' strait of 1.1±0.8 Sv (1 Sv = 10^6 m^3 s^{-1}), which would require a net production of 0.4±0.3 Sv of DSW per year. Using a simple box model involving CFC data, Wong *et al.*[1998] estimated a much larger DSW formation rate of 0.9-9.4 Sv. *Martin et al.* [1998] and *Gladyshev et al.*[2000], using remotely-sensed ice production rates and non-winter hydrographic surveys respectively, estimated annual DSW formation rates between 0.2 and 0.5 Sv depending on the winter conditions for a given year. Seasonal change in the DSW outflow from 1.4±1.2 Sv during February-May to 0.2±0.1 Sv in summer, with an annual average of 0.6±0.6 Sv, has also been suggested by historical hydrographic data analysis for the Kuril Basin [*Gladyshev et al.*, 2003]. Another analysis of historical data [*Itoh et al.*, 2003] further supports these results, yielding a mean annual DSW formation rate of 0.67 Sv.

The present study estimates the rates of DSW formation and export during the winter of 1999-2000 using both satellite and in-situ wintertime observations (section 2). The relationship of surface heat loss to densification of shelf waters is also investigated using the advective approach with the flow and heat flux fields based on observations (section 3). The datasets are described in *Shcherbina et al.* [2003; 2004].

2 Estimating DSW formation and export rates

Using a combination of remote and in-situ observations, we attempt to construct a comprehensive image of the evolution of DSW on the northwestern shelf, relating the

independent estimates of formation and export rates of this watermass. First, we use the surface heat loss based on the ice distribution and meteorology fields to estimate the salt enrichment due to ice formation, allowing the approximation of DSW formation rate (section 2.1). Second, the export rates are estimated using moored velocity data and assumptions of the DSW cross-section area based on hydrographic data (section 2.2). Both estimates are combined in section 2.3 in a simple production-export model.

2.1 Formation rates of DSW based on satellite and reanalysis data

Indirect methods of estimation of brine rejection and mixing rates based on remote sensing and/or watermass analysis are the only means of studying dense water formation in most polynyas worldwide. Our moorings provide a rare opportunity to compare and combine the direct and indirect methods.

The first estimates of dense water formation on the northwestern shelf of the Okhotsk Sea based on Special Sensor Microwave/Imager (SSM/I) ice concentration and NCEP reanalysis meteorological data were made by *Alfultis and Martin* [1987] and *Martin et al.* [1998]. *Ohshima et al.* [2003] suggested an improved heat flux calculation algorithm incorporating an accurate treatment of heat fluxes through different ice types, and calculated the surface heat balance for the entire Okhotsk Sea.

The heat flux estimation algorithm used in the present study (Appendix) generally follows that of *Ohshima et al.* [2003]. The main differences in our algorithm are the parameterization of ice thickness as a continuous function of ice-type parameter instead of ascribing the thickness to three discrete ice types [*Ohshima et al.*, 2003],

and choice of slightly different radiative heat flux parameterizations which were shown to be appropriate for arctic conditions [*Key et al.*, 1996]. The main benefit of using bulk parameterization of heat fluxes based on reanalyzed lower atmosphere meteorology and SSM/I ice data over the output of large-scale meteorological reanalysis models is the improvement of the resolution of ice cover and distinguishing between the various ice types. Sea ice distribution was determined using the 25-km gridded Special Sensor Microwave Imager (SSM/I) brightness temperature data [*Maslanik and Stroeve*, 1990].

For each pixel the total ice concentration and ice type were derived using the thin ice algorithm [*Cavalieri*, 1994] from the 19/37GHz gradient ratio $Gr=(T_{37V}-T_{19V})/(T_{37V}+T_{19V})$ and 19GHz polarization ratio $Pr=(T_{19V}-T_{19H})/(T_{19V}+T_{19H})$, where T_{37V}, T_{19V}, and T_{19H} are the vertically polarized 37 GHz and vertically and horizontally polarized 19 GHz SSM/I brightness temperatures, respectively. Algorithm tie points suitable for the Okhotsk Sea conditions [*Martin et al.*, 1998] were used. Three ice types, namely new, young and first year ice, were distinguished using the 19GHz polarization ratio [*Kimura and Wakatsuchi*, 1999]. These ice types (as well as the open water) were ascribed different radiative and thermodynamic properties, leading to different parameterizations of surface heat fluxes. The particular differences are mentioned in the Appendix.

The estimate of heat loss F at the ice surface takes into account turbulent sensible (F_S), latent (F_L), net shortwave (S) and longwave (L) heat fluxes:

$$F = F_S + F_L + S + L. \quad (1)$$

The fluxes are calculated using the low-resolution (~1.125-degree) ECMWF reanalysis meteorological data (10-m windspeed, 2-m air temperature, and surface atmospheric pressure) and high-resolution (25-km) ice type data (see Appendix for details). The free parameter of these calculations is the ice surface temperature T_s, which is determined by balancing the surface heat loss with the conductive heat flux through the ice.

The heat flux algorithm suffers greatly from large uncertainties in bulk heat parameterization, especially since very little opportunity for direct verification of flux estimates exists. Uncertainties in ice concentration, air temperature, and wind speed are the most important sources of error in winter [*Ohshima et al.*, 2003]. Additionally, the wintertime heat flux estimate is greatly dependent on the parameterization of thickness and thermal properties of sea ice [*Ohshima et al.*, 2003]. The primary source of error is the use of direct semi-empirical relationships of ice thickness to the ice type, while the SSM/I ice classification is strongly affected by seasonal and regional variability of radiative properties of ice surface. As a simple consistency test, the ice surface temperatures that were obtained as a by-product of heat balance estimates were compared with the surface temperatures T_{SST}, obtained by NOAA/NASA Polar Pathfinder Advanced Very High Resolution Radiometer (AVHRR) [*Fowler et al.*, 2000]. Significant cloud cover over the area in wintertime made reliable AVHRR data scarce, so an area-averaged approach had to be taken.

The heat flux method tends to underestimate the ice surface temperature in the first half of the winter (compared to AVHRR data, which is assumed to be correct),

and overestimates it in the second half (Fig. 2.2). The domain-averaged difference between T_s and T_{SST} varied from about –1.5ºC in early January to 0.4ºC in April. Standard deviation of the difference T_S-T_{SST} ranged from 1ºC to 3ºC with the maximum in late January when the diversity of ice types was the greatest. Overestimation of T_s might have resulted from the buildup of snow on the ice surface as it ages. Snow cover provides additional insulation, decreasing the conductive heat flux and surface temperature measured by AVHRR. SSM/I ice classification, however, does not fully account for this cover and consequently the conductive heat flux and the ice surface temperature may be overestimated for the case of old snow-covered ice. Older ice, however, contributes little to the total heat loss compared to the young polynya ice, which is usually free from substantial snow cover. Consequently, snow cover effects were not included in our heat flux estimate.

The satellite observations provide an independent method of validation of the heat flux algorithm, and could potentially enable the further calibration of ice thickness classification. However, the scarcity of clear-sky AVHRR images during the winter did not allow such calibration for the present study.

Without knowledge of the water temperature distribution it is not possible to determine if the heat loss leads to ice formation. In the present study we assume that the water in the immediate vicinity of ice is close to freezing, so the heat loss in pixels where ice is already present is translated into ice formation. On the other hand, we assume that water in ice-free pixels is too warm and that no significant ice formation occurs there, even though such an assumption underestimates the ice production at the initial stages of freezing. The ice concentration throughout the polynya region was

high from mid-January to the end of April, so the exclusion of open-water ice production is not expected to affect the estimate of the rate of DSW formation happening mainly during this period.

Following *Cavalieri and Martin* [1994] (hereafter referred to as CM-94) and *Martin et al.* [1998], the ice volume production (V_i), salt flux (S_F), and dense water volume production in the polynya (V_{DSW}) are given by (per unit area):

$$V_i = \frac{F}{\rho_i L}\ , \tag{2}$$

$$S_F = \rho_i V_i (s_0 - s_i) 10^{-3}, \tag{3}$$

$$V_{DSW} = \frac{S_F}{(\rho_b s_b - \rho_0 s_0) 10^{-3}}, \tag{4}$$

where F is the net surface heat loss, ρ_i=920 kg m^{-3} is the ice density, L=2.34×10^5 J kg^{-1} is the latent heat of fusion of sea ice, s_i is the ice salinity, ρ_0= 1026.25 kg m^{-3} (ρ_b= 1026.9 kg m^{-3}) and s_0=32.6 psu (s_b=33.4 psu) are water density and salinity before (after) the density enrichment by brine rejection. Note that, compared to *Martin et al.* [1998], a lower L, which is more appropriate for salt-water ice production [*Haarpaintner et al.*, 2001], as well as lower s_0 and ρ_0 consistent with the observed values [*Shcherbina et al.*, 2004], are used. Following CM-94, constant ice salinity s_i=0.31s_0 is assumed.

The obtained DSW production rates were integrated over the northwestern polynya region. For the purpose of this study, this region was empirically defined by the box shown in Fig. 2.3a. Approximately the same definition was used in *Martin et al.* [1998] and *Gladyshev et al.* [2000].

The estimated mean heat loss within the northwestern polynya during the winter of 1999-2000 was of order of 100 W m^{-2}. It reached a maximum of about 190 W m^{-2} by the end of January (Fig. 2.3b). A brief polynya closure happened on 15 February, after which the heat loss continued at a rate of about 85 W m^{-2} until 10 March. After 15 March the polynya region was covered with thick first-year ice and the heat loss dropped to about 20 W m^{-2}. The estimated heat flux corresponds to the formation of a total of 8.6×10^{12} m^3 of DSW in the NWP alone, which corresponds to the mean annual production rate of 8.6×10^{12} m^3/12 month = 0.27 Sv. Formation rates varied between 2.28 Sv in late January and 0.98 Sv in early March.

It should be mentioned that the error in the net heat flux estimate associated with the uncertainties in atmospheric forcing and ice conditions is on the order of at least 20 W m^{-2} [*Ohshima et al.*, 2003]. Consequently, our estimates of DSW production have approximately 25% error margin.

2.2 Export rates of DSW based on in-situ data

The properties of DSW and the flow field in the southern part of NWP were observed directly by bottom moorings during the winter of 1999-2000 [*Shcherbina et al.*, 2004]. The velocities measured by Acoustic Doppler Current Profilers (ADCP) at the moorings combined with the assumptions about the DSW extent (Fig. 2.4) can be used to estimate the rate of export of this watermass from its formation region.

The outer margin of dense water was found to be located between the two moorings during the ice-cover season (January – March) based on the fact that the significant density increase associated with DSW formation was observed by only the

inshore instrument [*Shcherbina et al.*, 2003; 2004]. Additionally, we assume that the new dense water extended all the way to shore and to the surface as a result of vigorous brine-driven convection in that region (Fig. 2.4b). Consequently, the DSW cross-section during this period can be estimated as $(12.5\pm4.5)\text{x}10^6$ m^2 with the uncertainty being half the cross-section area between the two instruments. The flow through the section is assumed to have been uniform since the mean velocities observed by the two moorings were nearly identical [*Shcherbina et al.*, 2004]. With a mean advection velocity of 6 cm s^{-1} (January – February), the winter dense water transport was roughly 0.75±0.27 Sv. The transport dropped to about 0.34±0.12 Sv in spring (March-April) due to decreased velocity.

A more reliable estimate of the dense water cross-section is possible at the times of the two hydrographic sections, occupied during the mooring deployment and recovery cruises in September 1999 and June 2000. On these sections DSW stands out as a well-mixed watermass bounded by sharp property gradients [*Shcherbina et al.*, 2004], which allows its clear demarcation. Similarly to *Gladyshev et al.* [2003], we define DSW as water denser than 26.7 σ_θ, as brine rejection is the primary source of ventilation of OSMW in that density range. Additionally, we use the -1˚C isotherm to bound DSW laterally (Fig. 2.4a,c). (On our sections, the 0˚C isotherm used by *Gladyshev et al.* [2003] lay outside the temperature gradient surrounding the DSW.) The cross-section of DSW, defined in this way, was $6.9\text{x}10^6$ m^2 in September and $7.7\text{x}10^6$ m^2 in June (Fig. 2.4a,c). Mean velocities are taken from the first and last week of the record of the offshore mooring, since it was located in the core of the dense

water during these periods. The resulting estimate is 0.33 Sv in June and close to 0.02 Sv in September.

2.3 Combined results: production-export model

The changes of net volume of DSW on the northwestern shelf can be parameterized by the difference of the formation and export rates estimated in the previous sections, as illustrated in Fig. 2.5. In this calculation dense water is assumed to be absent from the shelf at the beginning of the ice formation period, which is consistent with the observations [*Shcherbina et al.*, 2004]. Import of dense water from northern polynyas, though hardly negligible, is not included. After the rapid increase in January-February, the DSW volume stayed almost constant from 10 March to 5 April. Maximum DSW volume reached during that period was 4.8×10^{12} m^3, which is approximately half of the total volume (8.6×10^{12} m^3) of new DSW formed in that region. Gradual flushing of dense water from the shelf continued after the formation ceased in early April.

3 Advective approach to the production-export balance

The unique feature of the present experiment is the presence of wintertime observations of bottom water properties in the polynya region [*Shcherbina et al.*, 2003]. These observations [*Shcherbina et al.*, 2004] can potentially provide a necessary direct verification of the methods used to obtain the DSW formation and export rates in section 2.1. However, direct comparison of these integral estimates with the point mooring measurements is not possible. In order to reconcile the two approaches, the same production-export balance applied previously to the DSW as a

whole can be extended to study the evolution of individual infinitesimal parts of it, explicitly considering the effect of advection through a spatially and temporally varying polynya region.

For this purpose we consider a large number of "particles" in an idealized horizontal advection field. Each particle represents a water column with unit cross-section and is characterized by its salinity. The salinity of the particles changes as they travel under the actual spatially inhomogeneous and time-varying salinity flux field S_F, which was calculated in the previous section based on remote ice sensing and meteorology. Instantaneous mixing to the bottom is assumed, so the evolution of the salinity of a particle with time t is approximated by

$$s = \int \frac{10^3 S_F(\mathbf{x},t)}{\rho_0 h(\mathbf{x})} dt\,, \tag{5}$$

where $\mathbf{x} = \mathbf{x}(t)$ is the position of the particle, S_F is the salt flux and $h(\mathbf{x})$ is the local water depth.

This advective estimate for salinity change is compatible with the CM-94 algorithm in terms of integral rates of salt influx and export. At the same time the advective approach provides an improved view of the evolution of water properties throughout the brine rejection period. This approach accounts for the cumulative effect of spatially varying brine rejection and variations in water residence time inside the polynya. Most importantly, since the salinity of the particles passing through a certain point can be tracked, direct comparison of the estimated rate of salinity increase with the moored observations is possible. As a result, the rates of brine rejection estimated

from heat fluxes can be independently verified, providing a test of the CM-94 algorithm.

3.1 Advection field

In the absence of comprehensive observed or modeled velocity climatology, an artificial advection field is constructed based as much as possible on the flow observed at the moorings [*Shcherbina et al.*, 2003; 2004]. Without forcing or friction, the streamfunction ψ of geostrophic unstratified flow satisfies

$$\nabla\psi \times \nabla(f/h) = 0, \tag{6}$$

where f is the Coriolis parameter and h is the ocean depth [*Pedlosky*, 1987], that is the flow has to follow lines of constant planetary potential vorticity f/h. The mean velocities observed at the moorings were generally directed along the contours of f/h (Fig. 2.6), roughly supporting the above hypothesis. The solution of (6) is

$$\psi = \Psi(f/h), \tag{7}$$

where Ψ is an arbitrary function which must be determined using the information of the cross-shore flow variation. Similarly to the assumptions of section 2.2, the flow across the line connecting the moorings is assumed to be uniform. This assumption is justified by high correlation of the flow measured by the moorings [*Shcherbina et al.*, 2004], and it is minimally sufficient for definition of Ψ up to an arbitrary multiplier. Such choice of Ψ results in relatively uniform velocity over the northern and northwestern shelves with intensifications in the regions of the East Sakhalin and Kamchatka currents as well as in the northeastern corner of the basin (Fig. 2.7a).

We wish to evaluate the possible role of circulation changes in DSW evolution. The constructed velocity field was therefore modulated in time so that its value at the site of the inshore mooring matches the vertically-averaged velocity observed at that location [*Shcherbina et al.*, 2004], low-passed using a 72-hour Blackman filter (Fig. 2.7b). This modulation affects only the absolute values but not the direction of the flow, so the general flow pattern remains invariant (although it reverses in several instances). The particles are advected using the fourth order Runge-Kutta scheme with a 1-day time step. We reiterate that this scheme is introduced as a simple observation-based refinement of the bulk DSW production estimate (section 2), and is not meant to be a full simulation of the Okhotsk Sea circulation.

3.2 Monte-Carlo simulation

The domain was initially populated with 10,000 particles randomly distributed throughout the basin. The initial salinity of all particles was set to s_0=32.6 psu to match the assumed initial salinity of DSW, based on the moored observations [*Shcherbina et al.*, 2004]. (This initial salinity is also consistent with that used in section 2.1.) Particles that left the domain during the run were reintroduced at a random location within the "repopulation" region upstream of the polynya (Fig. 2.7a), representing freshwater inflow. The salinity of reintroduced particles was set to be s_0 as well.

3.3 Comparison with direct observations

The advective approach to the production-export balance captures the general tendencies of dense water formation due to brine rejection (Fig. 2.8), validating the

CM-94 parameterization of dense water formation based on surface heat fluxes. At the same time, several discrepancies between the observed and estimated salinity variations clearly show the limits of applicability of the simple production-export balance in both advective (differential) and integral forms.

The advective estimate of salinity increase at the site of the inshore mooring was 26% slower (0.017 psu/day vs. 0.023 psu/day), but continued considerably longer than was actually observed at that site. As a result, the total salinity increase was overestimated by 22% by the advective method. The slower salinity increase suggests that the estimate (3) of the salt flux associated with ice formation is biased low by a factor of 0.74, which is not unreasonable given the uncertainties in the heat flux parameterization (section 2.1). If the salt flux were adjusted so that the rates of salinity increase match the observations, the estimate of mean annual DSW formation rate made in section 2.1 would increase to 0.36 Sv. Total DSW salinity increase would be overestimated by 70% in that case due to the longer period of salinity increase inferred from the heat fluxes.

The duration of the dense water formation yielded by the advective approach depends mostly on the duration of the polynya opening rather than the heat flux parameterization. Consequently this method can be expected to predict the dates of the beginning and end of DSW formation more accurately than the amount of the salinity increase, as the former estimates are the most direct ones. Nonetheless the advective approach predicts the salinity increase at the inshore mooring site starting at least a week earlier and terminating almost a month later than was actually observed.

One of the factors missing from both the CM-94 formation estimate (section 2) and the advective estimate is the initial background stratification of the water column. The delayed onset of density increase at the bottom can be readily explained by the time necessary to overcome such stratification. It also may explain why a much slower salinity increase was observed at the offshore (deeper) mooring. The salinity observed at the offshore mooring in January was higher than the maximum salinity predicted by the advective approach for the brine rejection season (Fig. 2.8). If the latter were indeed the maximum brine salinity at that location, the convection plume would not reach the bottom there. Consequently, late autumn stratification likely played a crucial role controlling the extent of bottom penetration of the newly formed DSW.

Additionally, estimates of DSW export based on the mooring data do not account for cross-shelf eddy transport of density anomalies. As shown by modeling studies [*Gawarkiewicz and Chapman*, 1995], geostrophic adjustment of the density anomaly inside the polynya leads to the formation of a rim current at the edge of the forcing region. This current later becomes baroclinically unstable and gives rise to a series of eddies, which effectively disperse the density anomaly. These processes result in an abrupt termination of density increase despite continuous forcing [*Gawarkiewicz and Chapman*, 1995], much like the termination observed at the inshore mooring [*Shcherbina et al.*, 2004]. Gross overestimation of maximum salinity at the site of inshore mooring by the advective method might be due to the exclusion of eddy transport balancing the salt influx in late February – late March. The missing DSW eddy transport during that period can be estimated as the difference between the production and along-isobath advective export rates, giving a mean value of 0.8 Sv

from 23 February to 13 March. Consequently, the eddy transport may account for an additional 0.04 Sv of mean annual DSW export.

On the other hand, the gradual salinity decrease at the inshore mooring in spring appears to be adequately described by the along-isobath advection model. This allows us to conclude that the final salinity of DSW at the end of brine rejection season decreases towards the northeast. The advection of this gradient past the mooring is responsible for the salinity decrease observed in spring and also continuing in the autumn, as apparent from the beginning of the record. This conclusion contradicts one of the assumptions of CM-94, which postulates a uniform salinity increase of the whole watermass.

4 Conclusion

The mean annual production rate estimated from the heat loss in the northwestern polynya alone is 0.27 Sv. Comparison of the rates of salinity increase observed directly and inferred from the heat flux analysis suggests that the brine rejection rate based on heat flux data is underestimated by a factor of 0.74. Consequently, the estimate of mean annual production rate should be increased to 0.36 Sv. These estimates are consistent with the previous indirect estimates [*Martin et al.*, 1998; *Gladyshev et al.*, 2000; *Gladyshev et al.*, 2003], although direct comparison is difficult due to interannual variability. The winter of 1999-2000 was milder than usual [*Shcherbina et al.*, 2004], which may have led to a lower DSW production.

Using the directly measured velocities, the export rate of Okhotsk Sea dense shelf water in 1999-2000 was found to vary between negligible in autumn, 0.75±0.27 Sv in winter, and 0.34±0.12 Sv in spring. Assuming the spring rates of export continued

through the summer, the mean annual export rate of DSW is estimated to be 0.30 Sv. Additionally, cross-shelf eddy transport of DSW in late February – late March is estimated to contribute 0.04 Sv to the mean annual DSW export.

The estimated annual DSW formation is quite small. However, its role in the thermahaline overturn of North Pacific is significant. Theoretical [*Price and Baringer*, 1994] and observational studies in the North Atlantic [*Dickson and Brown*, 1994] and Arctic Ocean [*Fahrbach et al.*, 2001] alike show that entrainment and mixing lead to a roughly twofold increase of the volume transport of newly formed dense waters by the time they reach their equilibrium depth. Similarly, the transport of DSW in the Okhotsk Sea intensifies as the water travels southward along the Sakhalin coast. As a result, OSMW production is a factor of 3 to 4 greater than that of DSW [*Alfultis and Martin*, 1987; *Gladyshev et al.*, 2000; *Gladyshev et al.*, 2003]. Our observed DSW production rate is thus consistent (accounting for interanual variability) with the mean overturn of about 2 Sv between surface and intermediate layers [*Macdonald*, 1998; *Talley*, 2003] that sustains the NPIW.

Appendix: Calculation of heat flux

The net heat flux F_{net} consists of turbulent sensible (F_S) and latent or evaporative (F_E) heat fluxes, as well as net shortwave (F_R) and longwave (F_L) radiation:

$$F_{\text{net}} = F_S + F_E + F_R + F_L. \quad (8)$$

Sensible and latent heat fluxes are calculated using the bulk formulae

$$F_S = \rho_a c_p C_S U (T_a - T_s), \tag{9}$$

and

$$F_E = 0.622 \rho_a L C_E U (e - e_s), \tag{10}$$

where ρ_a=1.3 kg m^{-3} is the air density, c_p=1004 J kg^{-1} K^{-1} is the specific heat at constant pressure, L is the latent heat of vaporization (2.52×10^6 J kg^{-1} for water and 2.86×10^6 J kg^{-1} for ice), C_S and C_E are stability-dependent bulk transfer coefficients [*Kondo*, 1975], U is the wind speed, T_a and T_s are air and surface temperatures, e is the water vapor pressure, and e_s is the saturated water vapor pressure at the surface temperature.

ECMWF reanalysis data for 2-m surface air temperature and 10-m surface wind speed are used as T_a and U, respectively. Following *Ohshima et al.*[2003], who found a 25% difference between the ECMWF wind data and observations, U is corrected by a factor of 1.25. The water vapor pressure e is calculated as the saturated water vapor pressure at the ECMWF 2-m surface dew point temperature. The surface temperature T_s is taken to be −1.8ºC (freezing point) for water and is estimated iteratively for ice (see below).

Radiative fluxes are estimated using the parameterizations found to be optimal for arctic conditions [*Key et al.*, 1996]. For the shortwave radiation, the empirical formula by *Jacobs* [1978] gives:

$$F_R = (1 - \alpha)(1 - 0.33C) F_{R0}, \tag{11}$$

where α is the surface albedo, C=0.7 is the mean fractional cloud cover, and F_{R0} is the mean daily incoming solar radiation, estimated using *Zillman* [1972] empirical

formula. Albedos of 0.06, 0.27, 0.36, and 0.64 were assumed for open water, new, young, and first-year ice, respectively [*Ohshima et al.*, 2003]. Longwave radiation is estimated as

$$F_L = \varepsilon_s \sigma T_s^4 - \varepsilon_a \sigma T_a^4 \ , \tag{12}$$

where ε_s is the surface emissivity (0.97 for water, 0.99 for ice), σ=5.67×10^{-8} W m^{-2} K^{-4} is the Stefan-Boltzman constant, and ε_a is the effective atmosphere emissivity, given by combining the empirical formulae of *Efimova* [1961] and *Jacobs* [1978]:

$$\varepsilon_a = (0.746 + 0.0066e)(1 + 0.26C), \tag{13}$$

where e is the water vapor pressure.

For the ice-covered areas the net surface flux should be equal to the conductive heat flux through the ice

$$F_c = k(T_w - T_s)/d \ , \tag{14}$$

where k=2.1 W m^{-1} K^{-1} is the ice heat conductivity, T_w is the water temperature, and d is the ice thickness.

The ice thickness is the major uncertainty in estimation of the ice heat fluxes, as it has to be estimated using the SSM/I data without much observational background. Based on historical data, *Ohshima et al.* [2003] used the values of 5, 20 and 80 cm for new, young, and first-year ice, respectively; 16-cm snow cover was also assumed for the first-year ice bringing its "effective" thickness to 1.85 m. For the present study we chose d to be an empirical piece-wise linear function of the ice type parameter, which was derived from the 19GHz polarization ratio [*Kimura and Wakatsuchi*, 1999]. This

choice led to a more natural continuous ice thickness variation: 5-10 cm for new, 10-30 cm for young, and 30-80 cm for first year ice.

The ice surface temperature that satisfies the balance $F=F_c$ was computed iteratively, starting with $T_s=0.6T_a$. On each iteration step the surface heat fluxes were estimated using (8) and then (14) was used to obtain the updated ice surface temperature that satisfies the balance. Just a few iterations were enough to achieve a stable value of T_s.

Acknowledgements. This work was supported through the National Science Foundation grant OCE-9811958 and by Hokkaido University (ship support). Technical support was provided by the Oceanographic Data Facility and the Instrument Development Group at Scripps Institution of Oceanography (SIO), and by the captain and crew of the R/V Professor Khromov. We thank S. Gladyshev, K. Ohshima, and S. Martin for helpful discussion of heat flux calculations in the ice-covered Okhotsk Sea.

References:

Alfultis, M. A. and S. Martin, Satellite passive microwave studies of the Sea of Okhotsk ice cover and its relation to oceanic processes, *J. Geophys. Res.*, 92, 13013-13028, 1987.

Cavalieri, D., A microwave technique for mapping thin sea ice, *J. Geophys. Res.*, 99, 12561-12572, 1994.

Cavalieri, D. J. and S. Martin, The contribution of Alaskan, Siberian, and Canadian coastal polynyas to the cold halocline layer of the Arctic Ocean, *J. Geophys. Res.*, 99(C9), 18343-18362, 1994.

Dickson, R. R. and J. Brown, The production of North Atlantic Deep Water: sources, rates, and pathways, *J. Geophys. Res.*, 99, 12319-12341, 1994.

Efimova, N. A., On methods of calculating monthly values of net longwave radiation, *Meteorol. Gidrol.*, 10, 28-33, 1961.

Fahrbach, E., S. Harms, G. Rohardt, M. Schröder, and R. Woodgate, Flow of bottom water in the northwestern Weddell Sea, *J. Geophys. Res.*, 106, 2761-2778, 2001.

Fowler, C., J. Maslanik, T. Haran, T. Scambos, J. Key, and W. Emery, AVHRR Polar Pathfinder twice-daily 5 km EASE-Grid composites, http://nsidc.org/data/nsidc-0066.html, National Snow and Ice Data Center, Boulder, CO., 2000, updated 2002.

Gawarkiewicz, G. and D. Chapman, A numerical study of dense water formation and transport on a shallow, sloping continental shelf, *J. Geophys. Res.*, 100, 4489-4507, 1995.

Gladyshev, S., S. Martin, S. Riser, and A. Figurkin, Dense water production on the

northern Okhotsk shelves: comparison of ship-based spring-summer observations for 1996 and 1997 with satellite observations, *J. Geophys. Res.*, 105, 26281-26299, 2000.

Gladyshev, S., L. Talley, G. Kantakov, G. Khen, and M. Wakatsuchi, Distribution, formation, and seasonal variability of Okhotsk Sea Mode Water, *J. Geophys. Res.*, 108(C6), 3186, doi: 10.1029/2001JC000877, 2003.

Haarpaintner, J., J. C. Gascard, and P. M. Haugan, Ice production and brine formation in Storfjorden, Svalbard, *J. Geophys. Res.*, 106(C7), 14001-14013, 2001.

Itoh, M., K. I. Ohshima, and M. Wakatsuchi, Distribution and formation of Okhotsk Sea Intermediate Water: an analysis of isopycnal climatological data, *J. Geophys. Res.*, 108(C8), 3258, doi: 10.1029/2002JC001590, 2003.

Jacobs, J. D., Radiation climate of Broughton Island. Energy budget studies in relation to fast-ice breakup processes in Davis Strait, in *Occas. Pap. 26*, edited by R. G. Barry and J. D. Jacobs, pp. 105-120, Inst. of Arctic and Alp. Res., Univ. of Colorado, Boulder, 1978.

Key, J. R., R. A. Silcox, and R. S. Stone, Evaluation of surface radiative flux parameterizations for use in sea ice models, *J. Geophys. Res.*, 101(C2), 3839-3849, 1996.

Kimura, N. and M. Wakatsuchi, Processes controlling the advance and retreat of sea ice in the Sea of Okhotsk, *J. Geophys. Res.*, 104(C5), 11137-11150, 1999.

Kitani, K., An oceanographic study of the Okhotsk Sea - particularly in regard to cold waters, *Bull. Far Seas Fish. Res. Lab.*, 9, 45-76, 1973.

Kondo, J., Air-sea bulk transfer coefficient in diabatic conditions, *Bound.-Layer*

Meteor, 9, 91-112, 1975.

Macdonald, A. M., The global ocean circulation: a hydrographic estimate and regional analysis, *Prog. in Oceanogr.*, 41, 281-382, 1998.

Martin, S., R. Drucker, and K. Yamashita, The production of ice and dense shelf water in the Okhotsk Sea polynyas, *J. Geophys. Res.*, 103, 27771-27782, 1998.

Maslanik, J. and J. Stroeve, DMSP SSM/I daily polar gridded brightness temperatures, CD-ROM, National Snow and Ice Data Center, Boulder, CO., 1990, updated 2003.

Ohshima, K. I., T. Watanabe, and S. Nihashi, Surface heat budget of the Sea of Okhotsk during 1987-2001 and the role of sea ice on it, *J. Meteor. Soc. Japan*, 81(4), 653-677, 2003.

Pedlosky, J., Geophysical fluid dynamics, 2nd ed., Springer-Verlag, New York, 1987.

Price, J. F. and M. Baringer, Outflows and deep water production by marginal seas, *Progr. Oceanog.*, 33, 161-200, 1994.

Shcherbina, A. Y., L. D. Talley, and D. L. Rudnick, Direct observations of North Pacific ventilation: brine rejection in the Okhotsk Sea, *Science*, 302(5652), 1952-1955, 2003.

Shcherbina, A. Y., L. D. Talley, and D. L. Rudnick, Dense water formation on the northwestern shelf of the Okhotsk Sea. Part I: direct observations of brine rejection, *J. Geophys. Res.*, in press, 2004.

Talley, L., Distribution and formation of the North Pacific Intermediate Water, *J. Phys. Oceanogr.*, 23, 517-537, 1993.

Talley, L. D., An Okhotsk water anomaly: implications for ventilation in the North Pacific, *Deep Sea Res.*, 38(Suppl. 1), S171-S190, 1991.

Talley, L. D., Shallow, intermediate, and deep overturning components of the global heat budget, *J. Phys. Oceanogr.*, 33, 530-560, 2003.

Wong, C. S., R. J. Matear, H. J. Freeland, F. A. Whitney, and A. S. Bychkov, WOCE line P1W in the Sea of Okhotsk. Part 2: CFCs and the formation rate of intermediate water, *J. Geophys. Res.*, 103(C8), 15625-15642, 1998.

Yasuda, I., The origin of the North Pacific Intermediate Water, *J. Geophys. Res.*, 102, 893-909, 1997.

Zillman, J. W., A study of some aspects of the radiation and heat budgets of the southern hemisphere oceans, *Meteorol. Stud. Rep. 26*, Bur. of Meteorol., Dep. of the Inter., Canberra, Australia, 1972.

Figures:

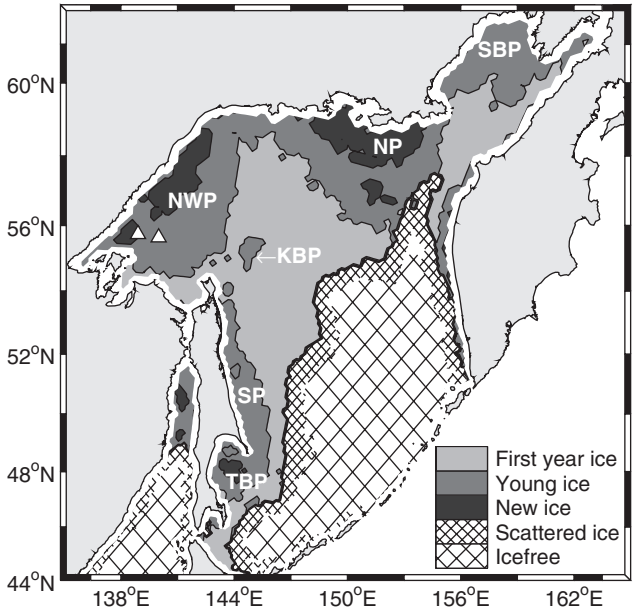

Fig. 2.1. Ice distribution in the Okhotsk Sea on 1 February 2000, showing the persistent polynyas: Shelikhov Bay (SBP), northern (NP), northwestern (NWP), Kashevarov Bank (KBP), Sakhalin (SP) and Terpeniya Bay (TBP). Ice classification based on National Snow and Ice Data Center SSM/I brightness temperatures. White triangles show the bottom mooring positions.

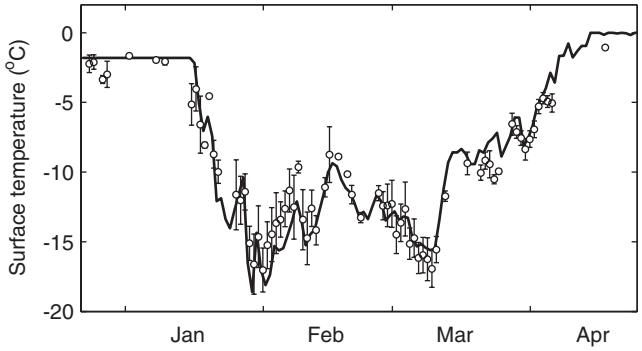

Fig. 2.2. Ice surface temperature inferred via heat balance (line) and observed by AVHRR (dots). Average within a 50km radius of (146ºE, 57ºN) is shown. One standard deviation error bars are shown for AVHRR data

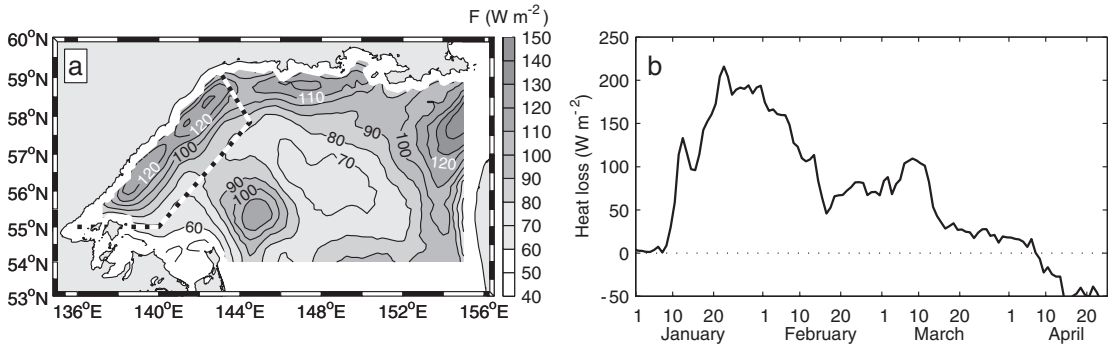

Fig. 2.3. (a) Surface heat loss in the northern Okhotsk Sea (average over the period from 10 January to 10 April 2000). (b) Time series of mean heat loss from the northwestern polynya region (marked with dashed line in (a)). Heat loss in absence of ice formation is disregarded.

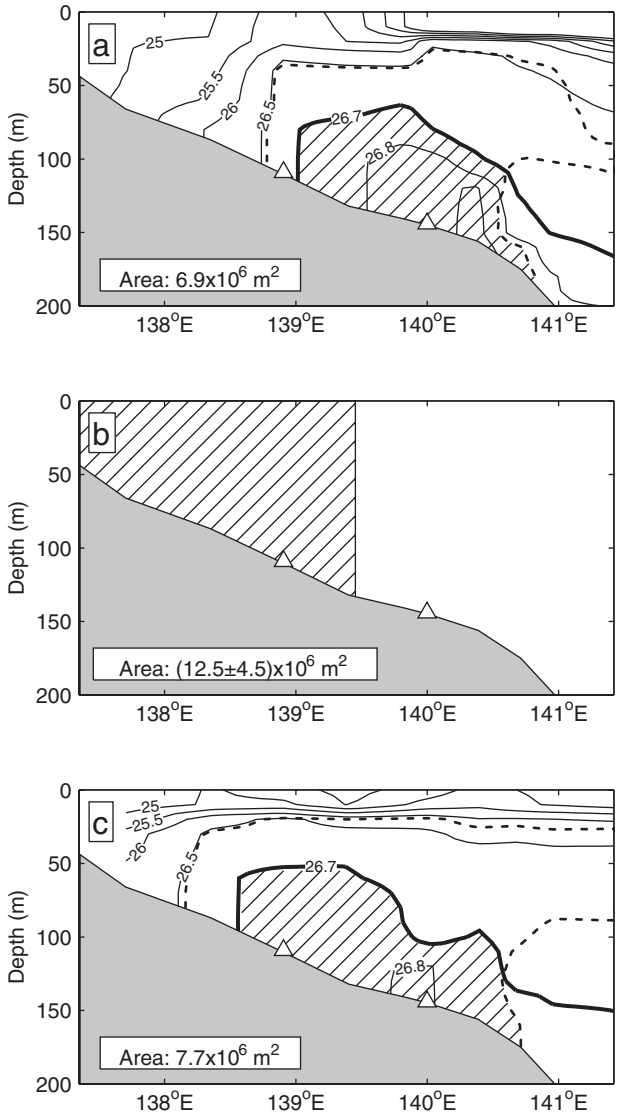

Fig. 2.4. Estimated DSW cross-section (hatched) in (a) autumn, (b) winter, and (c) spring. Solid contours in (a) and (c) show potential density distribution in September 1999 and June 2000 correspondingly. Thicker contours correspond to σ_θ =26.7 isopycnals. Dashed contours show -1ºC isotherm. White triangles indicate the location of bottom moorings.

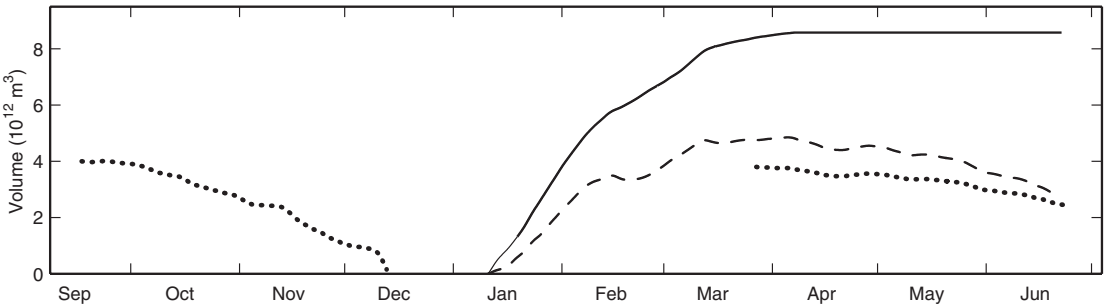

Fig. 2.5. Volume of DSW in the NWP region estimated via brine rejection rates based on SSM/I ice concentration data and ECMWF reanalysis meteorology (solid black line). The same estimate but corrected for the wintertime export, estimated in section 2.1 using the moored velocity data (dashed black line). Integrals of fall and spring export estimates based on hydrographic data and moored velocity data (dotted lines) are shown for reference, arbitrarily offset.

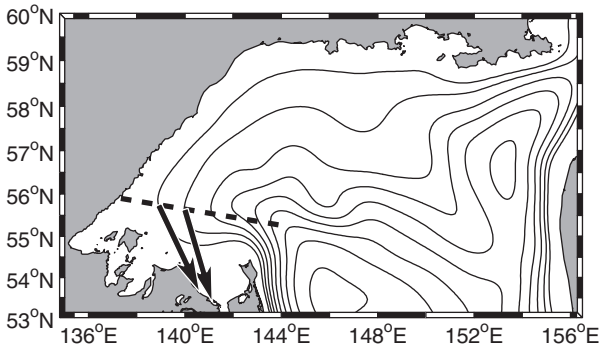

Fig. 2.6. Planetary potential vorticity, *f/h*. The contour interval varies to produce evenly-spaced contours. Arrows show the mean velocity observed at the moorings. Line of assumed constant velocity is also shown (dashed).

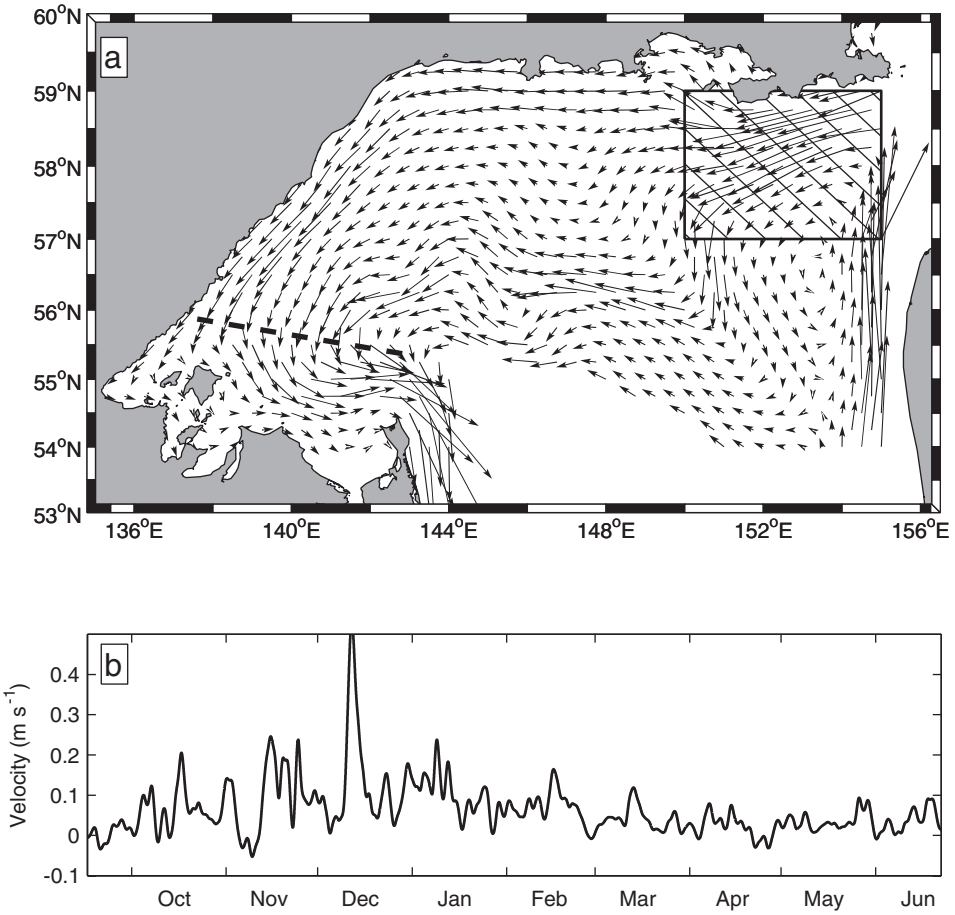

Fig. 2.7. (a) Flow field used in the advective approach and (b) temporal variation of the flow amplitude, based on moored observations. Line of assumed constant velocity (dashed) and "repopulation" region (hatched) are also shown in (a).

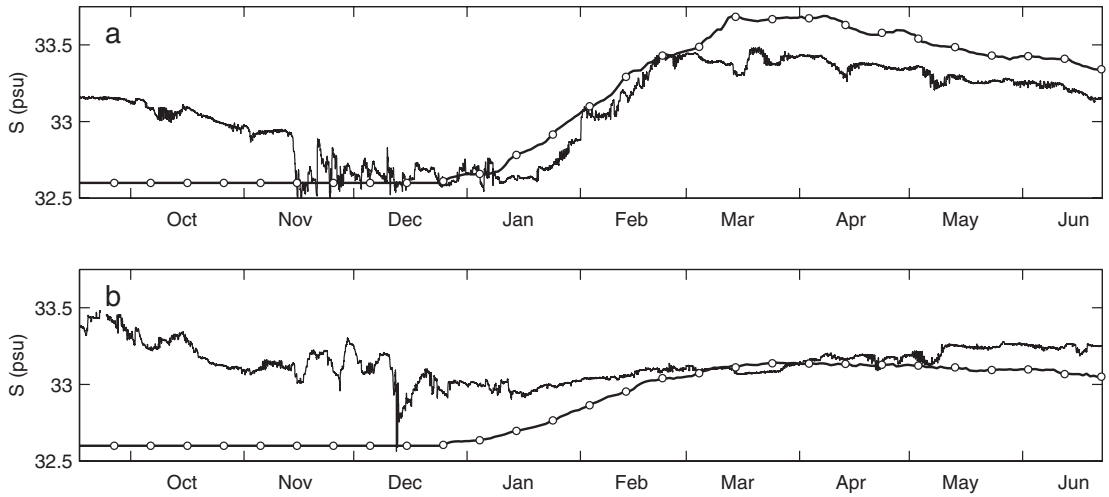

Fig. 2.8. Advective estimate of DSW salinity evolution (line marked with dots every 10 days) and observed (solid line) salinity at the sites of the (a) inshore and (b) offshore moorings.

CHAPTER III

Tidal Bottom Boundary Layer Structure

Abstract. The tidal bottom boundary layer structure on the northwestern shelf of the Okhotsk Sea was investigated using two bottom-mounted Acoustic Doppler Current Profilers (ADCPs) at 110 and 140 m depth. Clear Ekman spiraling was evident in rotary tidal components at M_2 tidal frequency. Vertical and temporal variations of vertical eddy viscosity coefficient were obtained from the parameters of this spiraling. Mean eddy viscosity was estimated to be 5.9×10^{-3} m^2 s^{-1} and 3.8×10^{-3} m^2 s^{-1} at the inshore and offshore moorings, respectively. A slight decrease of eddy viscosity was distance from the bottom was observed at both sites. Wintertime decrease in eddy viscosity likely associated with active brine rejection occurred at the inshore mooring. At the same time eddy viscosity at the offshore mooring was elevated relative to the mean value. Such difference in the behavior of the tidal boundary layer corresponds to the differences in wintertime watermass evolution regimes, identified based on the hydrographic data.

1 Introduction

The Okhotsk Sea is a marginal semi-enclosed sea in the subpolar gyre of the northwestern Pacific (Fig. 1.1a). Wide continental shelf areas in the northern part of the sea give rise to high tidal amplitudes in these areas (Fig. 1.1b). At the same time, the northern and northwestern shelves are the site of the Okhotsk Sea Dense Shelf Water (DSW) formation, a key watermass in the North Pacific intermediate-layer overturn [*Kitani*, 1973; *Talley*, 1991; *Gladyshev et al.*, 2000]. *Shcherbina et al.* [2004] showed that the evolution of a tidal mixing front on the northwestern shelf plays an important role in the DSW formation cycle. Due to the difficulty of wintertime access, seasonal variability of tidal boundary layer dynamics in this region is poorly investigated.

In 1999-2000 the first direct observations of wintertime watermass evolution on the northwestern shelf of the Okhotsk Sea were made with two bottom moorings [*Shcherbina et al.*, 2003; *Shcherbina et al.*, 2004]. In particular, measurements of vertical current structure were made using moored Acoustic Doppler Current Profilers (ADCPs).

Studies of the tidal bottom boundary layer in other shelf regions have revealed a strong dependence of the dynamics of the layer on stratification [*Maas and van Haren*, 1987; *Werner et al.*, 2003]. In both studies the authors attempted to reproduce the vertical structure of tidal currents based on analytical [*Maas and van Haren*, 1987] or numerical [*Werner et al.*, 2003] reconstruction of the eddy viscosity profile. A priori knowledge of the density profile is crucial for such reconstruction.

In contrast to the studies of *Maas and van Haren* [1987] and *Werner et al.* [2003], no information about vertical stratification was available in our experiment. On the other hand, the strong and regular tides observed at the moorings allowed estimation of eddy viscosity based solely on vertical profiles of the tidal currents.

Section 2 of this paper presents the mooring data used in the study. Section 3 describes the observed vertical structure of tidal boundary layers and the procedure of eddy viscosity estimation. Section 4 discusses the observed variation of eddy viscosity in the context of wintertime watermass transformation on the northwestern shelf of the Okhotsk Sea.

2 Data

In situ observation of the shelf processes was made using an array of four bottom moorings deployed on the northwestern shelf of the Okhotsk Sea in September 1999, two of which were successfully recovered in June 2000. The two surviving moorings were located at (55°45'N, 138°54'E) and (55°39'N, 140°00'E) in 109 and 144 m of water correspondingly, and will be hereafter referred to as the "inshore" (western, shallower) and the "offshore" (eastern, deeper) moorings (Fig. 1.1a).

Each mooring was equipped with a Seabird Seacat CTD and an upward-looking 300-kHz broadband RD Instruments Acoustic Doppler Current Profiler (ADCP). Pressure, salinity, temperature and oxygen concentration were recorded with a 15-minute sampling interval. The ADCPs provided velocity data with 4-m vertical and 16-minute temporal resolution. The first useable bin was located 14.1 m above the bottom. Due to the lack of scatterers in the water column throughout the year and especially in winter, only a 20-50% data return rate was observed in near-surface

(maximum range) layers. The range of 95% data return rate was at 50 and 60 m above the bottom at the inshore and offshore moorings, respectively.

3 Tides on the northwestern shelf of the Okhotsk Sea

The tidal signal at both moorings was much stronger than the mean flow, with amplitudes reaching 50 cm/s. The major tidal component was M2 with amplitudes of approximately 29 cm/s at the inshore mooring and 21 cm/s at the offshore one (Fig. 3.2a). The second largest component was S2 with the amplitudes of 10 and 7 cm/s, correspondingly (Fig. 3.2a). All components exhibited strong elliptical polarization (ratio of the major to minor axis of about 6), with major axes nearly perpendicular to the isobaths (Fig. 3.2). In the near-bottom layers, the axis of the ellipses veers clockwise, while their aspect ratio decreases. Such behavior is the clear evidence of the bottom friction effects [*Maas and van Haren*, 1987], and will be discussed in detail in section 3.1. Vertical profiles of rotary tidal components will also be used to estimate the temporal and spatial variability of vertical eddy diffusivity coefficient in section 3.2.

3.1 Tidal bottom boundary layer

It is customary to represent an elliptically polarized tidal current as a composition of two counter-rotating components [*Prandle*, 1982]:

$$R = R_{+}e^{i\omega t} + R_{-}e^{-i\omega t},$$

where $R=u+iv$ is the complex velocity, $\omega=2\pi/T$ is the tidal frequency (for M_2 tide T=12.42 hours and $\omega=1.41\text{x}10^{-4}$ s^{-1}), and R_{+}, R_{-} are the complex amplitude of counterclockwise- and clockwise-rotating component correspondingly.

The complex amplitudes of the two components at each depth level were extracted from the velocity data using a Fourier transform. Their mean vertical profiles at both moorings exhibit clear boundary layer structures (Fig. 1.12b-c).

The structure of such rotational boundary layers is similar to that of surface Ekman layers [*Prandle*, 1982; *Maas and van Haren*, 1987]. Vertical profiles of complex rotational amplitudes can be shown to follow

$$R_{\pm}(z) = R_{0\pm}\left(1 - \frac{\exp\{-\alpha_{\pm} z\}}{1 + \alpha_{\pm} / s_{\pm}}\right), \tag{15}$$

where z is the distance above the bottom, $s_{\pm} = r_{\pm}/k$, where $r_{\pm}$ is the bottom resistance coefficient with dimensions of velocity [*Csanady*, 1982], k is the vertical eddy viscosity coefficient, $\alpha_{\pm} = (1 \mp i)/\delta_{\pm}$, and $\delta_{\pm}$ are the Ekman layer depths for the two components :

$$\delta_{\pm} = \sqrt{\frac{2k}{\omega \pm f}}, \tag{16}$$

where f is the Coriolis parameter. (For simplicity $\omega > f$ is assumed, which is the case for the M_2 frequency equatorward of 75° latitude.) The Ekman layer depths for the two counter-rotating components are consequently expected to be significantly different, with the separation especially prominent in mid-latitude for the semi-diurnal components, where $\omega \gtrsim f$ [*Soulsby*, 1983].

The observed rotary component profiles (Fig. 1.12b-c) agree reasonably well with the theoretical prediction based on (15). The free parameters ($R_{0\pm}$, $\alpha_{\pm}$, and $s_{\pm}$) in (15) were determined by a non-linear least-squares fit of (15) to the complex profiles of $R_{\pm}$ at each mooring (Table 3.1). Only the bottom halves of the profiles were used for

fitting the data, as the upper portions of the profiles appear to be affected by missing data (see section 2), which results in an inadequate fit if the whole profiles are used. The fitting procedure produced the Ekman layer depths δ_+=11.61 m and δ_-=23.65 m for the inshore mooring and δ_+=9.56 m and δ_-=19.0 m for the offshore one. In both cases the ratio δ_-/δ_+ was close to 2.0, which is significantly lower then the expected value $[(\omega+f)/(\omega-f)]^{1/2}$=3.5. The most obvious explanation of the source of this discrepancy is an overestimation of δ_+.

The values of bottom resistance coefficient $r_\pm$ determined by the fit were $r_+=5\text{x}10^{-4}$ m s^{-1}, and $r_-=8\text{x}10^{-4}$ m s^{-1} for the inshore mooring and $r_+=3\text{x}10^{-4}$ m s^{-1} and $r_-=1\text{x}10^{-3}$ m s^{-1} for the offshore one. The bottom resistance coefficient appears in (15) as a result of linearization of the bed friction boundary condition [*Csanady*, 1976]. For the case of oscillatory flow the theoretical values of r_+ and r_- are generally not equal and depend on amplitudes and phases of all tidal constituents [*Heaps*, 1978]. We do not attempt to study the agreement of $r_\pm$ with theory here, and give the obtained values just for reference. These values agree to the order of magnitude with the values quoted previously [*Scott and Csanady*, 1976; *Bennett and Magnell*, 1979].

The determination of δ_+ is inherently less robust due to the low number of depth bins within the thinner counterclockwise boundary layer. Besides, the measurements did not extend closer than 14 m to the bottom (section 2), so only the outermost portion of the counterclockwise boundary layer was sampled. However vertical variation of both the amplitude and the phase of the R_+ profiles consistent with the presence of a boundary layer with δ_+~10 m was observed over at least the 4 deepest bins with both instruments, so an overestimation by a factor of 1.75 is unlikely.

A shift of the effective Coriolis frequency f due to the presence of large-scale vorticity could also change the ratio of vertical lengthscales. In order to produce the observed apparent underestimate of δ_- / δ_+, however, mean anticyclonic background vorticity of order of $0.3f$ is necessary, which is unlikely taking into account the general cyclonic circulation in the region. Presently, the discrepancy appears to be not reconciled.

Ignoring the possible changes of the effective Coriolis frequency and using the clockwise Ekman depth, the mean vertical eddy viscosity coefficient $k_- = (\omega - f)\delta_-^{\,2}/2$ is estimated to be $5.9\text{x}10^{-3}$ m^2 s^{-1} at the inshore mooring and $3.8\text{x}10^{-3}$ m^2 s^{-1} at the offshore one. The same estimates using the counterclockwise Ekman depth would be roughly 3 times larger. The thicker clockwise boundary layer is much better resolved than the counterclockwise one. Consequently the estimates of vertical viscosity based on δ_- are preferred to those based on δ_+. The mean value of vertical eddy viscosity at the inshore mooring is higher than that at the offshore one, which is consistent with the higher tidal amplitudes and shear production at the shallower (inshore) site (see the next section).

3.2 Estimation of vertical eddy viscosity

Deviation of the observed profiles from (15) in the upper half of the water column (Fig. 1.12b-c) is partly due to the increasing amount of missing data, but may also suggest vertical variation of eddy viscosity k. The extent of such variation can be estimated from the mooring data. As above, only the clockwise component is used, as it is better resolved.

Assuming (15) is locally valid even for variable *k,* it follows that:

$$\arg\left[\frac{dR_-}{dz}\right] = \frac{z}{\delta_-} + C\,, \tag{17}$$

where C is a constant. Thus the local value of k is given by

$$k = \frac{\omega - f}{2}\delta_-^{\,2} = \frac{\omega - f}{2}\left(\frac{d}{dz}\arg\left[\frac{dR_-}{dz}\right]\right)^{-2} = \frac{\omega - f}{2}\left(\frac{da_-}{dz}\right)^{-2}\,, \tag{18}$$

where $a_-=\arg[dR_-/dz]$ is the rotary shear phase.

Clockwise rotary components R_- were extracted from the velocity data at each depth using a Gaussian window with the length T_w equal to 10 M_2 tidal periods (approximately 5 days). Vertical derivatives of the rotary shear phase $a_z=da_-/dz$ were then computed and temporarily averaged. (Averaging of the intermediate quantity a_z is preferable to the averaging of the final result, since the former is distributed roughly normally, while the distribution of the latter is substantially skewed.) Finally, the eddy viscosity variation was estimated as

$$k=0.5(\omega\text{-}f)\langle a_z\rangle^{-2}, \tag{19}$$

where angle brackets represent a temporal mean. The obtained profiles of mean vertical eddy viscosity are shown Fig. 3.5.

The confidence intervals of estimates of eddy viscosity can be directly derived from the corresponding confidence intervals of $\langle a_z\rangle$. Assuming normal distribution of a_z, the 90% confidence interval of $\langle a_z\rangle$ can be taken as $\pm 1.66\sigma_{\langle a_z\rangle}$, where $\sigma_{\langle a_z\rangle}$ is the standard deviation of the mean. The latter is given by

$$\sigma_{<a_z>} = \sigma / \sqrt{M} \ , \qquad (20)$$

where M is number of degrees of freedom in the average. We assume that Gaussian windows with 50% overlap provide virtually independent spectral estimates [*Harris*, 1978], which gives the effective number of degrees of freedom $M=2T/T_w \approx 108$, where T=280 days is the length of the record.

The vertical profile of k derived from the velocity data of the inshore mooring shows an increase of eddy viscosity towards the bottom (Fig. 3.5a) reaching 7.7×10^{-3} m^2 s^{-1} 18 m above the bottom. The apparent increase of k towards the surface is likely statistically insignificant as the profile becomes excessively noisy due to the increased fraction of missing velocity data. The vertical profile of k inferred from the offshore mooring data (Fig. 3.5b) is more uniform, with the near-bottom value of 3.8×10^{-3} m^2 s^{-1}.

Time series of near-bottom vertical eddy viscosity (Fig. 3.7) were obtained by fitting straight lines to the individual profiles of $a_-(z_i)=\arg[dR_-/dz]$. The fit was performed only within 32 m off the bottom (5 vertical levels) to reduce the effects of vertical variability. The slopes of the lines provided the estimate of $<a_z>$, which was then converted to the vertical eddy viscosity estimates using (19). Calculation of confidence intervals of the time series of k is similar to that described above for its mean vertical profile. The standard deviation $\sigma_{<a_z>}$ of $<a_z>$ obtained by least squares line fitting is given by

$$\sigma_{<a_z>} = \sqrt{\frac{\sum \sigma_i^{-2}}{\Delta}}, \tag{21}$$

where σ_i is the standard deviation of individual values of a_i, $\Delta = \sum \sigma_i^{-2} \sum z_i^2 \sigma_i^{-2} - \left(\sum z_i \sigma_i^{-2}\right)^2$, and z_i is the vertical coordinates of the data points [1988]. Temporal variation of σ_i at each depth was estimated from the data using a 2-week window.

The lowest vertical eddy viscosity 1×10^{-3} m^2 s^{-1} was observed at the inshore mooring in mid-February (Fig. 3.6a). On the other hand the viscosity at the offshore mooring (Fig. 3.7a) was elevated from January to March. The difference in qualitative behavior of the vertical viscosity at the two moorings was possibly due to the difference in wintertime stratification regimes at these locations that will be discussed in the following section.

4 Discussion

According to the study of wintertime evolution of hydrographic properties [*Shcherbina et al.*, 2003; *Shcherbina et al.*, 2004], the two mooring sites were located within two different regimes during the winter of 1999-2000. Persistent salinity increase was observed at the inshore mooring from mid-January to end of February, while the temperature stayed close to the freezing point (Fig. 3.6b). *Shcherbina et al.* [2003] attributed this salinity increase to Dense Shelf Water (DSW) formation, driven by intense brine rejection driven in the northwestern polynya. On the other hand, salinity at the offshore mooring stayed nearly constant, with only a mild increase likely due to due to the gradual mixing with the dense water inside the polynya and upstream

advection (Fig. 3.7b). Such a regime difference was unexpected, since the moorings were less than 70 km apart and were both located within the active heat loss area of the northwestern polynya, as determined by remote sensing of the ice cover [*Shcherbina et al.*, 2004]. A clear distinction between the near-bottom mixing regimes at the two sites is also evident from the comparison of vertical eddy diffusivity time series (Fig. 3.6a, Fig. 3.7a).

Brine rejection at the inshore mooring was preceded by a peak in eddy viscosity on 10-15 January 2000 reaching 2 $m^2 s^{-1}$, which was likely due to the loss of vertical stability caused by cooling of the water column to the freezing temperature. However, once the active brine rejection started on January 20, the vertical eddy viscosity dropped, reaching 10^{-3} $m^2 s^{-1}$ by mid-February. Based on indirect evidence of bottom potential supercooling and heat flux analysis, brine rejection at the site of inshore mooring continued until mid-March despite the earlier termination of salinity increase [*Shcherbina et al.*, 2004]. Consequently, the period of lower eddy diffusivity in late January – early March 2000 coincides well with the period of brine rejection and DSW formation at this site. This coincidence may be due to the increased near-bottom stratification in the plume of newly-formed DSW which would suppress the shear turbulence production.

In contrast with the inshore mooring, vertical eddy viscosity at the offshore mooring was elevated to the values of 10^{-2} $m^2 s^{-1}$ from mid-January to end of March 2000, compared to

10^{-3} $m^2 s^{-1}$ in late December and in April-June. This suggests that the weak

stratification persisted at the offshore mooring site throughout the winter, reflecting the lack of brine-driven convection there.

No vertical stratification data were collected during the present experiment, so a direct relationship between the observed variation of vertical eddy viscosity and stratification changes cannot be established. However, the observed fluctuations of near bottom friction stress the importance of inclusion of shelf dynamics in the models of dense shelf water production.

Acknowlegements. This work was supported through the National Science Foundation OCE-9811958 and by Hokkaido University (ship support). Technical support was provided by the Oceanographic Data Facility and the Instrument Development Group at Scripps Institution of Oceanography (SIO), and by the captain and crew of the R/V Professor Khromov.

References:

Bennett, J. R. and B. A. Magnell, A dynamical analysis of currents near the New Jersey coast, *J. Geophys. Res.*, 84, 1165-1175, 1979.

Csanady, G. T., Mean circulation in shallow seas, *J. Geophys. Res.*, 81(30), 5389-5399, 1976.

Csanady, G. T.,Circulation in the coastal ocean, D. Reidel Publishing Company, Dordrecht/Boston/London, 1982.

Gladyshev, S., S. Martin, S. Riser, and A. Figurkin, Dense water production on the northern Okhotsk shelves: comparison of ship-based spring-summer observations for 1996 and 1997 with satellite observations, *J. Geophys. Res.*, 105, 26281-26299, 2000.

Harris, F. J., On the use of windows for harmonic analysis with the discrete Fourier transform, *Proc. IEEE*, 66(1), 1978.

Heaps, N. S., Linearized vertically-integrated equations for residual circulation in coastal seas, *Dtsch. hydrogr. Z.*, 5, 147-169, 1978.

Kitani, K., An oceanographic study of the Okhotsk Sea - particularly in regard to cold waters, *Bull. Far Seas Fish. Res. Lab.*, 9, 45-76, 1973.

Maas, L. and J. van Haren, Observations on the vertical structure of tidal and inertial currents in the central North Sea, *Journal of Marine Research*, 45(2), 293-318, 1987.

Prandle, D., The vertical structure of tidal currents, *Geophys. Astrophys. Fluid Dynamics*, 22, 29-49, 1982.

Press W. H., B. P. Flannery, S. A. Teukolsky, and W. T. Vetterling , Numerical Recipes in C: the art of scientific computing,Cambridge; New York: Cambridge University Press, 1988.

Scott, J. T. and G. T. Csanady, Nearshore currents off Long Island , *J. Geophys. Res.*, 81(30), 5401-5409, 1976.

Shcherbina, A. Y., L. D. Talley, and D. L. Rudnick, Direct observations of North Pacific ventilation: brine rejection in the Okhotsk Sea, *Science*, 302(5652), 1952-1955, 2003.

Shcherbina, A. Y., L. D. Talley, and D. L. Rudnick, Dense water formation on the northwestern shelf of the Okhotsk Sea. Part I: direct observations of brine rejection, *J. Geophys. Res.*, 2004.

Soulsby, R. L., The bottom boundary layer of the shelf seas, in *Physical oceanography of coastal and shelf seas*, edited by B. Johns, pp. 189-266, Elsevier Science Publ. Company, Inc., N.Y. 1983.

Talley, L. D., An Okhotsk water anomaly: implications for ventilation in the North Pacific, *Deep Sea Res.*, 38(Suppl. 1), S171-S190, 1991.

Werner, S. R., R. C. Beardsley, S. J. Lentz, D. L. Hebert, and N. S. Oakey, Observations and modeling of the tidal bottom boundary layer on the southern flank of Georges Bank, *J. Geophys. Res.*, 108(C11), 8005, DOI: 10.1029/2001JC001271, 2003.

Tables and Figures:

Mooring	CW			CCW			δ_- / δ_+
	δ_-, m	r_-, m s^{-1}	k_-, m^2 s^{-1}	δ_+, m	r_+, m s^{-1}	k_+, m^2 s^{-1}	
Inshore	23.65	8×10^{-4}	5.9×10^{-3}	11.61	5×10^{-4}	1.8×10^{-2}	2.04
Offshore	19.00	1×10^{-3}	3.8×10^{-3}	9.56	3×10^{-4}	1.2×10^{-2}	1.99

Table 3.1 Parameters of clockwise (CW) and counterclockwise (CCW) bottom Ekman spirals at the two moorings.

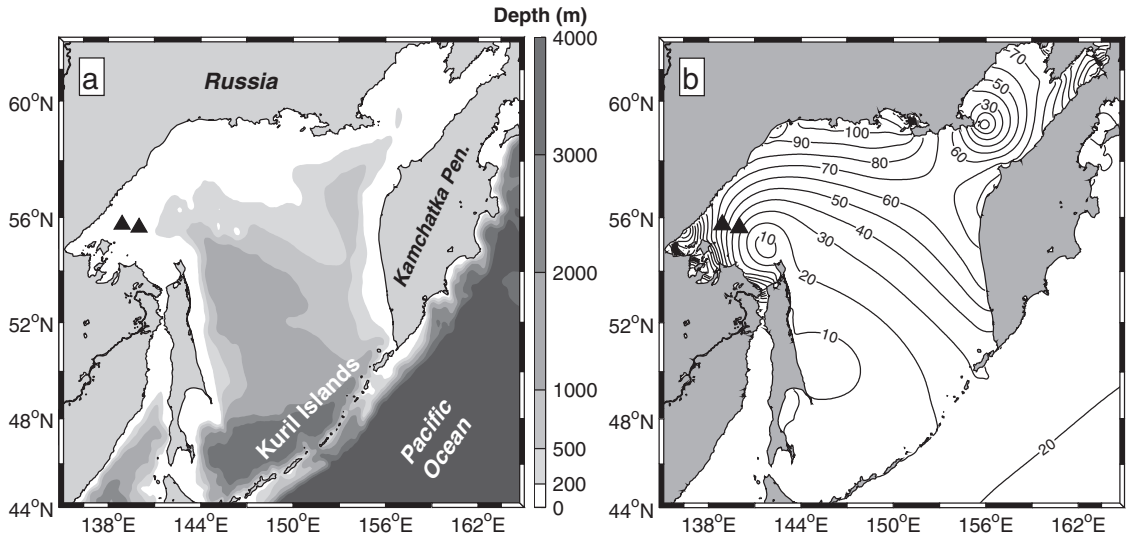

Fig. 3.1 The Okhotsk Sea. (a) Topography and (b) surface elevation amplitude of M_2 tide (in cm) based on OSU Inverse Tidal Model. Black triangles show the bottom mooring locations.

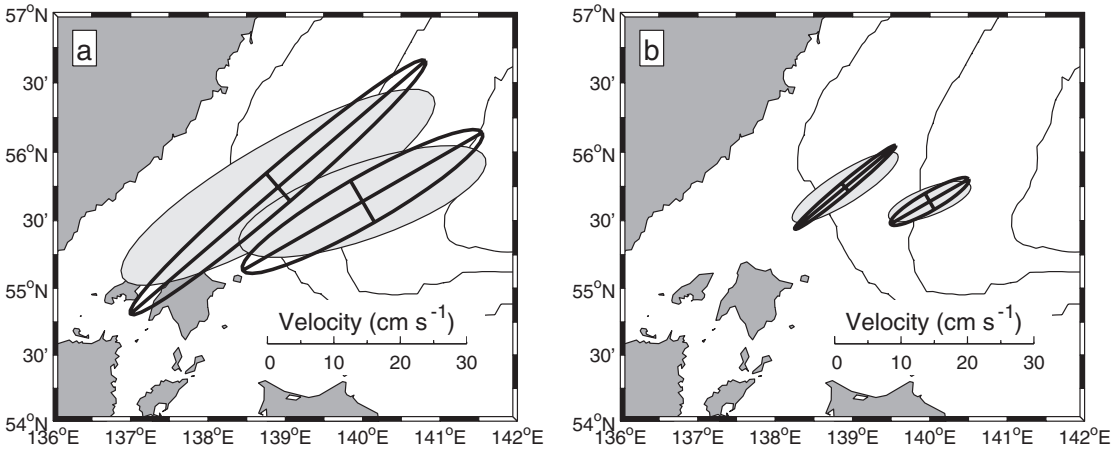

Fig. 3.2 Mean tidal ellipses of (a) M_2 and (b) S_2 constituents based on moored observations. Ellipses at the levels of 14 and 72 m above the bottom are shown by gray shading and black outlines, respectively. 100, 150, and 200 m isobaths are shown.

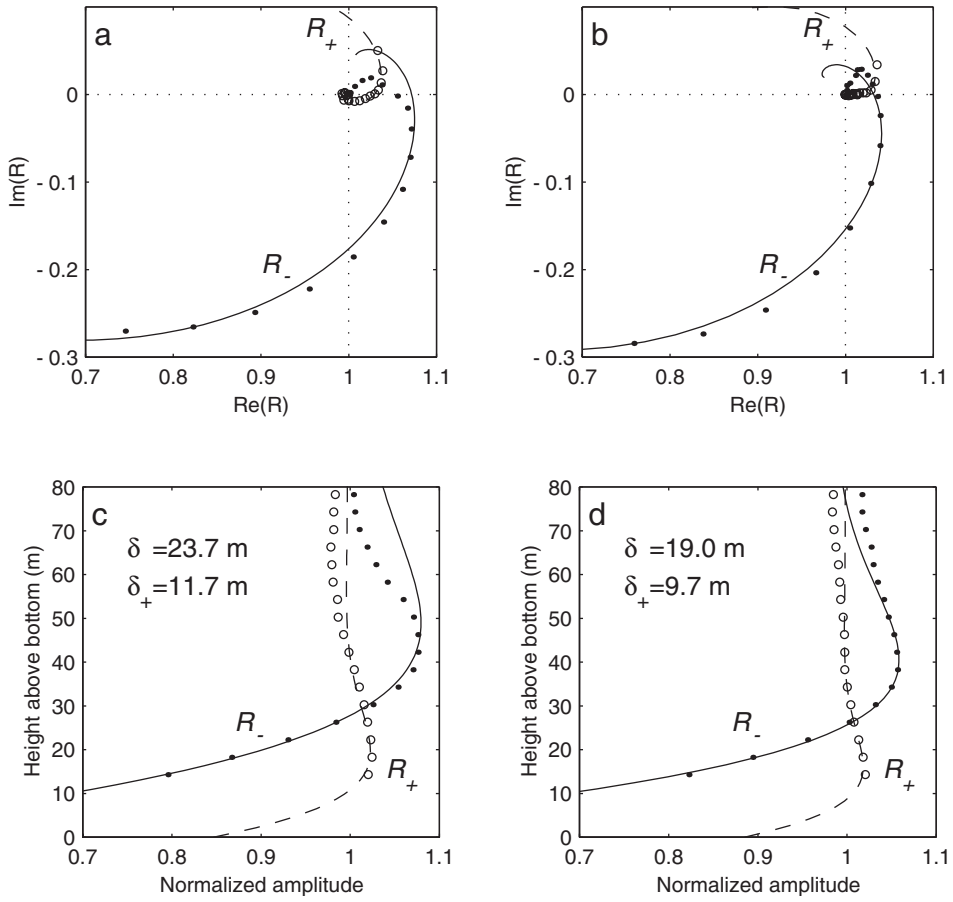

Fig. 3.3 Bottom tidal Ekman spirals observed at the inshore (a,c) and offshore (b,d) moorings. Panels (a) and (d) show hodographs of rotary M_2 components; panels (c) and (d) show vertical profiles of the absolute values of these components. Temporally-averaged clockwise (R_-, dots) and counterclockwise (R_+, open circles) components normalized by their vertical means are plotted. Dashed and solid lines are the theoretical curves, best-fit to the bottom half of each complex profile. Ekman layer depths, inferred from each fit, are shown in panels (c) and (d).

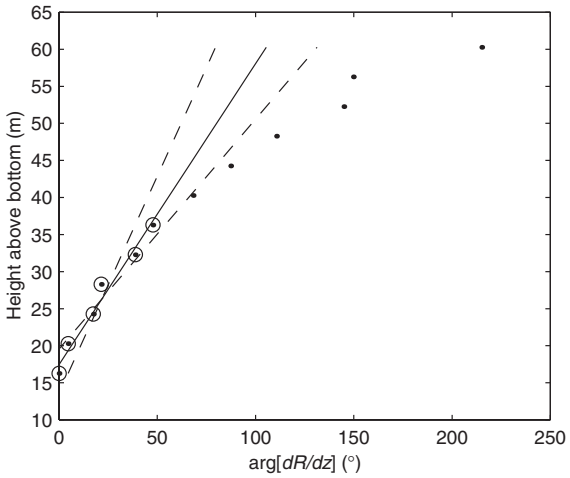

Fig. 3.4 Example of vertical profile of rotary shear phase (dots). The solid line shows a linear fit to the 6 bottommost points (circled). 90% confidence interval of the line slope is shown by dashed lines.

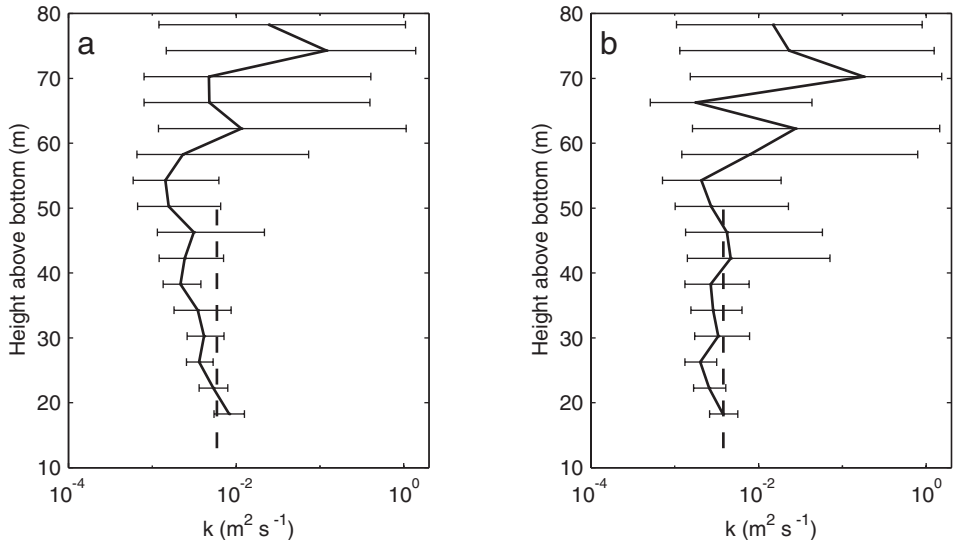

Fig. 3.5 Mean vertical profile of vertical eddy viscosity coefficient at (a) inshore and (b) offshore mooring. 90% confidence intervals are shown. Dashed lines show the values, determined by the least squares fit of the theoretical relationship (15) to the observed mean profiles of *R*. (shown in Fig. 1.12b-c).

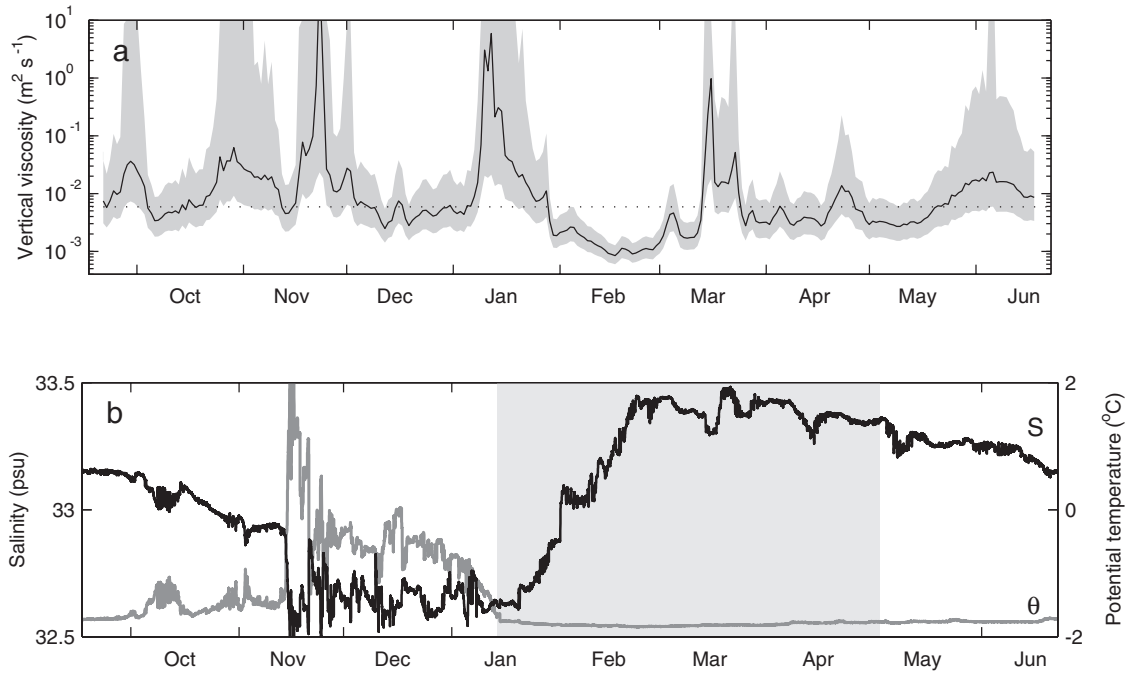

Fig. 3.6 (a) Near-bottom vertical eddy viscosity coefficient at the inshore mooring. Shading represents 90% confidence interval. The dashed line shows the eddy viscosity, determined by the least squares fit of the theoretical relationship (15) to the observed mean profiles of R- (shown in Fig. 1.12b-c). (b) Bottom salinity (black line) and potential temperature (gray line) at the same site. Shaded region indicates presence of surface ice, based on correlation of ADCP surface echo.

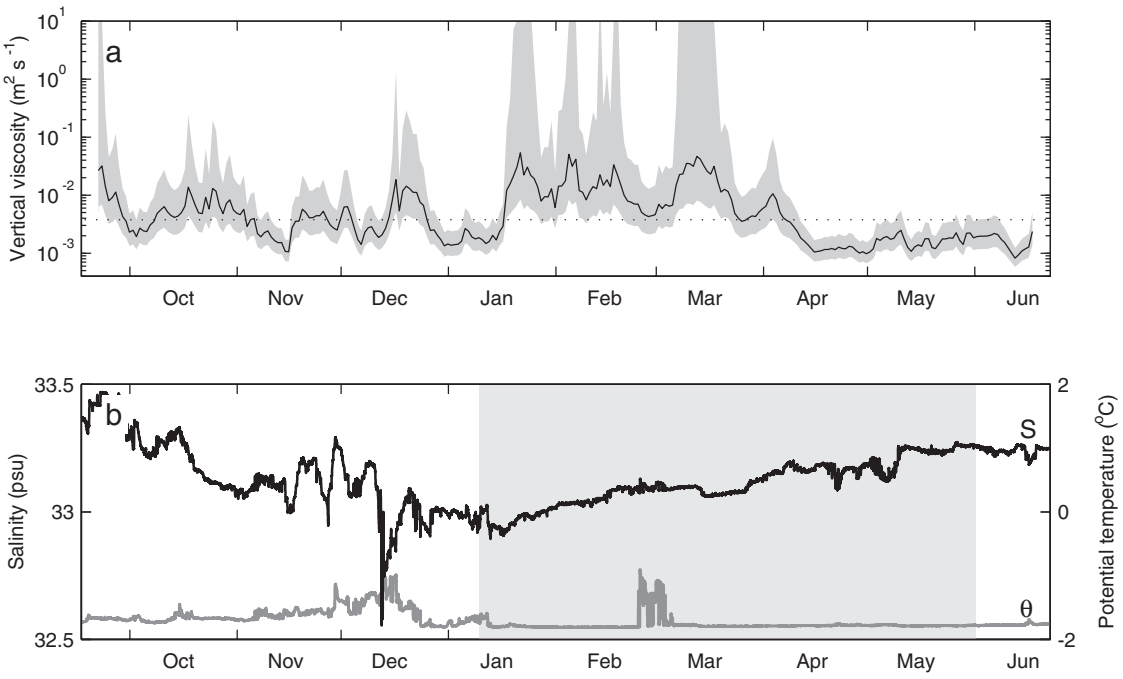

Fig. 3.7 Same as Fig. 3.6, but for the offshore mooring.

CHAPTER IV

Role of Tidal Mixing in the Dynamics of the Shelf Region

1 Introduction

In 1999-2000 the process of Dense Shelf Water (DSW) formation via brine rejection was directly observed on the northwestern shelf of the Okhotsk Sea using bottom moorings [*Shcherbina et al.*, 2003]. These observations suggested an important role for shelf dynamics in the formation, evolution, and export of DSW. In particular, the tidal mixing front was shown to be a key factor in the early stages of dense shelf water formation [*Shcherbina et al.*, 2004a]. Interpretation of the observations, however, was hampered by insufficient knowledge of the processes involved in the annual evolution of the shelf hydrographic structure.

This chapter presents the results of several process modeling studies, designed to elucidate some of the unresolved aspects of the observations. Section 2 summarizes the observed properties of the Okhotsk Sea shelf front. A simple one-dimensional analytical model of front formation is developed in section 3. Circulation in the cross-shelf plane is investigated with the help of a simplified two-dimensional numerical model in section 4. Section 5 extends the two-dimensional numerical model to include realistic tidal and wind parameterizations; evolution of the tidal mixing front in summer and fall is simulated in this section. Tidal mixing during the wintertime dense water formation stage is studied in section 6.

In particular, the following results are obtained:

1) The tidal mixing front structure can be reproduced with a primitive one-dimensional mixing model with prescribed dependence of vertically uniform diffusivity on water depth.
2) The observed offshore surface density maximum can be created solely by mixing and does not need to be associated with upwelling.
3) A combination of tidal and wind mixing results in a distribution of diffusivity that is favorable for the formation of the mixing front.
4) The front location progresses offshore both during early summer warming, and during fall cooling. The front position during most of the summer is stable.
5) Baroclinic instability of the wintertime density front leads to enhancement of internal wave activity in the polynya region. At the same time the increase in stratification that results from the instability leads to the reduction of vertical eddy diffusivity in that region.

2 Observations

2.1 CTD observations

The hydrographic structure of the northwestern shelf of the Okhotsk Sea was observed with two surveys performed in September 1999 and June 2000 [*Shcherbina et al.*, 2004a]. These two surveys documented both the early (June) and the late (September) stages of the development of the shelf front, even though these observations belong to two different cycles of summer front development.

The mixing front is evident in all property distributions, both in June and in September (Figs. 1 and 2). In June (Fig. 4.1a,c,e), the front is located more than 50 km closer to the shore than in September, which suggests substantial offshore movement of the front during the summer. On the September section (Fig. 4.1b,d,f) the front reaches the 100 m isobath and its structure becomes more pronounced. The front separates the warm, relatively fresh, well-mixed water inshore from the stratified offshore region with a well-defined surface mixed layer. This structure, known as a "Type II" tidal mixing front [*Hill and Simpson*, 1989], is commonly observed in shallow seas in summer. Horizontal variability of tidal mixing is a well-established mechanism for forming of fronts of this type [*Simpson and Hunter*, 1974; *Hill and Simpson*, 1989]. This mechanism is illustrated in sections 3-5 below.

A characteristic feature of the mixing front observed on the northwestern shelf of the Okhotsk Sea in September 2000 is the presence of a horizontal maximum of surface density and salinity and a corresponding temperature minimum (Fig. 4.1b,d,f). As will be shown in sections 3 and 5, this feature should accompany every "Type II" tidal mixing front. However, to our knowledge, this feature has not been singled out before, possibly because it may be easily occluded in the observed distributions of properties by the horizontal mixing and surface heating.

A horizontal surface maximum in nutrient concentration is also associated with the tidal mixing front in late summer (Fig. 4.2d,f), creating favorable conditions for a phytoplankton bloom. A clear increase of chlorophyll concentration in the frontal zone was observed on 22 September 1999 in the SeaWiFS satellite imagery (Fig. 4.3) (courtesy of SeaWiFS Project and the Goddard Earth Sciences Data and Information

Services Center/Distributed Active Archive Center). An increase of primary productivity is commonly found in the vicinity of tidal mixing fronts [*Pingree et al.*, 1975; *Demers et al.*, 1986]. These bloom conditions are typically explained by tidal front excursions or cross-frontal exchange bringing nutrients to the stratified side of the front, where the inhibited vertical mixing reduces the light limitation on the plankton growth [*Demers et al.*, 1986]. The maximum of nutrient concentration formed just inshore of the front, similar to that observed in the Sea of Okhotsk, may additionally facilitate the bloom.

Even though the horizontal density, salinity, and nutrient maxima observed in the frontal zone suggest active frontal upwelling, vertical advection is not necessary to produce the tidal mixing front observed on the Okhotsk Sea shelf. Bottom boundary layer convergence leading to frontal upwelling is a feature commonly associated with the shelfbreak fronts [*Houghton and Visbeck*, 1998; *Pickart*, 2000; *Chapman and Lentz*, 1994; *Chapman*, 2000a]. *Pickart* [2000] argued that the reduced isopycnal cross-shore gradients of potential temperature and salinity observed on the Middle Atlantic Bight shelf indicate such upwelling. However, similar analysis of the property distribution on the Okhotsk Sea shelf in September showed no conclusive evidence of such upwelling. As will be shown in section 4 below, the modeled tidal mixing front is actually associated with surface *downwelling*, and the circulation in the vertical plane has little effect on the formation of the horizontal density maximum at the surface.

2.2 AVHRR SST observations

Insight into the late autumn evolution of the shelf front can be gained from satellite sea surface temperature (SST) observations. Ocean Pathfinder Advanced Very High Resolution Radiometer (AVHRR) SST data were obtained from the NASA Physical Oceanography Distributed Active Archive Center at the Jet Propulsion Laboratory, California Institute of Technology. In summer infrared images, the front is poorly visible, likely due to a thin layer of warm water masking the subsurface structure. Starting in September this layer disappears due to the increasing surface heat loss, and the underlying mixed layer structure becomes evident in the SST images (Fig. 4.4).

The front position generally lies between the 100 and 150 m isobaths on the northern and northwestern shelves. Even though the locations of the front in September and November are close, the sign of the offshore temperature gradient changes. This transition can be clearly demonstrated by considering the changes of mean SST anomaly, referenced to the offshore SST (Fig. 4.5a). Until early October, inshore waters are colder than offshore; however, by 19 October the inshore SST anomaly becomes positive. The transition roughly coincides with the net surface heat flux becoming negative (Fig. 4.5b). It is remarkable that the change seems to only involve the regions shallower than 170 m. In both early-fall and late-fall regimes, the SST shows an offshore minimum, corresponding to the density maximum observed during the CTD survey. The position of the SST minimum shifted from the 120 m to the 170 m isobath between 29 September and 19 October.

Theories based on the energy balance of tidal mixing and heat input suggest that the location of the mixing front should follow a critical value of $\chi=\log_{10}(h/\langle u^3\rangle)$

[*Simpson and Hunter*, 1974], where h is the bottom depth, u is the depth-averaged tidal current amplitude, and angle brackets denote temporal averaging. Extensive research on the European shelf provided the observational support for this criterion and estimation of the critical value χ=2.7±0.4 [*Simpson and Hunter*, 1974; *Simpson and James*, 1986; *Bowers and Simpson*, 1987]. *Schumacher et al.* [1979] found that the location of the shelf front in the Bering Sea agrees well with a larger critical value of χ=3.5. (They attribute 0.4 of the discrepancy between this value and the European shelf result to the difference in definitions of χ.)

An alternative approach to estimating the location of a mixing shelf front is based on the relative thickness of the tidal frictional boundary layer [*Garrett et al.*, 1978; *Soulsby*, 1983; *Stigebrandt*, 1988]. This approach leads to a different critical value of h/u~80 s, successfully locating shelf fronts in the Irish Sea and Gulf of Maine [*Loder and Greenberg*, 1986; *Stigebrandt*, 1988].

The location of the mixing front on the northwestern shelf of the Okhotsk Sea does not agree with either the h/u^3 or h/u criteria (Fig. 4.6). The front is found within a wide range of these parameters ($\log_{10} h/u^3$ between 3.9 and 4.8, $\log_{10} h/u$ between 2.7 and 3), substantially exceeding the established critical values (2.7 and 1.9, respectively). The front is found in anomalously deep water for the comparatively low tidal amplitudes observed on the Okhotsk Sea shelf. Similar to the Bering Sea observations [*Schumacher et al.*, 1979], this discrepancy can be explained by reduced background stratification and lower values of the thermal expansion constant. As a result, thermal stabilization of water column under comparable surface heat flux may be reduced, increasing the penetration depth of the tidal boundary layer. Additionally,

wind mixing likely plays an important role, aiding the tides in homogenization of water column. The front location follows the contours of bottom Ekman boundary layer criterion (h/u) slightly better (Fig. 4.6). This suggests an important role for boundary layer dynamics in establishing the position of the front. The boundary layer properties will be further discussed in section 5.

3 Simple one-dimensional model

Insight into the origins of the mixing front can be gained by studying a simple one-dimensional analytical mixing model. In this model, the vertical diffusivity is taken to be depth-independent, but decreasing towards offshore with increasing water depth. Several characteristic features of the mixing front observed on the northwestern shelf of the Okhotsk Sea can be reproduced with this model, including the surface density maximum in the frontal zone.

The model description is first given in section 3.1. The model is then used to simulate the mixing front observed on the northwestern shelf of the Okhotsk Sea (section 3.2).

3.1 Formulation

In the one-dimensional model considered in this section, the temporal evolution of density anomaly ρ (or any other tracer) is governed by

$$\rho_t = A(x)\rho_{zz}, \tag{22}$$

where the vertical diffusivity $A(x)$ is constant in time and in the vertical, but may vary horizontally (offshore). Equation (22) is subject to the top and bottom no-flux

boundary conditions ρ_z=0 at z=0, -H and the initial condition ρ=$\rho_0(z)$ at t=0. The initial condition is chosen to be a step function

$$\rho_0 = \begin{cases} -\rho_S, \text{ for } z > -D \\ 0, \text{ for } -H < z < -D \end{cases}$$

with the discontinuity at z=-D, representing the springtime mixed layer with density anomaly $-\rho_s$ created by ice melt and surface warming.

The solution to (22) in an infinite domain can be expressed as

$$\rho(z,t) = \int_{-\infty}^{\infty} \rho_0(z-\zeta) G(\zeta) d\zeta \tag{23}$$

where $G(\zeta)=(4\pi At)^{-1/2}\exp(-\zeta^2(4At)^{-1})$ is the Green's function of (22). The no-flux boundary conditions at the surface and at the bottom can be satisfied using the method of images, expanding ρ_0 from [-H, 0] to [-∞, ∞] so that

$$\rho_0^{\infty} = \begin{cases} -\rho_S, \text{ if } |z-2mH| < D \\ 0, \text{ otherwise} \end{cases},$$

where m=0, 1,etc. It can be seen that ρ_0^{∞} is symmetric with respect to z=0 and z= -H, and consequently the convolution (23) satisfies no-flux boundary conditions ρ_{zz}=0 at z=0, -H. The expanded initial temperature distribution can also be expressed as a series

$$\rho_0^{\infty} = -\rho_s \left(\Pi(D,z) + \sum_{n=1}^{\infty} \left[\Pi(2nH+D,z) - \Pi(2nH-D,z) \right] \right),$$

where

$$\Pi(d,z) = \begin{cases} 1, \text{ if } |z| < d \\ 0 \text{ otherwise} \end{cases}.$$

Defining

$$E(d,z)=\int_{-\infty}^{\infty}\Pi(d,z-\zeta)G(\zeta)d\zeta=\int_{z-d}^{z+d}G(\zeta)d\zeta=\frac{1}{2}\left[erf\left(\frac{z+d}{2\sqrt{At}}\right)-erf\left(\frac{z-d}{2\sqrt{At}}\right)\right],$$

the solution is then given by

$$\rho(z)=-\rho_s\left(E(D,z)+\sum_{n=1}^{\infty}\left[E(2nH+D,z)-E(2nH-D,z)\right]\right).$$

The solution initially behaves as in the unbounded case: $\rho\sim-\rho_s E(D,z)$, until the terms within the sum sign become large and the solution reaches the steady state $\rho_\infty=-\rho_S D/H$ (Fig. 4.7). In the initial ("infinite") regime, the surface density depends on the depth of the mixed layer D and time. Later, in the "mixed" regime, the density is set by the ratio of the mixed layer depth and the total water depth H. The transition between the two regimes occurs at approximately $t=0.3t_0$, where $t_0=H^2A^{-1}$ is the natural time scale. At a given time, shallower regions are fully mixed, while the deeper remain in the "infinite" regime. The surface density in the mixed regime increases with the water depth, contrary to the surface density in the "infinite" regime, which decreases with H (Fig. 4.8). As a result, a surface density maximum is formed.

3.2 Okhotsk Sea one-dimensional simulation

The one-dimensional model described in the previous section will now be investigated in a setting modeled after the northwestern shelf of the Okhotsk Sea. A 200-km cross-shelf section (Fig. 4.9a), with the depth linearly increasing from 50 to 200 m, resembles that surveyed during September 1999 and June 2000 (Fig. 4.1). The model was initialized with a step-like density profile, with a 25-meter mixed layer with a density anomaly of -6 kg m^{-3}.

Vertical diffusivity A was chosen to decrease exponentially with increasing depth (Fig. 4.9b). The choice of an exponential relationship is mostly empirical. Exponential increase in tidal amplitude towards the shore (see section 5.1) provides some support for this choice. Since the purpose of the one-dimensional model is to illustrate the emergence of the mixing front structure, such a simplified relationship between vertical diffusivity and water depth is reasonable. The e-folding scale of the decay and the value of the offshore diffusivity were selected so that the surface density distribution after a 90-day model run resembled that observed during September 1999 (Fig. 4.10).

The 3-month running time was chosen to represent summertime mixing. The satellite data (not shown) indicate that the ice cover on the northwestern shelf disappeared by 20 June 1999, approximately 90 days before the September 1999 survey.

After 90 days of mixing, a vertical density anomaly structure similar to that observed in autumn on the northwestern shelf of the Okhotsk Sea emerges (Fig. 4.11a). The "front" separating the "mixed" regime inshore and the "infinite" regime offshore is located approximately 80 km offshore in 100 m of water. The horizontal density maximum, which is the surface manifestation of this front, disappears approximately 60 m below the surface. Along the bottom, the front is seen only as a transition between the gradual density decrease inshore and the region of higher density gradient offshore.

The surface density maximum gradually moves offshore as the mixing progresses (Fig. 4.12), since there is no process to halt the progression in this very simple model.

The speed of the offshore progression of the maximum varied from 3 km day^{-1} at the beginning to 0.15 km day^{-1} at the end of the model run. The speed is pre-determined by the choice of relationship between the depth and viscosity. However, since the chosen configuration produced a realistic density distribution in a reasonably chosen amount of time, 0.15 km day^{-1} might be a reasonable estimate for the speed of the offshore propagation of the surface density maximum in autumn. As will be shown in section 5.4, this offshore transition may be arrested by changes in the vertical mixing distribution.

The bottom-referenced geostrophic flow corresponding to the modeled density distribution is shown in Fig. 4.11b. The main feature is a mid-depth jet located slightly offshore of the surface density maximum location. If the model domain is interpreted as a section across the northern shelf of the Okhotsk Sea (North on the left), the flow direction is westward. In the mixed regime inshore of the front, the westward flow is surface-intensified, and also increases toward the shore.

Cross-shore variation of the alongshore flow is expected to lead to areas of convergence in the bottom boundary layer, and in turn to secondary circulation in the section plane. Bottom boundary layer dynamics cannot be studied with this geostrophic model. Consequently, the secondary circulation is investigated in the next section using a primitive equation numerical model.

4 Cross-shelf circulation – two-dimensional model

Secondary cross-shelf circulation induced by friction associated with the main frontal jet often plays an important role not only in property distribution in the frontal zone, but in controlling the front itself. Convergence of the bottom boundary layer

leading to the frontal upwelling has been shown to be associated with shelf fronts in analytical [*Gawarkiewicz and Chapman*, 1992; *Chapman and Lentz*, 1994] and observational studies [*Pickart*, 2000]. To conduct such a two-dimensional study, the model has to be upgraded, while still retaining a great degree of idealization. A primitive-equation numerical model with a nearly two-dimensional setup is described in section 4.1. Results of the model run and comparison with the one-dimensional model are given in section 4.2.

4.1 Formulation

The two-dimensional study of cross-shelf circulation was conducted using the Regional Oceanic Modeling System (ROMS). ROMS is a free-surface terrain-following primitive-equation ocean circulation model [*Shchepetkin and McWilliams*, 2004], initially based on the S-coordinate Rutgers University Model (SCRUM) described by *Song and Haidvogel [1994]*. ROMS is particularly suitable for this study due to its modular design, which allows construction of models with different degrees of physical complexity.

The model domain is a short periodic channel 200 km wide and 10 km long, with depth increasing linearly across the channel from 50 to 200 m. The cross-section of the channel is identical to that used with the one-dimensional model above. The model consists of 100 grid points along the cross-shore ("long") dimension, 6 grid points along the "short" periodic dimension, and 40 vertical layers distributed uniformly throughout the depth. The inshore (shallow) side of the channel is bounded by a free-slip wall; a radiation condition is enforced at the open offshore boundary. Similarly to

the one-dimensional model above, vertically uniform eddy diffusivity is prescribed as a function of bottom depth. To facilitate the comparison with the analytical model described in the previous section, the same exponential relationship between the diffusivity and depth is used (Fig. 4.9b). Also, a constant eddy viscosity $\kappa_u=1\times10^{-2}$ m^2 s^{-1} is assumed, using a typical value for this region (see Chapter III). Bottom friction is parameterized using a linear bottom drag coefficient $r=1\times10^{-3}$ m s^{-1}. The Coriolis parameter is $f_0=1.2\times10^{-4}$ s^{-1}, corresponding to that at approximately 56ºN. It should be noted that the combination of constant viscosity and variable diffusivity used in present model setup is physically implausible. However, it is used deliberately to simplify the flow structure and focus on buoyancy-driven currents. A realistic viscosity distribution is introduced into the model in section 5.

4.2 Simulation of cross-shelf circulation

The model was initialized with the same density distribution as for the analytical model (Fig. 4.9a), consisting of a 25-meter mixed layer with the 6 kg m^{-3} density anomaly. After 90 days of mixing, the two-dimensional numerical model produces essentially the same density distribution as the analytical model (Fig. 4.13a, cf. Fig. 4.11a). The along-shelf flow structure (Fig. 4.13b) is similar to the geostrophic flow pattern (Fig. 4.11b); however, the flow is reversed in the bottom boundary layer due to the model's tendency for barotropic momentum conservation.

Secondary circulation in the cross-shelf plane can be roughly described as three overturn cells. The inshore mixed region cell consists of onshore flow in the bottom boundary layer, intense upwelling at the coast, and weak downwelling throughout the

region out to the front. Flow in the stratified region offshore of the front consists of two counter-rotating cells. The combination of the three cells creates a zone of strong downwelling at the border between the mixed and stratified regimes, which coincides with the location of the surface density maximum. At the same time, weak upwelling is observed in the deeper layers in this region. These two flows converge at about 75 m depth and feed the offshore flow along the base of the thermocline.

5 Simulation of tidal mixing on the shelf

In the previous section it was shown that idealized, non-uniform mixing is capable of producing a realistic distribution of density anomaly on the shelf. Here a combination of more realistic tidal and wind mixing are shown to produce a similar distribution of vertical diffusivity and create the front. The basic model setup is equivalent to that used in the previous section. However, instead of prescribing eddy viscosity and diffusivity, they are parameterized using the "k-ε" turbulence closure scheme [*Jones and Launder*, 1972]. A brief overview of this closure and the reasoning behind the choice of this particular scheme is described in section 5.3. Realistic tidal (section 5.1) and wind (section 5.2) forcings provide the source of turbulence. Model predictions of the summer and fall evolution of the mixing front are compared with both the one-dimensional model and the observations, in sections 5.4 and 5.5.

5.1 Tidal forcing

Regional Oceanic Modeling System (ROMS) was used to simulate the effects of tidal mixing on the shelf density distribution. Similarly to section 4.1, a nearly two-dimensional model configuration is used. The model domain is a short periodic

channel 200 km wide and 10 km long, with depth increasing linearly across the channel from 50 to 200 m. The cross-section of the channel is identical to that used with the one-dimensional model above. The model consists of 100 grid points along the cross-shore ("long") dimension, 6 grid points along the "short" periodic dimension, and 40 vertical layers distributed uniformly throughout the depth. The inshore (shallow) side of the channel is bounded by a free-slip wall.

The model is forced with barotropic tidal flow and free surface variations at the open northern and southern boundaries through the Flather/Chapman boundary conditions [*Flather*, 1976; *Chapman*, 1985]. This tidal forcing has to be consistent with the periodic boundary conditions and must also be dynamically self-consistent. A separate simple barotropic tidal model was used to produce such forcing. The tidal model solves the shallow water Laplace tidal equations

$$\begin{aligned} u_t - fv &= -g\eta_x \\ v_t + fu &= -g\eta_y \\ \eta_t + (hu)_x + (hv)_y &= 0, \end{aligned} \tag{24}$$

where u and v are the horizontal velocities, η is the surface elevation, h is the water depth, g=9.8 m s^{-2}, f=1.2×10^{-4} s^{-1} is the Coriolis frequency, and subscripts denote temporal and spatial derivatives. A plane wave solution with the wave number perpendicular to the shore has no alongshore variability, and consequently would satisfy the periodic boundary conditions. The system (24) was solved numerically for such a plane wave at M_2 tidal frequency (corresponding to 12.42 h period). Tidal velocities and elevations at the inshore and offshore boundaries were then used to provide forcing at the boundaries of the numerical model.

It should be noted that such a cross-shore plane tidal wave is unrealistic. In coastal regions, tides generally have the form of a Kelvin wave propagating along the coast [*Miles*, 1972]. The alongshore wavelength of such a Kelvin wave is large (on the order of 1000 km), but finite. Given the relatively small alongshore extent of the model domain (10 km), a Kelvin wave solution would be inconsistent with the imposed periodic boundary conditions. The increase of tidal amplitude towards the shore, which is the main focus of this simulation, is similar for both the Kelvin wave and the plane wave solution (Fig. 4.14). Consequently, the plane wave solution can be considered an acceptable forcing for the present model. The Kelvin wave solution was used to force the three-dimensional model of wintertime shelf evolution, described in section 6.

5.2 Wind mixing

Surface wind mixing was included in the model, as the tidal mixing alone cannot overcome the strong stratification at the initial mixed layer base. In order to avoid undesirable wind-driven circulation, random windstress with zero mean was imposed. The standard deviation of wind stress was set to 0.07 N m^{-2}, matching the wind stress statistics extracted from 4-times daily ECMWF reanalysis for the survey location on the northwestern shelf of the Okhotsk Sea (Fig. 4.15). The ECMWF wind stress has a decorrelation time scale of about 2 days (not shown). The modeled wind stress variability, however, is decorrelated in time, so the wind mixing may be somewhat underestimated compared to reality. Since the wind mixing is ancillary to the main

focus of the present simulation, no further attempt to reproduce it realistically was made.

5.3 Choice of mixing scheme

ROMS offers a wide variety of vertical eddy diffusivity parameterizations. In particular, a range of second-order turbulence closures is available. These closures involve solving additional prognostic equations for second-order turbulence statistics (such as turbulence kinetic energy), which allow simulation of turbulence production, dissipation, and advection. Using these closures allows realistic modeling of the behavior of subgrid turbulent mixing in response to changes of local flow properties such as stratification and shear. Despite their conceptual similarity, second-order closures differ vastly in formulation of the particular turbulence evolution sub-models, which affects the diffusivity predictions for various flows.

The so-called "k-ε" closure, using the Generalized Length Scale (GLS) method [*Warner et al.*, 2004], was chosen for the present study. Similarly to the widely used Mellor-Yamada 2.5 level closure (MY2.5), k-ε closure involves solving two additional equations for turbulent kinetic energy k and a secondary mixing parameter. In MY2.5 closure, the secondary parameter is a product of turbulent kinetic energy k and mixing length l (hence the alternative designation "*k-kl*" for this type of closure in GLS terminology). Behavior of MY2.5 closure is strongly dependent on the choice of the wall proximity function, which has to be based on the particular flow regime. Several distinctly different formulations have been proposed [*Mellor and Yamada*, 1982; *Burchard and Baumert*, 1998; *Burchard*, 2001; *Blumberg et al.*, 1992], but the correct

choice is not obvious for our model setup. MY2.5 model is also known for underestimating wind-induced, near-surface mixing [*Burchard and Bolding*, 2001; *Warner et al.*, 2004]. In the *k*-ε model, originally developed by *Jones and Launder* [1972], the secondary parameter is the turbulent kinetic energy dissipation rate ε, and the wall function is not required. It has been shown that *k*-ε mixing parameterization performs better than generic MY2.5 in both wind and tidal mixing experiments [*Warner et al.*, 2004; *Burchard and Bolding*, 2001]. Additionally, this parameterization produces reasonable results for the case of unstable convective flows [*Burchard and Baumert*, 1998]. The present model formulation uses the "Canuto-A" stability function formulation [*Canuto et al.*, 2001], which has been shown to improve agreement with observations, in addition to being physically and numerically robust [*Burchard and Bolding*, 2001].

5.4 Simulation of summertime front evolution

Formation of the mixing front on the shelf in summer was simulated by a combination of surface buoyancy gain with wind and tidal mixing. This represents a more realistic scenario of gradual establishment of the surface mixed layer, compared to the step-function initialization used in the one-dimensional model. The present model is initialized with weak linear stratification (N=4x10^{-3} s^{-1}), similar to that found in the Okhotsk Sea main thermocline. Constant buoyancy flux at a rate of 1×10^{-7} m^2 s^{-3} is then imposed throughout the 90-day "summer" run of the model. For reference, such buoyancy flux is equivalent to approximately 200 W m^{-2} heating at 15˚C and 33 psu.

(Based on ECMWF reanalysis data, mean heat flux on the northwestern shelf of the Okhotsk Sea in June 1999 was 210 W m^{-2}, dropping to 103 W m^{-2} by August.)

After 90 days of combined mixing and buoyancy gain, a frontal structure is created similar to that observed on the northwestern shelf of the Okhotsk Sea (Fig. 4.16). Similarly to the one-dimensional model result, mixed and stratified regions occur, separated by a surface density maximum. The vertical density distribution, however, is markedly different, as the tidal mixing model produces a well-mixed bottom boundary layer. This boundary layer resembles the observations (Fig. 4.1), but is considerably thicker.

The distribution of vertical eddy diffusivity is markedly different in the mixed and stratified regions (Fig. 4.18a). Inshore of the front, the lack of stratification that suppresses turbulence leads to the enhancement of mixing. On the other hand, in the stratified region, diffusivity is lower, and only moderately enhanced within the surface and bottom boundary layers. At the front between the two regions, the mixing is further suppressed by the strong density gradients, leading to reduction of the bottom boundary layer depth. Vertically averaged (Fig. 4.18b), however, the diffusivity decreases exponentially offshore (disregarding the perturbation in the frontal region), following the reduction in tidal amplitudes. This result supports the ad hoc choice of an exponential relationship between diffusivity and depth in the one-dimensional model in sections 3 and 4. The rate of this exponential decay is substantially lower in the tidal mixing model, reflecting the differences in vertical structure of mixing.

The front is formed by merging of the surface and bottom boundary layers. This location is established by a dynamical balance of mixing and stratification. Offshore

propagation of the front is precluded by the region of reduced diffusivity that supports the high stratification in that region, impeding, in turn, further growth of the bottom boundary layer.

Compared to the one-dimensional model, the surface density maximum is found closer to the shore in the tidal mixing model. It can be seen (Fig. 4.17) that initially the maximum starts moving offshore, just as in the one-dimensional case, but its offshore propagation is quickly arrested around the 90-meter isobath. This behavior can be explained by the feedback between the density structure and mixing.

5.5 Simulation of autumn front evolution

The mixing front formation mechanism explored in the previous section relies on positive surface buoyancy flux. With the reversal of the sign of buoyancy flux in autumn, the front is expected to break down. To simulate this process, the model was run "in reverse", with the initial condition taken from the end of the "summer" simulation and a uniform buoyancy loss of 1.6×10^{-7} m^2 s^{-3} imposed. For reference, such buoyancy loss is equivalent to approximately 300 W m^{-2} heat loss at 15°C. The "fall" run was conducted for 30 model days.

During the "fall" model run, the shallower regions experience faster cooling. As a result, the horizontal density gradient created inshore of the front during the "summer" run is first removed, and later reversed (Fig. 4.19a). The density anomaly of the shallow mixed layer in the stratified region decreases rapidly. This leads to a decrease of the thermocline sharpness and deeper penetration of the wind mixing. Consequently, surface and bottom boundary layers can meet further offshore, and the

position of the front shifts (comparing Figs. 15 and 18). This offshore shift was also observed in the Okhotsk Sea bottom mooring records [*Shcherbina et al.*, 2004a].

Even though the horizontal density gradients in the bottom layer decrease, the location of the front is still clearly seen on the vertical diffusivity section (Fig. 4.19b). Compared to the late stages of the summer run (Fig. 4.18a), bottom boundary layer is thicker, which allows it to surface at a new, deeper location. The front position continues to be marked by the patch of reduced diffusivity offshore.

6 Wintertime dense water formation

In winter, the shelf dynamics are primarily driven by intense localized buoyancy loss, associated with brine rejection in the coastal polynya [*Shcherbina et al.*, 2004a]. As a result, a mass of dense water is formed near the coast. According to theoretical predictions [*Gawarkiewicz and Chapman*, 1995], the density front formed along the offshore edge of the polynya is baroclinically unstable. This instability leads to its breakup into a series of baroclinic eddies that play a crucial role in exporting the density anomaly from the forcing region.

In this section, the changes of vertical mixing associated with the instability of the polynya front are investigated. This study directly follows the numerical and analytical model of shallow polynya development under various conditions, developed by *Gawarkiewicz and Chapman* [1995], *Chapman and Gawarkiewicz* [1997], *Chapman* [1999], and *Chapman* [2000b; *Chapman and Gawarkiewicz*, 1997; *Chapman*, 1999; *Chapman*, 2000b]. The present work extends these studies to include the interaction of tides with the developing instability, as follows:

1) Density increase at a station within the polynya can terminate under continuing buoyancy loss. Even though *Gawarkiewicz and Chapman* [1995] and subsequent works imply this, these studies were mostly targeted on the integral properties of a polynya. However, to aid the interpretation of results of mooring observations [*Shcherbina et al.*, 2004a], evolution of the water properties at a specific location needs to be discussed.

2) Baroclinic eddies formed by the unstable density front at the edge of a polynya create favorable conditions for internal tide generation. The intensification of internal tides was shown to accompany the termination of linear density growth at a mooring within a polynya [*Shcherbina et al.*, 2004a]. If the link between eddies and internal tides is established in the model, these observations would provide the first indirect verification of the theoretical models of shallow polynya development.

3) Baroclinic instability in the polynya region decreases vertical eddy viscosity and diffusivity. Since polynyas are considered to be well-mixed by the brine-driven convection, high turbulent mixing within a polynya may be expected. The results of bottom boundary layer observations within a polynya on the northwestern shelf of the Okhotsk Sea, however, suggest a decrease of vertical eddy viscosity associated with dense shelf water formation (see chapter IV). This paradox can be explained by the influence of baroclinic eddies created by the instability at the polynya edge.

Section 6.1 describes the configuration of the numerical model used in the present study. The development of instability and the effects associated with it are then described in sections 6.2 and 6.3.

6.1 Model setup

The Regional Oceanic Modeling System (ROMS) described in section 5 is used for numerical simulation of wintertime dense water formation due to localized buoyancy loss in a coastal polynya. The model setup is similar to that used by Gawarkiewicz and Chapman [1995]. A full three-dimensional primitive-equation numerical model is set up in a 400 by 250 km domain (Fig. 4.20a). To aid the description, the long side of the domain is considered to be oriented zonally. The particular orientation, however, does not affect the results. The depth increases linearly from 50 m at the southern edge to 250 m at the northern one (Fig. 4.20b). A no-flow free-slip boundary condition is imposed on the southern boundary, to represent the shoreline. The model is initialized with weak linear stratification (N=4x10^{-3} s^{-1}), similar to that found in the Okhotsk Sea main thermocline.

Tidal forcing is imposed on the remaining open boundaries through the modulation of barotropic flow and free surface elevation. Self-consistent forcing is ensured by solving a separate system of barotropic tidal equations, as described in section 5.1. A Kelvin-wave type solution with cross-shore flow vanishing at the coast was chosen (Fig. 4.14).

Brine rejection in a coastal polynya is represented by the negative buoyancy flux B_0=-2×10^{-7} m^2 s^{-3} within the 200 by 50 km semi-elliptical area adjacent to the shore

(Fig. 4.20a). This "polynya" region is surrounded by a 10-km wide transition zone, where the buoyancy loss decays linearly from B_0 towards zero at its outer edge. For reference, mean buoyancy loss in the northwestern polynya during the 1999-2000 winter was on the order of 1 - 1.5×10^{-7} m^2 s^{-3} (Fig. 4.21), reaching 3×10^{-7} m^2 s^{-3} in the center of the polynya during the peak. In the simulation, the buoyancy loss starts on day 5 and continues through the end of the model run.

6.2 Instability

As previously shown by *Gawarkiewicz and Chapman* [1995], the offshore boundary of the newly-formed dense water quickly becomes unstable and breaks into baroclinic eddies that efficiently export the density anomaly offshore (Fig. 4.22, Fig. 4.23). The first eddies appear approximately 20 days after the onset of the buoyancy loss, and by day 40 they fill virtually the whole polynya area.

Density anomaly evolution at a virtual mooring within the polynya has two distinct phases (Fig. 4.24). During the first phase, the density increases nearly linearly, and the water column is well mixed. Arrival of the baroclinic eddies at day 35 marks the beginning of the second phase. At this point the density stops growing, and for the rest of the run it oscillates about the value reached during the first stage. At the same time, the water column becomes sharply stratified.

Changes in stratification have a pronounced effect on vertical eddy diffusivity (Fig. 4.25). During the linear density increase phase (days 5 to 35) the diffusivity stays nearly constant (with the exception of tidal fluctuations). During this stage the diffusivity is elevated by about a factor of 2 compared to its value prior to the

buoyancy loss onset on day 5. This difference is due to the response of the turbulence closure sub-model to the unstable stratification during the convective stage. In the beginning of the second phase, the diffusivity coefficient drops abruptly by more than three orders of magnitude in response to the sharp stratification brought by the baroclinic eddies. As the baroclinic instability involves the widening region on either side of the polynya boundary, a patch of suppressed mixing, clearly seen on the cross-shelf section of eddy diffusivity (Fig. 4.26b), grows as well.

The drop in eddy diffusivity associated with the arrival of the baroclinic eddies is preceded by a slight increase of mixing intensity at day 30 (Fig. 4.25). This increase is associated with a narrow patch of enhanced diffusivity just inshore of the unstable region. Similar mixing enhancement can also be observed inshore of the low-mixing region associated with summer mixing front (Fig. 4.19b). The cause of this increase is presently unknown. It can potentially be caused by downwelling observed in the edge of the mixing front (see section 4.2). It could also possibly be a modeling artifact. It should be noted, however, that a similar increase in eddy viscosity preceding its drop has been observed at the bottom mooring data (see Chapter III).

6.3 Internal waves

Increased stratification associated with baroclinic instability at the edge of the buoyancy forcing region also gives rise to strong internal tide generation. Several incidents of enhanced shear appear at the virtual mooring as soon as the baroclinic instability reaches the location of the mooring (Fig. 4.27). Close inspection of the

model results shows that the internal tide is generated in the bottom boundary layer and propagates upward.

Similar enhancement of the internal tide has been observed at one of the bottom moorings on the Okhotsk Sea shelf [*Shcherbina et al.*, 2004a]. Several bursts of internal tide activity followed the termination of linear density increase observed at that mooring. Striking similarity of the observed events with the present simulation allows us to conclude that the model adequately describes the basic processes involved in the wintertime evolution of the newly formed dense shelf water.

7 Conclusions

Density structure observed on the northwestern shelf of the Okhotsk Sea in September 1999 and in June 2000 is consistent with a "Type II" tidal mixing front. A front of this type is the boundary between a well-mixed band inshore and stratified region offshore. Early in the season (June) the front was found in relatively shallow water (<75 m deep). By early fall (September – October) the front moved offshore and was situated between 100 and 150 m isobaths.

The present work shows that the observed structure and evolution of the frontal zone can be adequately explained using a simple one-dimensional mixing model with vertically uniform diffusivity. Offshore exponential decrease of vertical eddy diffusivity from 3×10^{-2} m^2 s^{-1} at 50 m isobath to 3×10^{-6} m^2 s^{-1} at 200 m reproduces a mixing front structure similar to the one observed on the Okhotsk Sea shelf. The ad-hoc choice of exponential relationship between diffusivity and bottom depth is supported by the observed horizontal distribution of surface density. Additional justification is provided by the results of a numerical simulation of eddy diffusivity

evolution, which included the effects stratification and realistic tidal and wind forcing. In the one-dimensional mixing model with prescribed diffusivity, the front location progresses steadily offshore and reaches 120 m isobath after 90 days of mixing. In contrast, the front position on the northwestern shelf of the Okhotsk Sea in late summer appeared to be stable, even though offshore front movement may have occurred in early spring and late fall.

As illustrated by a tidally-driven two-dimensional model, the offshore propagation of the mixing front can be arrested at the depth where tidal bottom boundary layer can no longer reach the surface wind-driven boundary layer. The gap between the two boundary layers is characterized by relatively low eddy diffusivity that prevents further offshore extension of the near-shore mixed region. With realistic stratification, tidal and wind mixing, the front position is stabilized at the 90-100 m isobath. This depth range is close to the location of the tidal mixing front observed on the northwestern shelf of the Okhotsk Sea in September 1999. The model predicts a change of the sign of near-shore density anomaly and an additional offshore shift of the front in response to fall surface cooling. This prediction is consistent with the behavior of the front observed in September – October 1999. The results of modeling support the leading role for the tidal bottom boundary layer dynamics in formation and control of the mixing front on the Okhotsk Sea shelf.

During the September 1999 survey, the transition between the well-mixed and stratified regimes was marked by a lateral density maximum at the surface. The density maximum corresponded to a temperature minimum, as well as the maxima of salinity and nutrient concentration. In both the analytical and numerical models, the lateral

extrema in the property distributions occurs solely due to the cross-shore variability of mixing efficiency combined with increasing depth. The model predicts surface convergence and a weak near-surface downwelling in the frontal zone. Consequently, the observed density maximum may be of purely mixing origin, as the circulation in the vertical plane cannot be bring denser water to the surface.

Wintertime conditions on the northwestern shelf are characterized by localized buoyancy loss inside the coastal polynya. Mooring observations in 1999 - 2000 showed a linear density increase of the bottom density continuing for over a month. The density increase terminated abruptly several weeks prior to the closure of the polynya [*Shcherbina et al.*, 2004a]. A primitive-equation numerical simulation of an idealized coastal polynya reproduces this behavior of density at the outer edge of the polynya. The termination of density increase in the model is a result of baroclinic instability of the density front surrounding the polynya. Both the observations and the model show the intensification of the internal tide coinciding with the termination of density increase. The model confirms that this intensification is due to regions of strong stratification created by the baroclinic eddies, which, in turn, are a result of instability at the polynya edge. Enhancement of the internal tides leads to higher shear turbulence production. Despite that, the vertical eddy diffusivity in the region impacted by the baroclinic instability is reduced due to the overpowering effect of turbulence suppression by the increased stratification.

The range of analytical and numerical models described in the present study was designed to aid the interpretation of the observations and to elucidate the physical processes relevant to the dynamics of dense shelf water formation. These models show

that tidal mixing plays an important role at all stages of the seasonal cycle in the shelf region. Consequently, inclusion of tidal effects in large- and basin-scale models should be considered crucial for accurate simulation of the downward branch of thermohaline circulation driven in part by dense water formation in shelf seas.

Acknowledgements:

I am indebted to L. Talley and D. Rudnick for providing the Okhotsk Sea mooring data and continual support. I am also grateful to D. Haidvogel, H. Arango, and E. Di Lorenzo for instruction on the usage of ROMS. This paper benefited from stimulating discussions with C. Winant, D. Stammer, and D. Checkley. ECMWF ERA-40 data used in this study have been obtained from the ECMWF data server. SeaWiFS data were provided by SeaWiFS Project (Code 970.2) and the Goddard Earth Sciences Data and Information Services Center/Distributed Active Archive Center (Code 902) at the Goddard Space Flight Center, Greenbelt, MD 20771.

References:

Blumberg, A. F., B. Galperin, and D. J. O'Connor. Modeling vertical structure of open-channel flows, *J. Hydraulic Engineering*, 118(H8), 1119-1134, 1992.

Bowers, D. G. and J. H. Simpson. Mean position of tidal fronts in European-shelf seas, *Continental Shelf Res.*, 7(1), 35-44, 1987.

Burchard, H. On the q^2l equation by Mellor and Yamada (1982). *J. Phys. Oceanogr.*, 31, 1377-1387, 2001.

Burchard, H. and H. Baumert. The formation of estuarine turbidity maxima due to density effects in the salt wedge. A hydrodynamic process study., *J. Phys. Oceanogr.*, 28, 309-321, 1998.

Burchard, H. and K. Bolding. Comparative analysis of four second-moment turbulence closure models for the oceanic mixed layer, *J. Phys. Oceanogr.*, 31, 1943-1968, 2001.

Canuto, V. M., A. Howard, Y. Cheng, and M. S. Dubovikov. Ocean turbulence. Part I: One-point closure model - momentum and heat vertical diffusivities, *J. Phys. Oceanogr.*, 31, 1413-1426, 2001.

Chapman, D. Dense water formation beneath a time-dependent coastal polynya, *J. Phys. Oceanogr.*, 29, 807-820, 1999.

Chapman, D. Boundary layer control of buoyant coastal currents and the establishment of a shelfbreak front, *J. Phys. Oceanogr*, 30, 2941-2955, 2000a.

Chapman, D. The influence of an alongshelf current on the formation and offshore transport of dense water from a coastal polynya, *J. Geophys. Res.*, 105, 24007-24019, 2000b.

Chapman, D. and G. Gawarkiewicz. Shallow convection and buoyancy equilibration in an idealized coastal polynya, *J. Phys. Oceanogr.*, 27, 555-566, 1997.

Chapman, D. C. Numerical treatment of cross-shelf open boundaries in a barotropic coastal ocean model, *J. Phys. Oceanogr.*, 15, 1060-1075, 1985.

Chapman, D. C. and S. J. Lentz. Trapping of a coastal density front by the bottom boundary layer, *J. Phys. Oceanogr.*, 24(7), 1464-1479, 1994.

Demers, S., L. Legendre, and J.-C. Therriault, Phytoplankton response to vertical tidal mixing, in *Tidal Mixing and Plankton Dynamics, Lecture Notes on Coastal and Estuarine Studies*, vol. 17, edited by M. Bowman, C. Yentsch, and W. Peterson, pp. 1-40, Springer-Verlag, Berlin, 1986.

Flather, R. A. A tidal model of the Northeast Pacific, *Atmos.-Ocean*, 25, 22-45, 1976.

Garrett, C. J. R., J. R. Keeley, and D. A. Greenberg. Tidal mixing versus thermal stratification in the Bay of Fundy, Maine, *Atmos. Ocean*, 16, 403-443, 1978.

Gawarkiewicz, G. and D. Chapman. The role of stratification in the formation and maintenance of shelf-break fronts, *J. Phys. Oceanogr.*, 22, 753-772, 1992.

Gawarkiewicz, G. and D. Chapman. A numerical study of dense water formation and transport on a shallow, sloping continental shelf, *J. Geophys. Res.*, 100, 4489-4507, 1995.

Hill, A. E. and J. H. Simpson. On the interaction of thermal and haline fronts: the Islay front revisited, *Estuarine Coast. Shelf Sci.*, 28, 495-505, 1989.

Houghton, R. W. and M. Visbeck. Upwelling and convergence in the Middle Atlantic Bight shelfbreak front, *Geophys. Res. Lett.*, 25(15), 2765-2768, 1998.

Jones, W. P. and B. E. Launder. The prediction of laminarization with a two-equation model of turbulence, *Int. J. Heat Mass Transfer*, 15, 301-314, 1972.

Kowalik, Z. and I. Polyakov. Tides in the Sea of Okhotsk, *J. Phys. Oceanogr.*, 28(7), 1389-1409, 1998.

Loder, J. W. and P. D. Greenberg. Predicted positions of tidal fronts in the Gulf of Maine region, *Continental Shelf Res.*, 6, 397-414, 1986.

Mellor, G. L. and T. Yamada. Development of a turbulent closure model for geophysical fluid problems, *Rev. Geophys. and Space Phys.* 20, 851-875, 1982.

Miles, J. W. Kelvin waves on oceanic boundaries, *J. Fluid. Mech.*, 55, 113-127, 1972.

Pickart, R. S. Bottom boundary layer structure and detachment in the shelfbreak jet of the Mddle Atlantic Bight, *J. Phys. Oceanogr.*, 30, 2668-2686, 2000.

Pingree, R. D., P. R. Pugh, P. M. Holligan, and G. R. Forster. Summer phytoplankton blooms and red tides along tidal fronts in the approaches to the English Channel, *Nature*, 258, 672-677, 1975.

Schumacher, J. D., T. H. Kinder, D. J. Pashinski , and R. L. Charnell. A structural front over the continental shelf of the Eastern Bering Sea, *J. Phys. Oceanogr.*, 9, 79-87, 1979.

Shchepetkin, A. F. and J. C. McWilliams. The Regional Oceanic Modeling System: A split-explicit, free-surface, topography-following-coordinate ocean model, *Ocean Model.*, 2004.

Shcherbina, A. Y., L. D. Talley, and D. L. Rudnick. Direct observations of North Pacific ventilation: brine rejection in the Okhotsk Sea, *Science*, 302(5652), 1952-1955, 2003.

Shcherbina, A. Y., L. D. Talley, and D. L. Rudnick. Dense water formation on the northwestern shelf of the Okhotsk Sea: 1. Direct observations of brine rejection, *J. Geophys. Res.*, 109, C09S08, doi:10.1029/2003JC002196, 2004a.

Shcherbina, A. Y., L. D. Talley, and D. L. Rudnick. Dense water formation on the northwestern shelf of the Okhotsk Sea: 2. Quantifying the transports, *J. Geophys. Res.*, 109, C09S09, doi:10.1029/2003JC002197, 2004b.

Simpson, J. H. and J. R. Hunter. Fronts in the Irish Sea, *Nature*, 250, 404-406, 1974.

Simpson, J. H. and I. D. James, Coastal and estuarine fronts, in *Baroclinic Processes on Continental Shelves, Coastal Estuarine Stud. Ser.*, vol. 3, edited by C. N. K. Mooers, pp. 69-93, AGU, Washington, D. C., 1986.

Song, Y. and D. B. Haidvogel. A semi-implicit ocean circulation model using a generalized topography-following coordinate system, *J. Comp. Phys.*, 115(1), 228-244, 1994.

Soulsby, R. L., The bottom boundary layer of the shelf seas, in *Physical oceanography of coastal and shelf seas*, edited by B. Johns, pp. 189-266, Elsevier Science Publ. Company, Inc., N.Y. 1983.

Stigebrandt, A. A note on the locus of a shelf front, *Tellus*, 40A, 439-442, 1988.

Warner, J. C., C. R. Sherwood, H. G. Arango, and R. P. Signell. Performance of four turbulence closure models implemented using a generic length scale method, *Ocean Model.*, 2004.

Figures:

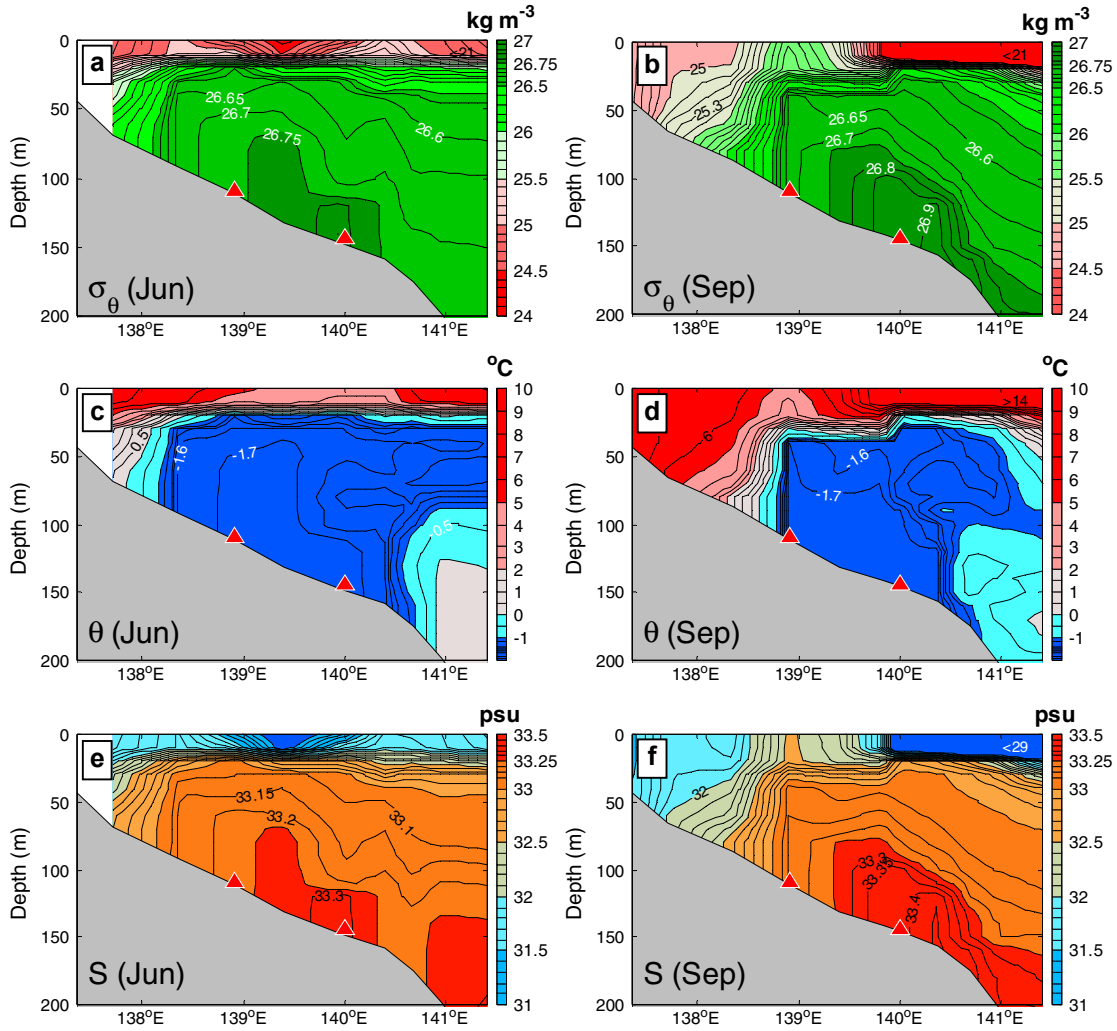

Fig. 4.1 Structure of the mixing front on the northwestern shelf of the Okhotsk Sea in June 2000 (a,c,e) and September 1999 (b,d,f). Potential density (a,b), potential temperature (c,d) and salinity (e,f) are shown. Red triangles mark the location of the bottom moorings.

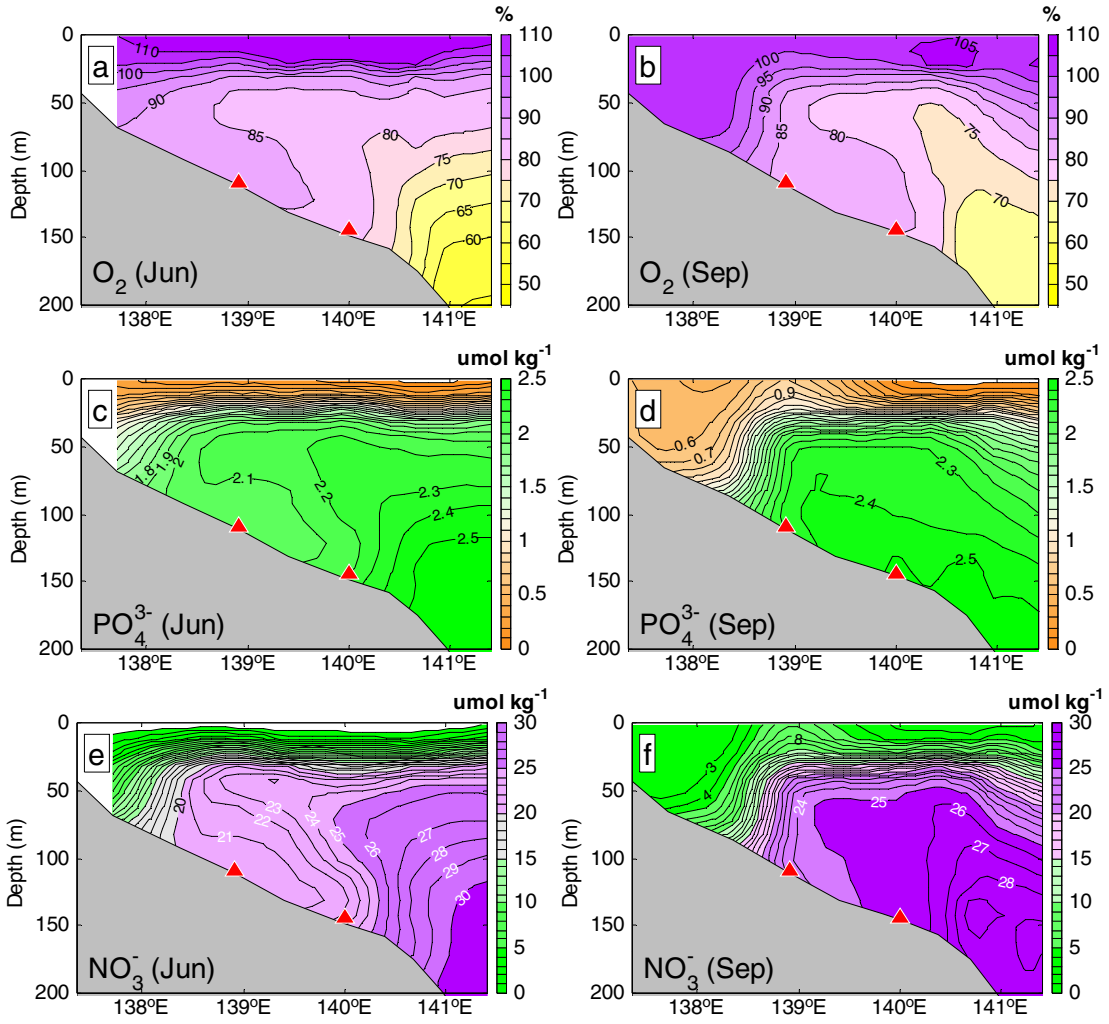

Fig. 4.2 Structure of the mixing front on the northwestern shelf of the Okhotsk Sea in June 2000 (a,c,e) and September 1999 (b,d,f). Oxygen saturation (a,b), phosphate (c,d) and nitrate (e,f) are shown. Red triangles mark the location of the bottom moorings.

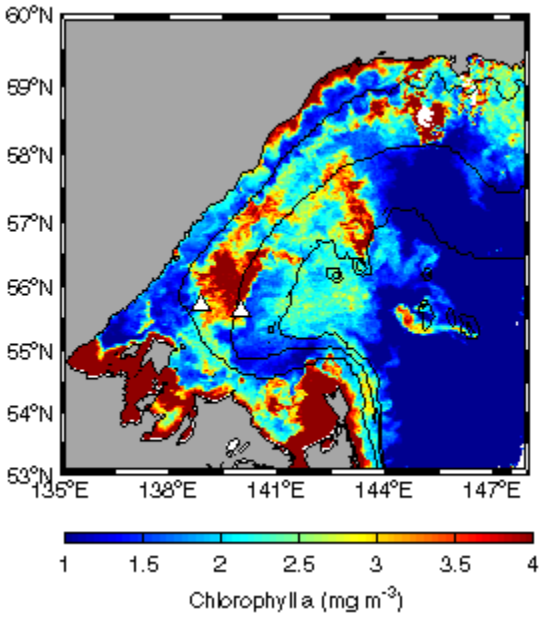

Fig. 4.3 SeaWiFS Chlorophyll-*a* concentration on the northwestern shelf of the Okhotsk Sea on 22 September 1999. Compare with SST distribution shown in Fig. 4.4a. White triangles mark the mooring positions. 100, 150, and 200 m isobaths are shown.

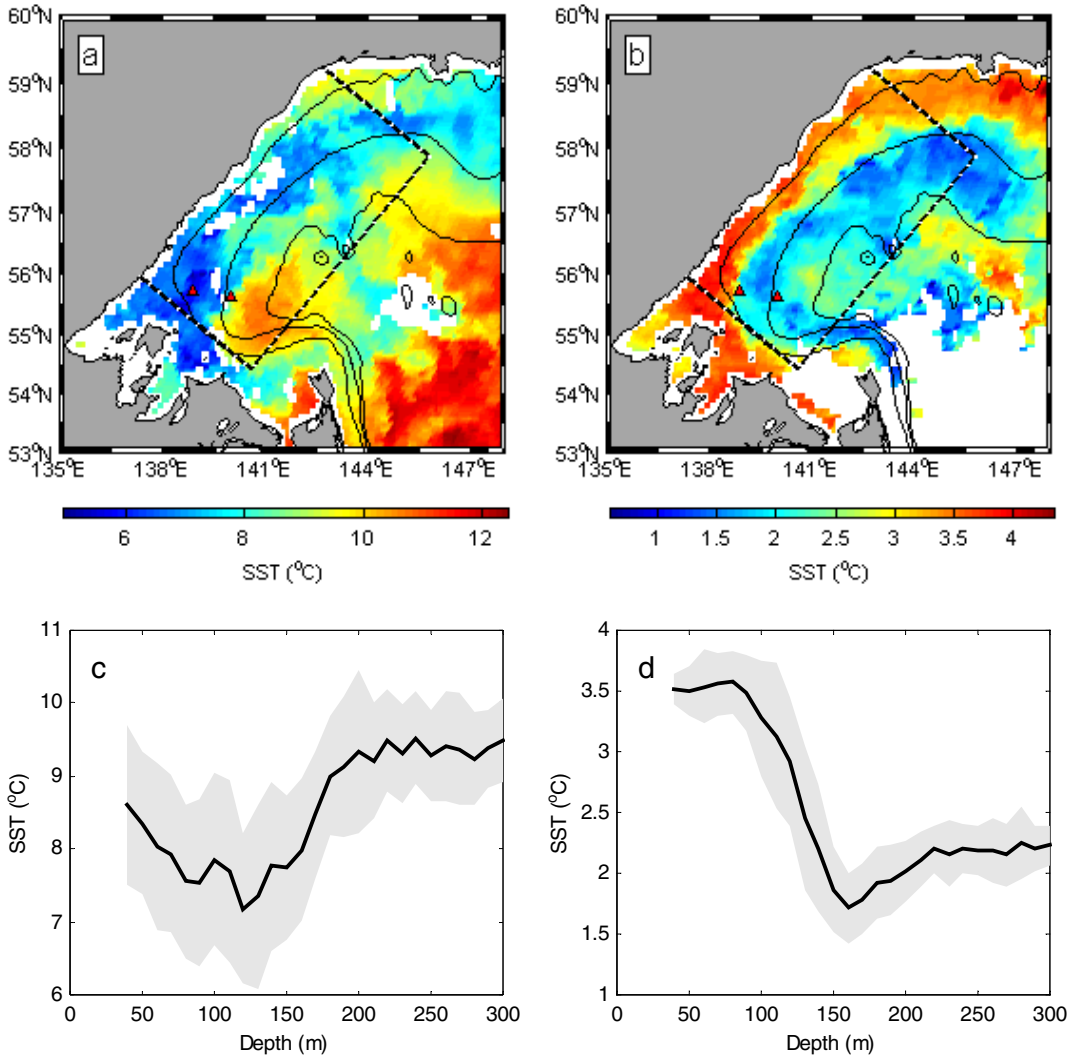

Fig. 4.4 Sea Surface Temperature (SST) on (a) 22 September 1999 and (b) 3 November 1999. Red triangles mark the mooring positions. 100, 150, and 200 m isobaths are shown. Panels (c) and (d) show average SST as a function of bottom depth for the SST images shown in (a) and (b), respectively. Gray shading represents one standard deviation. Area of averaging is shown by dashed lines in (a) and (b).

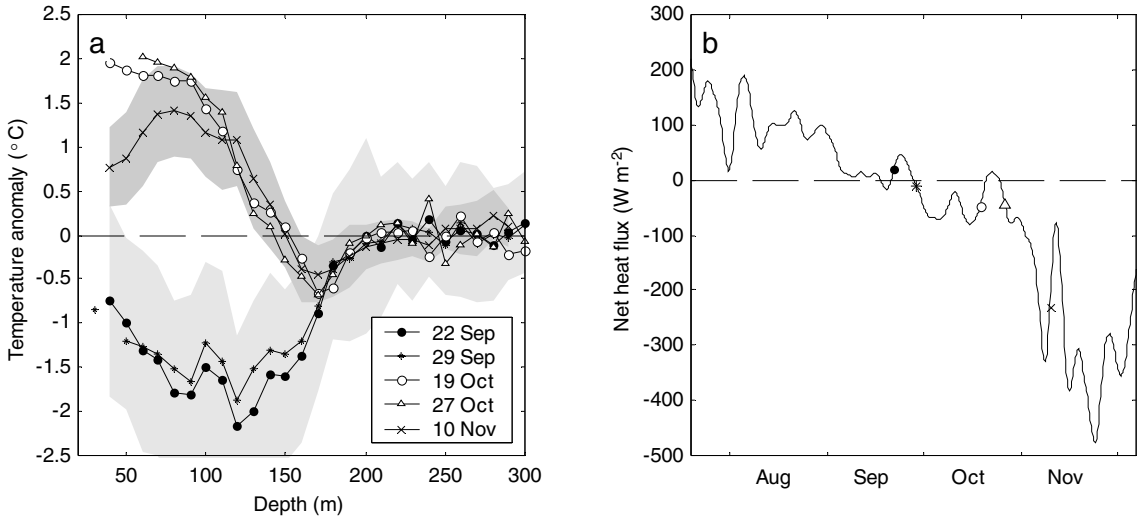

Fig. 4.5 (a) Ocean Pathfinder AVHRR sea surface temperature anomaly (relative to the offshore temperatures) on the northwestern shelf as a function of bottom depth. One standard deviation is shown for the first and the last profiles by gray shading (standard deviation of intermediate profiles is simiar). (b) ECMWF net heat flux on the northwestern shelf (142.5˚E, 57.5˚N), low-passed with 8-day Blackman filter. Symbols correspond to the dates shown in (a).

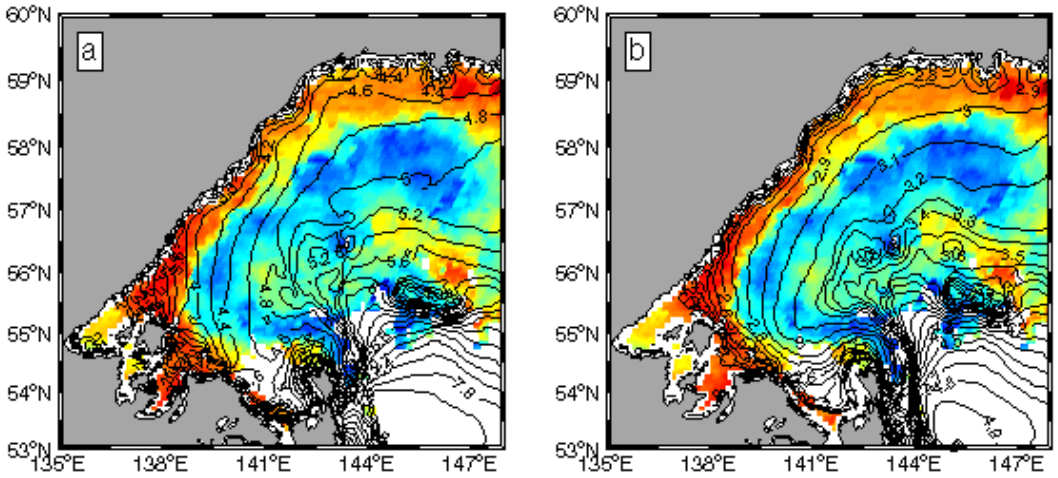

Fig. 4.6 AVHRR SST images taken on 3 November 1999, with the overlain contours of (a) $\log_{10}(h/\langle u^3 \rangle)$ and (b) $\log_{10}(h/\langle u \rangle)$, where h is the water depth in meters, u is the tidal flow speed in meters per second, and angle brackets represent averaging over the tidal cycle. M_2 component data from the Okhotsk Sea regional tidal model [*Kowalik and Polyakov*, 1998] are used.

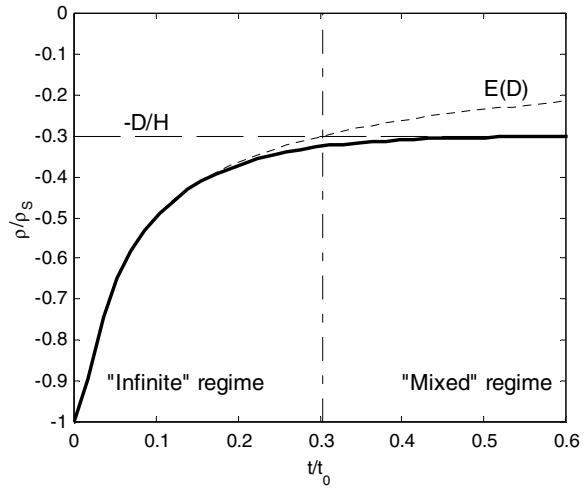

Fig. 4.7 Evolution of surface density anomaly for the case of step-function mixing (black line). The dashed and dotted lines show the asymptotics for the "mixed" (ρ=-$\rho_S D/H$) and "infinite" (ρ=-$\rho_S E_D$) regimes, respectively. Vertical dash-dot line indicates the approximate boundary between the two regimes. See text for details.

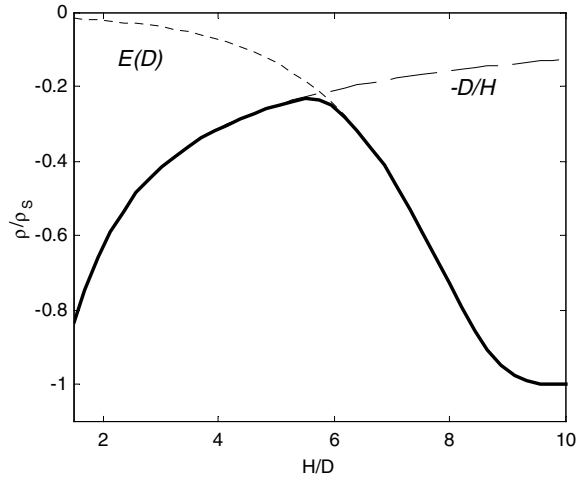

Fig. 4.8 Surface density anomaly as a function of non-dimensional bottom depth (thick line). The dashed and dotted lines show the asymptotics for the "mixed" (ρ=-$\rho_S D/H$) and "infinite" (ρ=-$\rho_S E(D)$) regimes, respectively. See text for details.

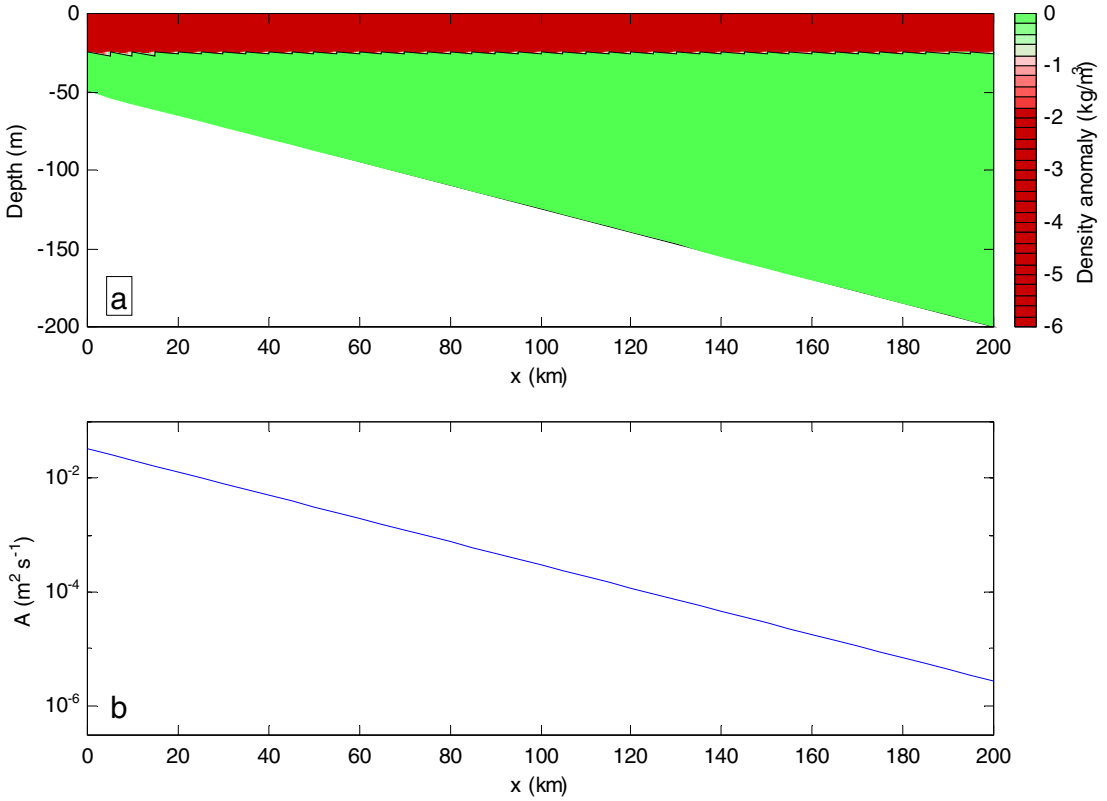

Fig. 4.9 Formulation of one-dimensional mixing model. (a) Initial density distribution. (b) Imposed cross-shore distribution of vertical diffusivity coefficient.

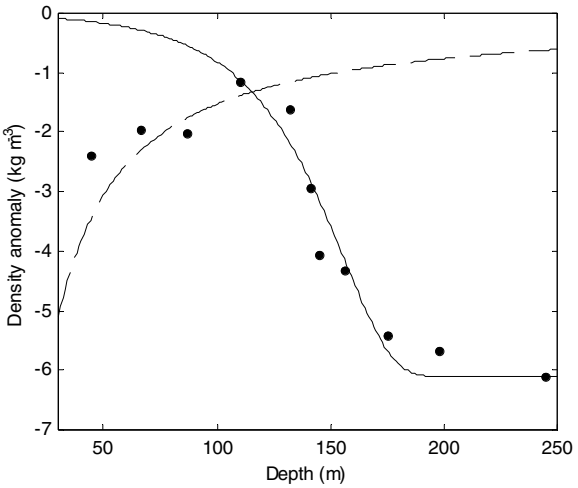

Fig. 4.10 Surface density anomaly relative to the offshore bottom density observed on the September 1999 section (dots) and analytical prediction for the "mixed" (dashed line) and "infinite" (solid line) regimes after 90 days of mixing with the vertical diffusivity shown in (Fig. 4.9b).

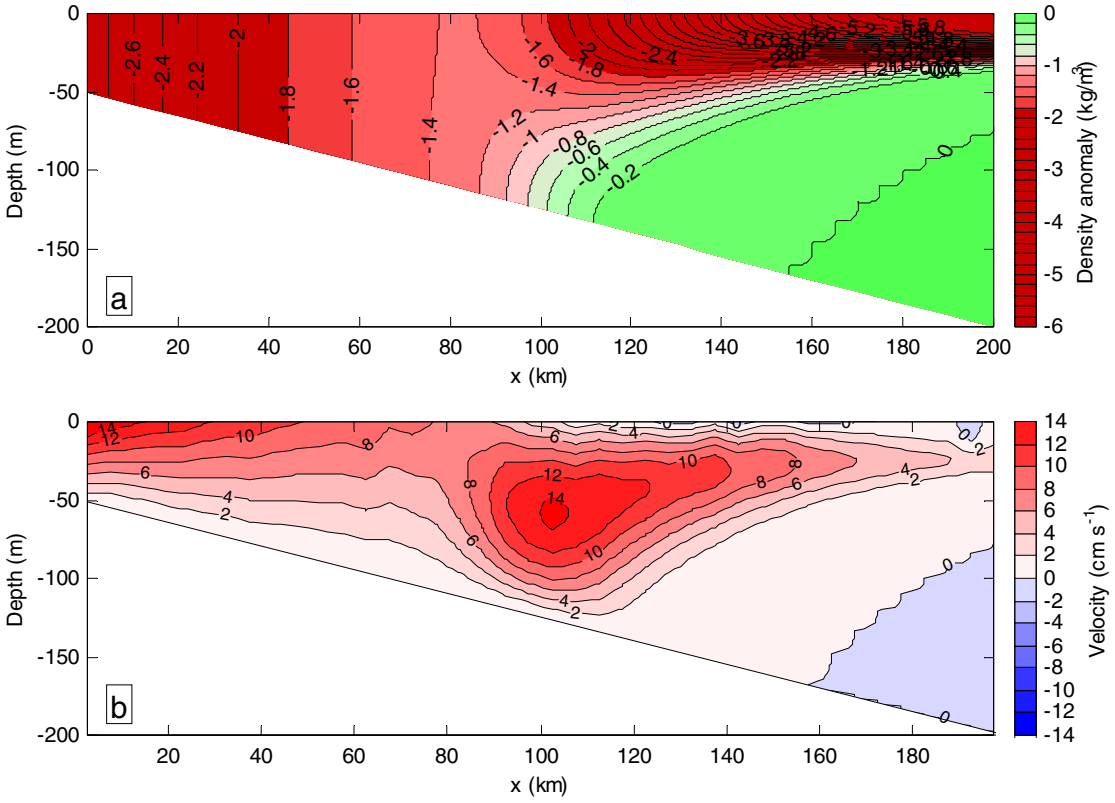

Fig. 4.11 Results of 90-day run of the 1^{D}-mixing model (a) Density anomaly structure. (b) Geostrophic velocity (positive westward).

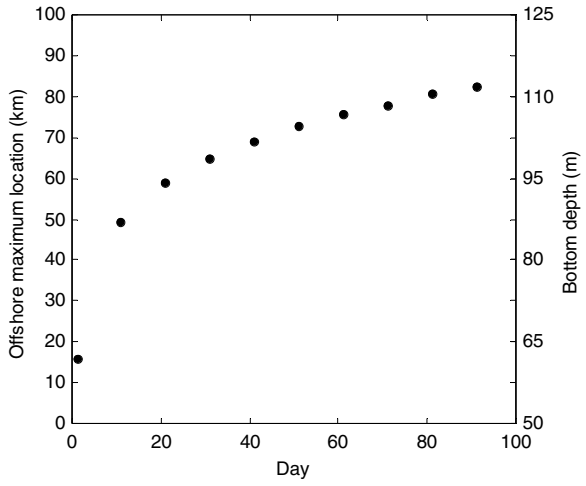

Fig. 4.12 Location of the surface density maximum for the one-dimensional model of Fig. 4.9 and Fig. 4.11.

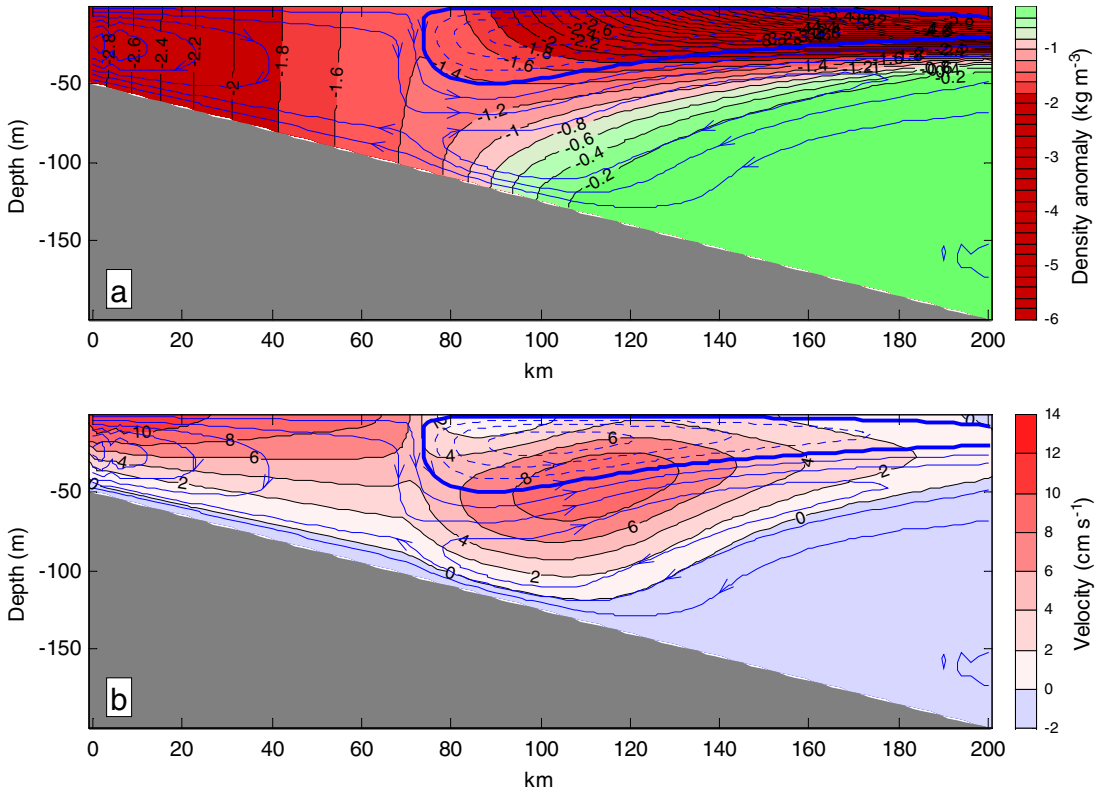

Fig. 4.13 Results of a 90-day run of a two-dimensional primitive equation simulation. (a) Density anomaly distribution and (b) alongshore current. Blue contours show the streamfunctions of the secondary circulation in the plane of the section. The contour interval is 5×10^{-2} m^2 s^{-1}. Negative contours are dashed. Zero contour is bold.

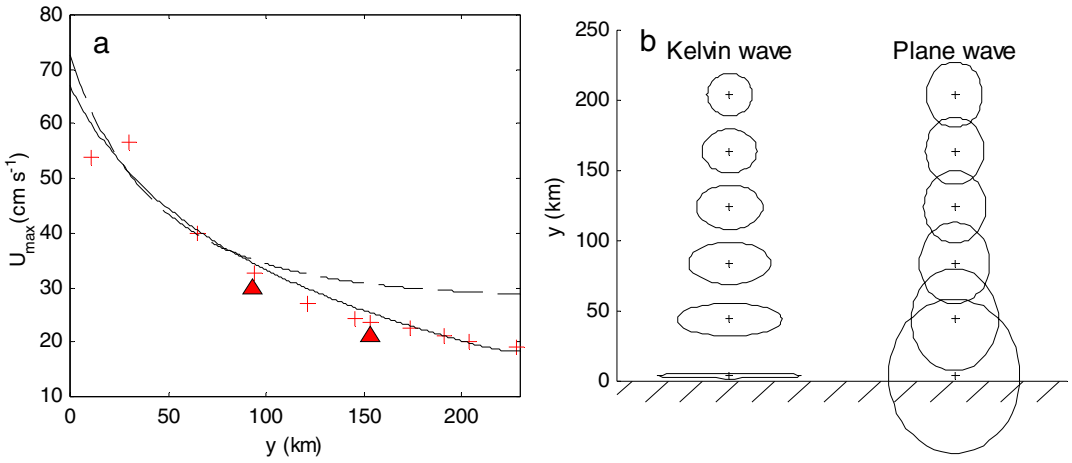

Fig. 4.14 (a) Cross-shelf variation of the amplitude of M_2 tidal current for Kelvin wave (solid line) and plane wave (dashed line) solutions. Depth distribution is the same as in Fig. 4.9a. Red crosses show the prediction of Okhotsk Sea regional tidal model [*Kowalik and Polyakov*, 1998]. Red triangles are the M_2 tidal velocity amplitudes observed by the bottom moorings in 1999-2000. (b) Shape of the tidal ellipses for Kelvin wave (left) and plane wave (right) solutions.

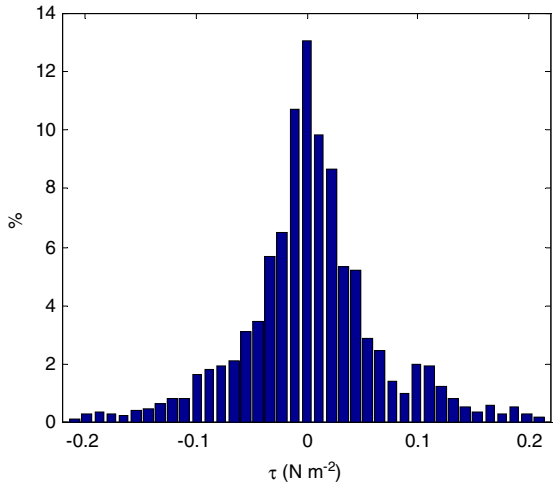

Fig. 4.15 Distribution of wind stress anomaly on the northwestern shelf of the Okhotsk Sea in August 1999 – June 2000, based on the ECMWF 4-times daily reanalysis.

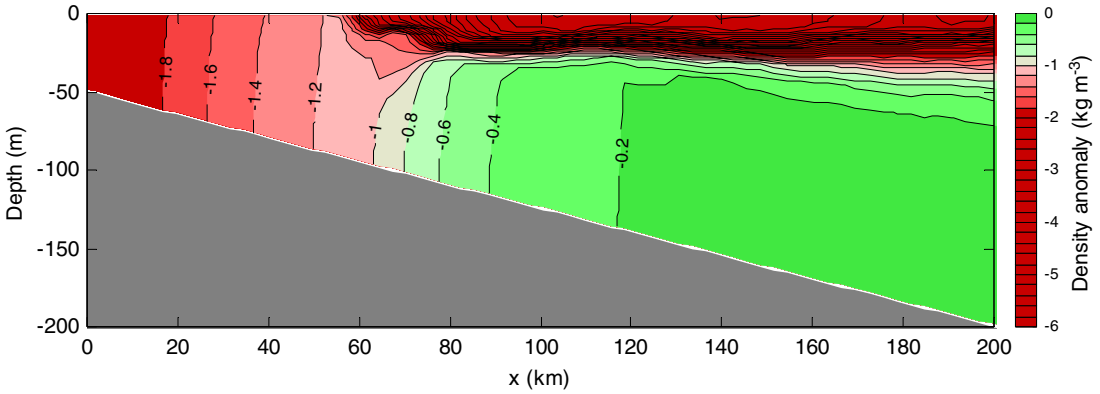

Fig. 4.16 Density distribution at the end of 90-day run of the two-dimensional tidal mixing model.

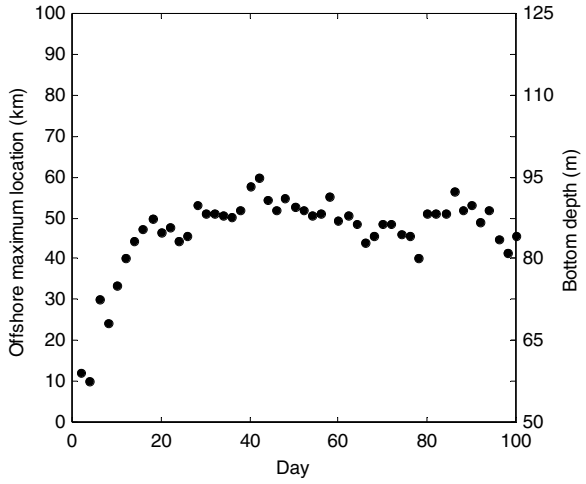

Fig. 4.17 Location of the surface density maximum for the two-dimensional tidal mixing model.

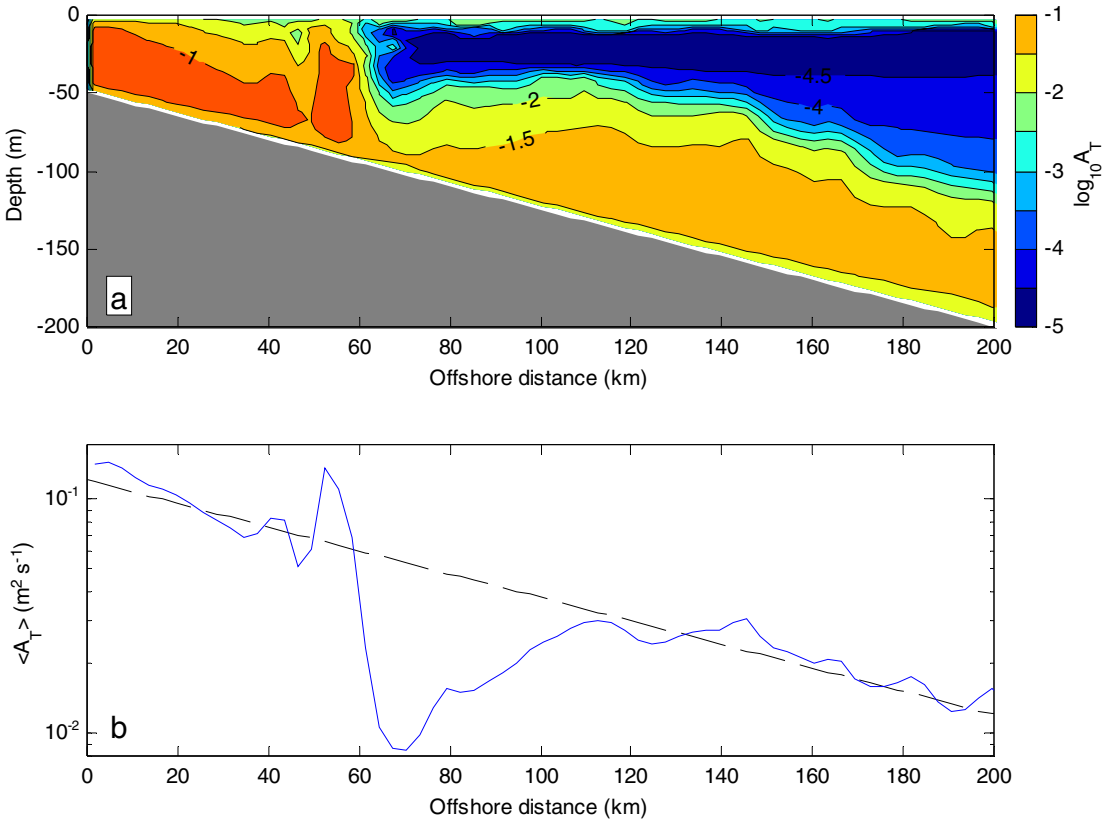

Fig. 4.18 (a) Distribution of vertical eddy diffusivity at the end of 90-day run of 2-dimensional tidal mixing model. (b) Mean vertical eddy diffusivity as a function of the distance offshore. Dashed line shows an arbitrary exponential decay for the reference.

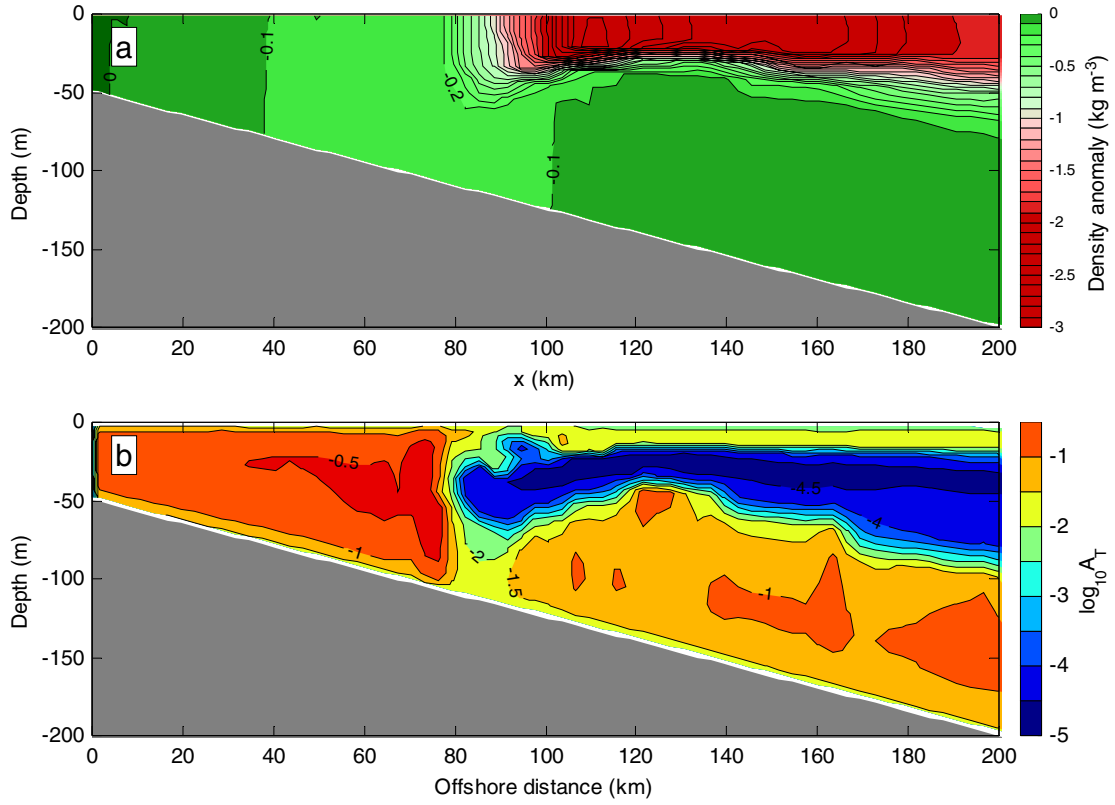

Fig. 4.19 Distribution of (a) density anomaly and (b) vertical eddy diffusivity at the end of 30-day fall cooling run.

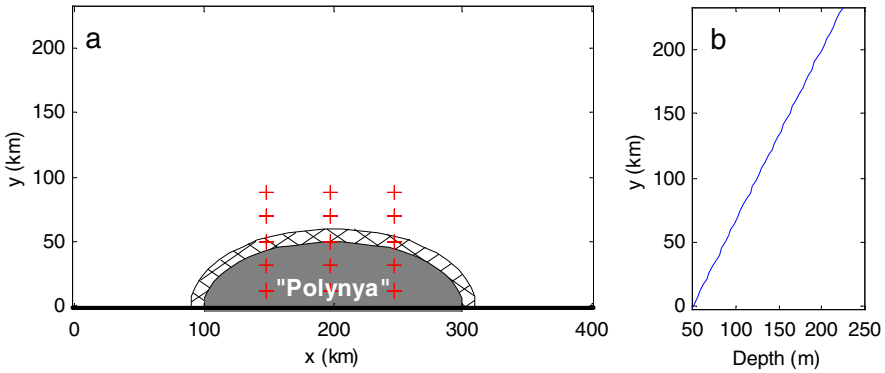

Fig. 4.20 (a) Schematics of the model domain for the numerical polynya experiment. Elliptical region of intense buoyancy loss ("polynya") is shaded. The transition zone, where the buoyancy loss decays linearly towards zero, is hatched. Red crosses show the location of virtual moorings. Thick line represents the closed southern boundary condition. (b) Depth distribution across the domain.

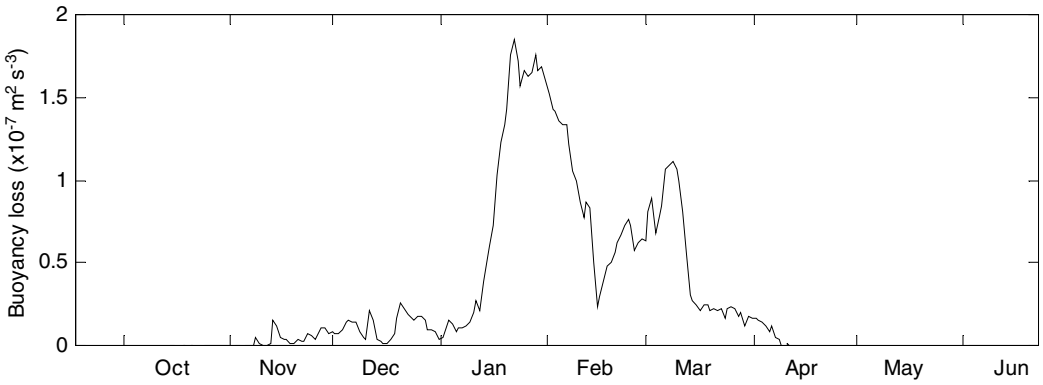

Fig. 4.21 Mean buoyancy loss due to brine rejection in the northwestern polynya (defined as the area north of 55ºN, west of 144ºE, and inshore of 200-m isobath). The estimates of ice formation rates are based upon European Centre for Medium-Range Weather Forecasts (ECMWF) reanalysis meteorology and National Snow and Ice Data Center ice data [*Shcherbina et al.*, 2004b].

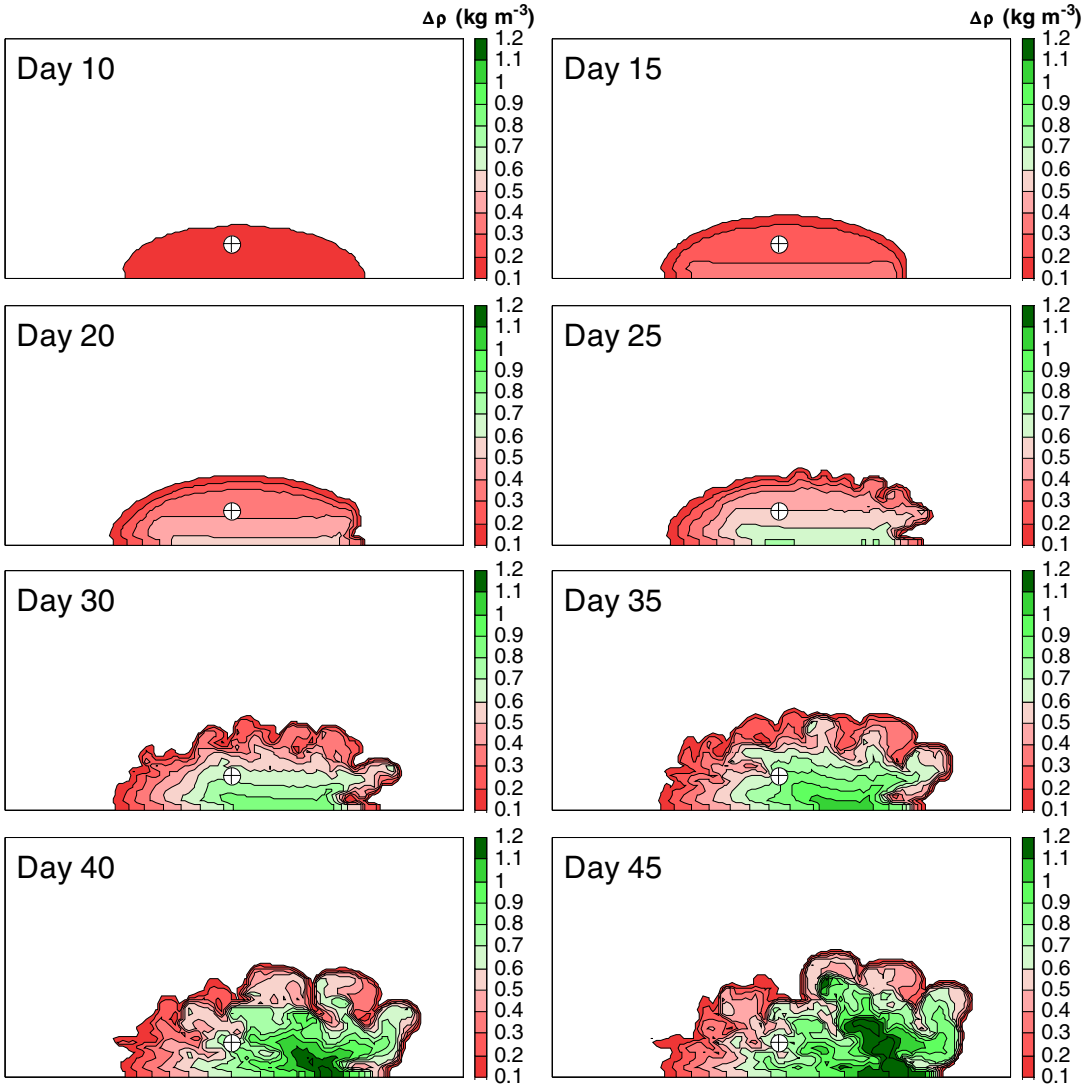

Fig. 4.22 Evolution of bottom density anomaly. Constant buoyancy loss $B=2\times10^{-7}$ m^2 s^{-3} starts at day 5. Circle with a cross marks the position of virtual mooring used for Fig. 4.24 and Fig. 4.25.

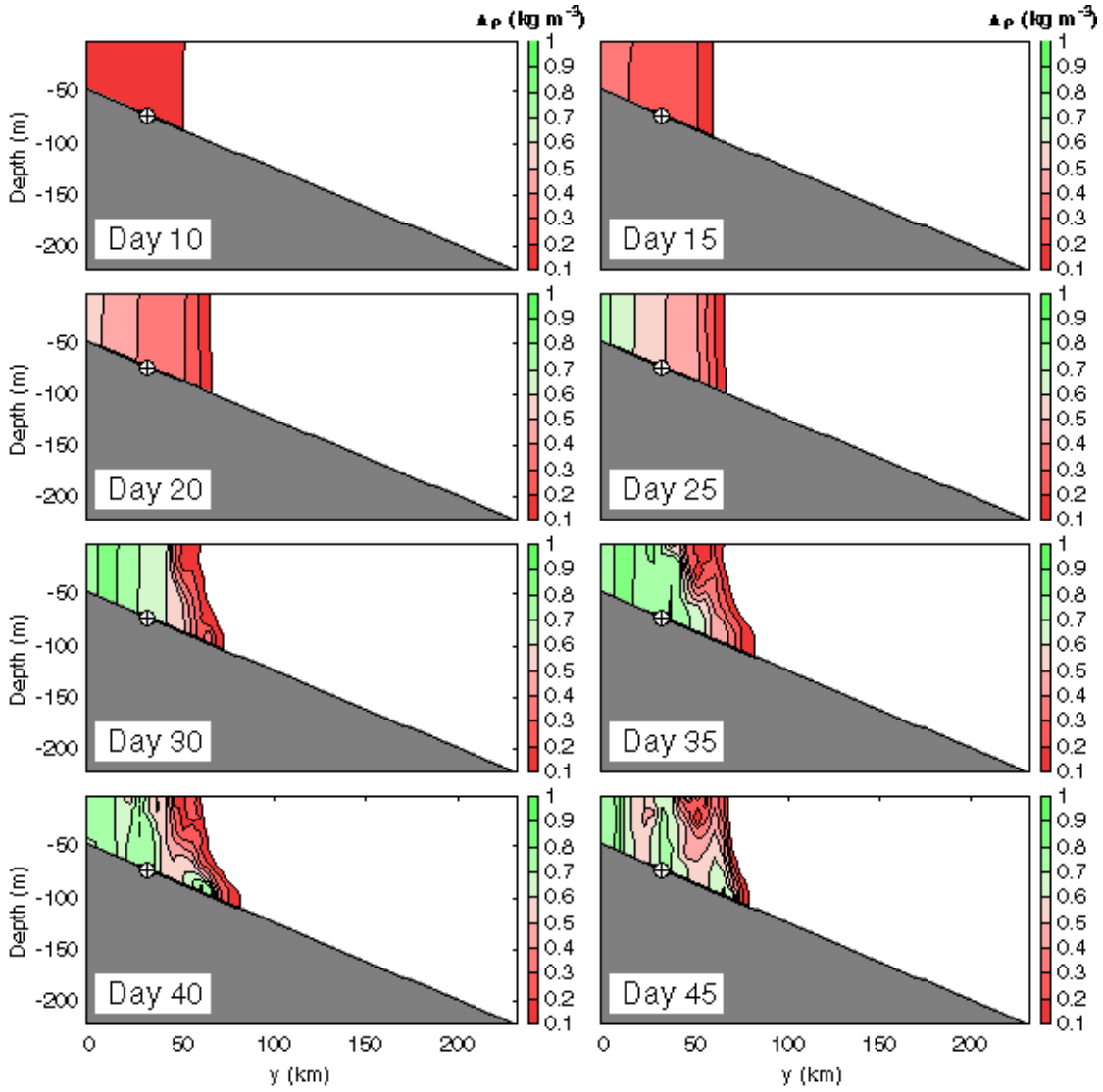

Fig. 4.23 Evolution of density anomaly on a cross-shelf section. Constant buoyancy loss $B=2\times10^{-7}$ m^2 s^{-3} starts at day 5. Circle with a cross marks the position of virtual mooring used for Fig. 4.24 and Fig. 4.25.

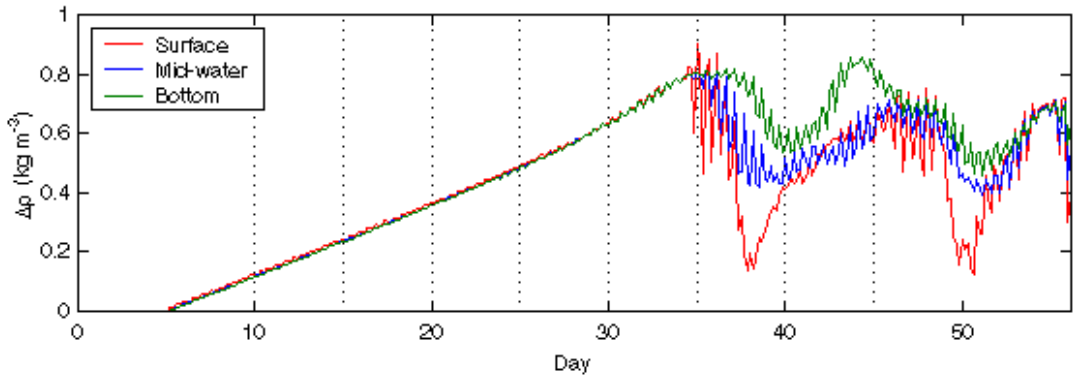

Fig. 4.24 Evolution of density anomaly on a virtual station at the surface (red), middle (blue) and bottom (green). Station position is shown in Fig. 4.22 and Fig. 4.23. Vertical dotted lines correspond to the times of snapshots shown in Fig. 4.22 and Fig. 4.23.

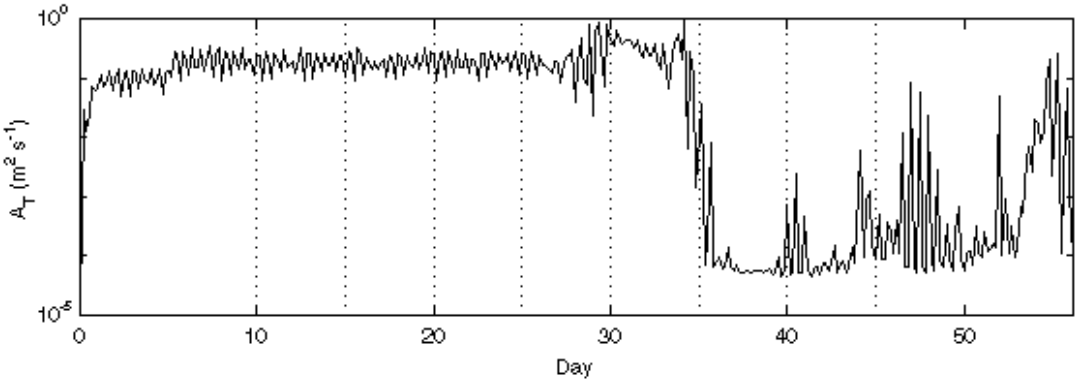

Fig. 4.25 Vertical eddy diffusivity on a virtual station (mid-water). Station position is shown in Fig. 4.22 and Fig. 4.23. Vertical dotted lines correspond to the times of snapshots shown in Fig. 4.22 and Fig. 4.23.

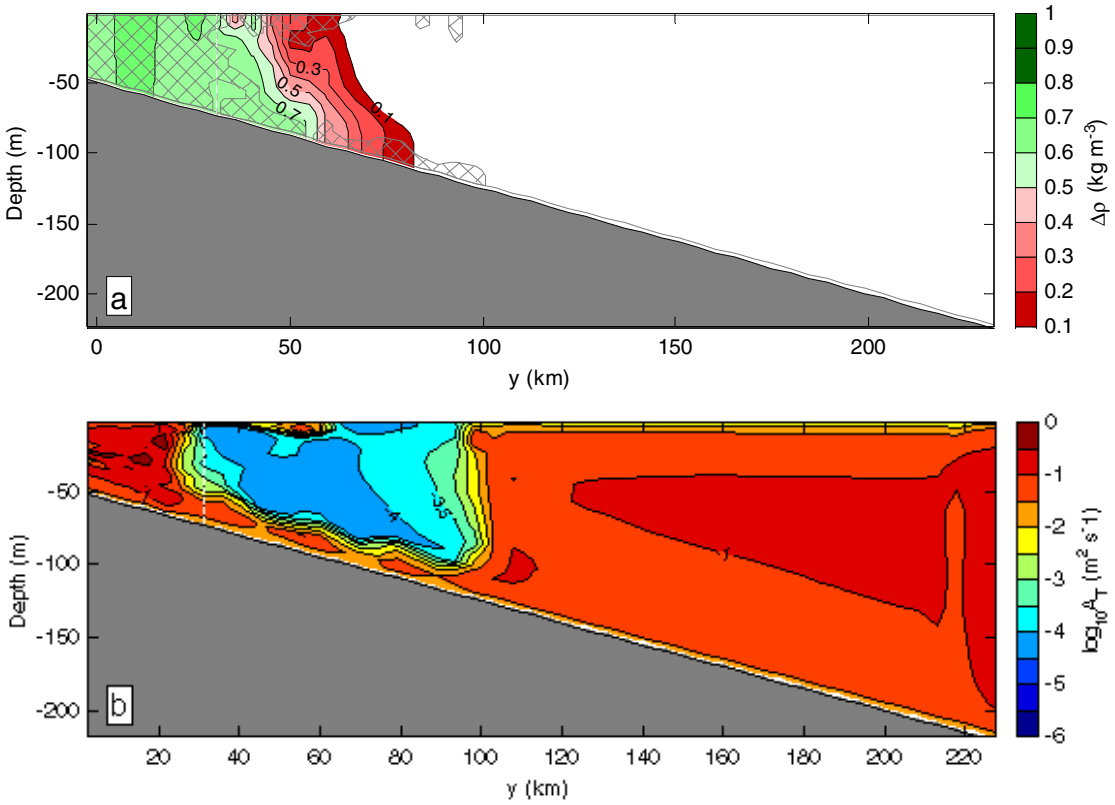

Fig. 4.26 (a) Density anomaly and (b) vertical eddy diffusivity on a cross-shelf section (day 35). Regions of density inversion are hatched.

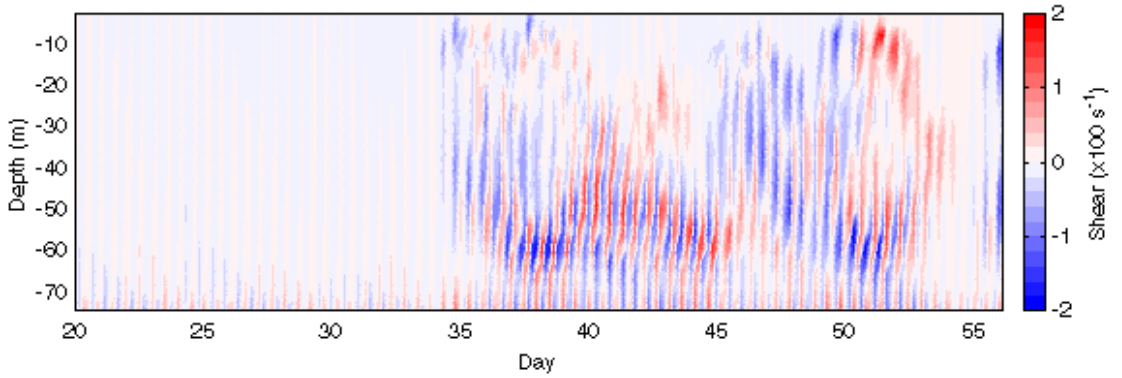

Fig. 4.27 Evolution of vertical shear of cross-shore velocity component on a virtual station. Station position is shown in Fig. 4.22 and Fig. 4.23.

CHAPTER V

Ice-Draft Profiling from Moored ADCP Data

The text of this chapter, in full, is a reprint of the material as it appears in Shcherbina, A. Y., L. D. Talley, and D. L. Rudnick, Ice-Draft Profiling from Moored ADCP Data, *J. Atmos. Ocean. Tech.*, (submitted). The dissertation author was the primary researcher and author, and the co-authors listed in this publication directed and supervised the research which forms the basis for this chapter.

Abstract.

The feasibility of ice-draft profiling using an upward-looking bottom-moored acoustic Doppler current profiler (ADCP) is demonstrated. Ice draft is determined as the difference between the instrument depth, derived from high-accuracy pressure data, and the distance to the lower ice surface, determined by ADCP echo travel time. Algorithms for surface range estimate from the water-track echo intensity profiles, data quality control and correction have been developed. Sources of error in using an ADCP as an ice profiler were investigated using the models of sound signal propagation and reflection. The effects of atmospheric pressure changes, sound speed variation, finite instrument beamwidth, hardware signal processing, instrument tilt, beam misalignment and vertical sensor offset are quantified. The developed algorithms are tested using the data from the winter-long ADCP deployment on the northwestern shelf of the Okhotsk Sea.

1 Introduction

The use of ADCPs for ice draft (thickness of the submerged ice part) measurement was first proposed by Visbeck and Fischer [1995]. They suggested that a combination of an ADCP with a high-accuracy pressure sensor would allow simultaneous measurements of the water depth and the distance to the lower ice surface, allowing ice draft to be obtained as the difference of the two. A similar method is widely used in specialized ice profiling sonars [*Melling*, 1998], but it has heretofore not been implemented using ADCPs because sufficiently accurate pressure sensors had not been used.

A typical ADCP offers at least two methods of estimating the distance to the surface. First, a dedicated bottom-tracking mode of an ADCP can be used. In this mode specially-configured and specially-processed pings are used to establish the range and the velocity of a reflective surface with high accuracy (on the order of 0.1 m) [*Gordon*, 1996]. Second, the distance to the surface can be determined by post-processing of the echo amplitude profiles of regular ("water-tracking") pings [*Visbeck*, 2002]. The vertical sampling of such profiles is typically quite coarse (2-8 m) compared to the expected variability of the ice surface. However, as shown by Visbeck and Fischer [1995] and in the present study, the surface reflection peak in the echo intensity is well-defined even with such relatively low resolution. As a result, fitting a theoretical curve to the shape of the peak has a potential of increasing the resolution of the surface location by utilizing the data in several neighboring depth bins. Additional averaging over the four ADCP beams and over time is expected to reduce the statistical error further. The present study explores and compares the performance of

both bottom-tracking and water-tracking methods applied to estimating the distances to the water-air and water-ice interfaces. Additionally, the effects of sound scattering and signal processing relevant to the problem of correct surface location, as well as the steps necessary to account for such effects are discussed.

We performed concurrent ADCP and bottom pressure measurements in 1999-2000 using bottom moorings during an Okhotsk Sea shelf polynya experiment. The primary reason for the experiment was to track water property and velocity changes in the polynya that is responsible for formation of the densest ventilated water in the North Pacific [*Shcherbina et al.*, 2004]. For quantitative flux budgets, it would be useful to know how much ice formed in the polynya, which involves tracking both the thickness and movement of the ice. The preferred in situ instrument for measuring ice thickness is the upward looking ice profiling sonar (IPS) [*Melling*, 1998], which uses a single vertical beam and has higher vertical resolution (~20 cm) than the ADCP. However, these instruments could not be included in our experiment due to funding constraints. Therefore we have attempted to reconstruct ice thickness from the ADCP information. As the bottom-mounted instruments used in our experiment combined upward-looking ADCPs with high-accuracy pressure sensors and the added benefit of instrument stability, they were promising for this task. Section 2 below provides the information about the mooring equipment, section 3 describes the algorithm of ice draft estimation using ADCP data and correction procedures. Results of observations are shown in section 4.

2 Measurements and instrumentation

In a winter polynya study on the broad continental shelf in the northwestern Okhotsk Sea, two fixed bottom moorings ("landers") were deployed at (55°45'N, 138°54'E) and (55°39'N, 140°00'E) in 109 and 144 m of water correspondingly (Fig. 5.1), and will be hereafter referred to as the "western" (shallower) and the "eastern" (deeper) ones. The landers were deployed in September, 1999 and were recovered in June, 2000 from the R/V Khromov. The instruments were mounted in a fixed fiberglass hull (Fig. 1b) and so were not subject to mooring motion. Each lander was equipped with an upward-looking RDI Workhorse 300 kHz broadband ADCP and a Paroscientific Digiquartz pressure sensor, the latter as part of a Seabird Seacat SBE 16-03 which also included temperature and conductivity measurements. Pressure, conductivity, and temperature were recorded with a 15-minute sampling interval.

Each ADCP recorded the averages of 70 pings for each 16-minute ensemble; the vertical bin size was 4 m. Both ADCPs operated in "bottom-tracking" (BT) mode, which in this case measured the distance to and speed of ice using dedicated pings and signal processing different from that used for water velocity profiling. 3 BT pings distributed among the regular ("water-tracking") pings of each 16-minute ensemble were used.

The data from the shallower mooring will be used in the following sections to illustrate the algorithm of ice draft estimation and data correction procedures. The results from both moorings are discussed in section 4.

3 Ice draft profiling with ADCP

The thickness of the submerged part of ice sheet ("ice draft") can be deduced as the difference between the instrument depth *H* and the distance to the lower ice surface *h (*Fig. 5.2*)*:

$$d = H - h. \tag{25}$$

As the water depth changes with tidal oscillations, the instantaneous depth is determined from the in-situ water pressure *P*:

$$H = P / \left(g \overline{\rho} \right), \tag{26}$$

where *g* is the gravitational acceleration and $\overline{\rho}$ is the vertical average of water density. $\overline{\rho}$ was calculated using the density measured at the bottom and assumptions about the thermocline shape obtained from measured density profile and satellite observations of surface temperature (see section 3.5.2).

In our experiment setup the ADCPs were used to determine the distance *h* to the surface based on the travel time of the sound reflected by the surface. Due to the high reflectivity of the interface, a typical echo amplitude profile exhibits a prominent peak near the surface (Fig. 5.3), so the distance to the surface can be inferred from the location of the echo intensity maximum. However, the apparent location of this maximum is shifted relative to the true distance to the surface due to the combined effect of the fairly wide ADCP beam and the steep dependence of surface reflectivity

on the incidence angle. Additional bias is introduced by the RDI ADCP signal processing circuitry. Section 3.1 below details the effect of these factors on the shape and location of the surface maximum. The algorithms for surface range estimate and quality control are described in sections 3.2-3.3, and their performance is compared with the BT algorithm in section 3.4. Section 3.5 outlines the correction procedures, designed to reduce the effects of changing atmospheric pressure, sound speed variation, beamwidth offset and the instrument misalignment on the ice-draft estimate.

3.1 ADCP's surface echo formation

The echo intensity recorded by an ADCP is a result of a chain of processes: emission of a sound signal, its propagation through the water column, sound scattering from suspended particles and the surface interface, and, finally, the return signal acquisition and pre-processing. Among these processes, surface scattering (section 3.1.1) and signal pre-processing (section 3.1.2) are especially important for the problem of surface range estimation, since they control the location of the surface echo intensity peak.

3.1.1 Surface reflection

Due to the finite width of an ADCP beam, it insonifies not a point but an ellipse on the water (ice) surface. The beamwidth of a 300-kHz RDI ADCP corresponds to a 8x10 m footprint on a surface 100 m away from the instrument. The incidence angle within this ellipse varies from 18° to 22°. Coincidently, the scattering strength of the water surface changes most rapidly between 10° and 20° [*Urick*, 1956], so the backscatter from the leading edge of the footprint (low incidence angle) is appreciably

stronger than from the trailing edge. Additionally, the leading edge is located closer to the instrument, which leads to slightly lower attenuation of the sound reflected from it. As a result, the echo level maximum shifts from the center of the ellipse (Fig. 5.4) [*Visbeck, personal communication*]. Consequently, the effective beam angle is less than the nominal one, and the inferred distance to the surface is biased low.

This effect can be illustrated with a simple model of the surface reflection of an ADCP beam. The level of the echo *EL* reflected from the surface at an angle θ from the vertical is [*Urick*, 1975]

$$EL(\theta)=SL+TL+S_s, \tag{27}$$

where *SL* is the source level, *TL* is the transmission loss, and S_s is the surface scattering strength, all expressed in decibels. (Volume backscattering has been neglected in this consideration.) We vary θ within ±5° to form a cone around the ADCP beam axis, inclined at an angle θ_0=20° to the vertical. We assume quadratic decay of the ADCP source level away from the beam axis, modeled as

$$SL = SL_0 - 3\frac{\Delta\theta^2}{\theta_{hw}{}^2}, \tag{28}$$

where $\Delta\theta$ is the angle measured from the axis of the beam, θ_{hw} is the beam half-width (2.2° for 300 kHz RDI ADCP), and SL_0 is an arbitrary constant. Following *Gordon* [1996], transmission loss is defined as

$$TL=-20\log_{10}(R)-2\alpha R, \tag{29}$$

where α=0.073 is the absorption coefficient, and $R= H\cos\theta_0/\cos(\theta)$ is the radial distance to the surface, and *H* is the instrument depth.

Surface scattering S_s varies greatly depending on surface roughness [*Urick*, 1975], which is affected by wind conditions and presence of ice. For this model we use Chapman and Scott's [1964b] approximation

$$S_s=-10\log_{10}8\pi\eta^2-2.17\,\eta^{-2}\tan^{-2}(90-\theta), \quad (30)$$

where η^2 is the mean-square slope of the surface irregularities. For the open water (OW) conditions, η^2 corresponds to the mean-square slope of wind waves, which is related to the wind speed W using the empirical relationship [*Cox and Munk*, 1954]

$$\eta^2=0.003+5.12\times10^{-3}W, \quad (31)$$

where W is expressed in meters per second.

Distribution of the terms of equation (27) across the beam is shown in Fig. 5.5a for a typical wind speed of W=5 m/s observed at the mooring location in autumn. It can be seen that the maximum echo level is achieved at an angle θ_{eff}=19°, which can be interpreted as an "effective beam angle". Since the echo from this angle arrives earlier than the one from the nominal beam angle, the distance to the surface is underestimated by 0.7 m compared to the true H=110 m. This effect becomes more pronounced as the reflection becomes more specular at lower wind speed (Fig. 5.5b). At W=1 m/s the bias in the range estimate reaches 1.73 m. It should be noted that this bias is a result of inherent ADCP features: the 20° beam slant that leads to the maximum variation of surface scattering strength across the beam, which is also fairly wide. Both BT and WT range estimates are equally susceptible to this bias.

The model of the beamwidth bias is equally applicable to the ice-covered (IC) conditions, provided an appropriate value of mean-square slope η^2 is substituted. The acoustic behavior of young sea ice is similar to that of the surface wave field generated

by 7-10 m/s winds [*Chapman and Scott*, 1964a; *Macpherson*, 1963], and the mean-square slope of the young ice can be approximated to the first order by substituting an appropriate W in (31).

The beamwidth bias may be the biggest obstacle in ADCP ice profiling, as it depends on ice roughness, which, in turn, may be correlated with the ice thickness. Consequently, the signals of ice roughness and thickness are likely to be aliased in the ADCP draft measurements. It appears impossible to separate these signals without external information about ice roughness. During the OW periods, this beamwidth bias is expected to have even greater variability in response to changes of surface roughness.

The above model is applicable for infinitely short pings. Broadband ADCPs use coded pulses with the duration τ almost equivalent to the vertical bin size (τ=3.83 m in our case). As a result, the pulses overlap, so that the return echo time series is effectively smoothed with the rectangular window of length τ.

3.1.2 Hardware signal processing

An ADCP's primary purpose is accurate velocity measurement. Echo intensity profiling, on the other hand, is an ancillary task, intended chiefly for quality control. Consequently, the details of the echo signal pre-processing are rarely known or controlled. Unfortunately, some of the aspects of such pre-processing lead to significant shift of the surface peak.

A time series of echo intensity is obtained by the ADCP's Return Signal Strength Indicator (RSSI) circuit. Time t elapsed between the ping start and arrival of an echo

can be converted to the vertical distance (range) to the echo origin as $h=0.5ct\cos\theta_0$, where c is the sound speed and θ_0 is the nominal beam angle. Consequently, the time series of echo intensity can be interchangeably interpreted as functions of range. Similarly, the temporal parameters such as pulse length are commonly expressed in units of length, implicitly implying such equivalence.

According to RDI [*P. Spain, personal communication*], the raw RSSI output is passed through a low-pass RC filter, which performance can be modeled as

$$W(\tau)=\exp(-\tau/\tau_{RC}), \tag{32}$$

where τ_{RC} is a time constant equivalent to 25-50% of the bin length. The exact value of the time constant is determined by the hardware based on the chosen bin length, but it is not reported to the firmware and should be assumed unknown. Since the filter is strongly asymmetric, the surface peak is shifted forward in time, and, consequently, in range (Fig. 5.6). The amount of shift of the maximum echo intensity depends on τ_{RC} and the shape of the original peak, and ranges from zero for a delta-function to approximately $1.96\tau_{RC}$ for a wide Gaussian peak. For τ_{RC} =2 m and the shape of the peak modeled in section 3.1.1, the shift is on the order of 1.5 m.

The filtered time series is then sampled near the *end* of the time gate corresponding to a given vertical bin (more precisely, with a delay of broadband code lag λ *after* the end of a gate), and the obtained value is assigned to the *middle* of the bin. Consequently, the peak is effectively shifted backwards in time and range by $\Delta h=0.5\tau_{BL}+\lambda$, where τ_{BL} is the bin length. In our case, τ_{BL}=4 m and λ =0.48 m, giving Δh=2.48 m. Overall, as a result of signal processing alone, the surface peak in the echo amplitude is shifted approximately 0.98 m closer to the instrument (Fig. 5.6).

We investigated a possibility of the reversal of the effect of the RC filter on the echo intensity record. However, poor knowledge of the filter time constant and sparse sampling of the surface echo peak make such reversal unfeasible. Consequently, we acknowledge the existence of the signal processing bias without attempting to correct it.

3.2 Determining location of the surface peak

The shape of the echo level peak associated with the surface can be approximated combining the models of surface reflection and signal processing discussed above (Fig. 5.7). The two most important features of the surface peak are its skewness and a prominent shift (up to several meters) relative to the true surface range. The observed peak in ADCP echo level is wider than the modeled and shows smoother transition to the volume back-scattering "floor". These discrepancies can be due to the effect of side-lobes in the emission diagram, as well as additional near-surface reflection caused by submerged air bubbles.

Ideally, distance to the surface and other model parameters (wind speed, source level, beamwidth) can be estimated by fitting the model curves to the observed echo level data. However even in a simple model these parameters control subtle changes of the shape of the peak, so accurate parameter estimation is not possible, given the coarse vertical resolution used in our experiment. Instead, a modified Gaussian profile was used to approximate the surface peak profile $A(z)$:

$$A(z) = a_0 \exp\left(-\left(\frac{z-h_0}{\delta}\right)^2\right) + a_1 z + a_2 , \quad (33)$$

where parameters a_0, a_1, a_2, h_0, and δ were obtained by the least-squares fit of (33) to the 11 points of each amplitude profile in the vicinity of the expected peak (Fig. 5.7). A weighted least squares algorithm was used, with the weights of data points proportional to the squares of the echo amplitudes, so that the values close to the maximum influence the fit more than the "tails". The linear term in (33) allows for echo amplitude changes caused by zooplankton congregation near the surface at night (mostly during the ice-free periods), which brings substantial periodic increase of the echo amplitude just below the surface (Fig. 5.8).

It is important to mention that the vertical coordinates z_i of the ADCP bins may vary from ping to ping. The reason for this variation is the changes in the effective length of transmit pulse with changing sound speed. (Note that this effect should be distinguished from the effect of changing in pulse travel time also caused by sound speed variation (see section 3.5.3.)) For most ADCP applications the vertical bin coordinates are retrieved once at the beginning of the record and assumed constant. However, for the purpose of surface range estimate the vertical bin coordinates should be computed for each ping separately to account for changing pulse length. In our case the position of the first bin varied by as much as 15 cm.

We understand that the modified Gaussian function is not an accurate approximation of the surface peak shape, which is markedly asymmetric (Fig. 5.7). Fitting a modified Gaussian shape (33) is, however, superior to a simple maximum search based on polynomial interpolation. Compared to the latter, our method provides

not only the estimate for the instrument to surface distance h_0, but also information about the width δ of the surface maximum and a standard deviation σ of the data from the fit, which can be used for quality control of the estimate of h, as described in the next section.

3.3 Filtering the WT signal

The fit (33) provides a variety of information about the shape of the surface maximum: location (h_0), height (a_0) and width (δ) of the peak, and the misfit (σ) between the data and a modified Gaussian model (33). These parameters can be used for filtering out the spurious range detections caused by unexpected surface reflection pattern. The peak characteristics may depend on the presence of ice at the surface, so the filtering parameters should be determined separately for ice-covered (IC) and open-water (OW) situations.

Presence of surface ice cover influences a wide range of the ADCP return signal parameters in addition to the echo amplitude, namely the correlation of surface reflection, and near-surface variances of horizontal, vertical and error velocities [*Visbeck and Fischer*, 1995]. It was empirically established that the value of signal correlation in the first bin above the mean surface level allows the most reliable detection of ice presence in our configuration, as its distributions for "definitely IC" (Feb. 15 – Mar. 15) and "definitely OW" (Oct. 15 – Nov. 15) exhibit the clearest separation. The critical value of correlation C_{ice}=92.3 optimally separates the two distributions, so that over 99.9% of correlation during the "definitely IC" period was higher than C_{ice}. Similarly, over 99.3% of correlation during the "definitely OW"

period was lower than C_{ice}. Consequently, we assume the surface ice is present whenever the signal correlation exceeded C_{ice}. Such ice detection also shows a good agreement with the SSM/I ice observations: correlation between the daily ice cover fractions determined with the two methods was 93%.

The distributions of surface peak width and height, determined by a modified Gaussian profile fitting, are noticeably different for the IC and OW periods distinguished using the ADCP signal correlation criterion (Fig. 5.10). Median values of surface peak width δ were 5.7 m and 7.2 m for IC and OW conditions correspondingly. The median values of peak height were 87.5 and 101.3 correspondingly.

Anomalously narrow and low surface peaks occurring predominantly during the OW periods likely indicate instances of specular reflection at the surface associated with calm conditions. In such conditions the return of the main lobe of the signal can be greatly reduced and the surface peak is largely due to side-lobe scattering. Consequently, the range estimated from such a peak is likely to be biased low, and thus should be excluded from analysis. At the same time, an anomalously wide surface peak may be due to enhanced sub-surface scattering caused by plankton congregation, and should also be excluded. Retaining only values within one standard deviation of the median value of peak width and within two standard deviations of the median value of peak height provided a reasonable balance of valid and false outlier detection. Additionally, range estimates associated with a high misfit between the observed echo amplitude data and modified Gaussian profile (33) should also be disregarded. An example of the effect of filtering on WT range estimates is shown in Fig. 5.11. On

average, approximately 17%, 6%, and 11% of the data were rejected by peak width, peak height, and misfit criteria correspondingly. Rejection rate was the highest (over 60%) during the spring melt, which was likely due to the greater variability of surface conditions.

3.4 Comparison of WT and BT

Surface range *h* can also be obtained using the BT mode of an ADCP. In this mode the ADCP periodically emits specially configured bottom-tracking pings, which are processed by the firmware to determine the location of the surface maximum of echo intensity. In BT mode the echo time series is sampled more frequently compared to WT mode [*Gordon*, 1996]. BT range, which is approximately twice the distance to the surface, is subdivided into as many as 200 depth bins, giving vertical resolution of about 1.3-1.5 m for our case. However, the interpolation of the surface peak position is not performed, nor is it possible in post-processing, since no raw data is recorded in BT mode.

On the other hand, even though the vertical resolution of raw WT echo amplitude is lower (4 m in our case), fitting the shape of the surface peak, described in section 3.2, allows better resolution than BT. The additional advantage of the WT method of surface range estimation over BT is its ability to measure the distance not only to the ice surface, but to the water-air interface as well. The distances from the instrument to the open-water surface obtained using the WT method aid the calibration of ice-draft estimates (see sections 3.5.3 and 4).

The ADCPs used in our moorings were among the first self-contained units to record bottom-tracking information. As a result, a direct comparison of the BT and WT methods of surface ranging is possible during the ice-covered period (Jan – May). In general, the two methods of range estimate agreed over a wide range of temporal scales (Fig. 5.12), with squared coherence over 0.75 (coherence > 85%) in the sub-tidal frequency range (Fig. 5.12b). For the most energetic tidal bands, the squared coherence reached 0.98. The noise level at time scales shorter than 6 hours was noticeably higher in the BT record. At the highest resolvable frequency the noise energy of the BT range estimate exceeded that of the WT estimate by a factor of 3. The mean difference between the raw unfiltered WT and BT range estimates was 14 cm. Filtering described in the previous section reduces this difference to 10 cm, which is still statistically significant.

The variance of ADCP range estimate exceeded that of the pressure-derived depth by a factor of 5 in the subtidal band, and up to a factor of a 100 at higher frequencies (Fig. 5.12a). On the other hand, energies in the tidal bands obtained with all three methods were identical. Higher variance of ADCP range estimate can be explained by a number of surface factors not reflected in the bottom pressure record. Ice cover topography is obviously one of such factors. Others may include short-period surface waves whose pressure signature decays significantly with depth, as well as variation of surface scattering that introduces a variable bias in ADCP surface ranging (see section 3.5.3).

We conclude that the quality of the WT and BT range estimates are comparable, and the ice-profiling technique described herein can be performed with installations

lacking BT capabilities as well. With the BT mode enabled (as in our setup), each ping provides 8 independent estimates of range *h,* which can be used to improve the statistical stability of ice draft estimate.

3.5 Corrections and errors

The ice draft is estimated as a difference between the water depth derived from the bottom pressure and the distance to the ice surface, measured by the ADCP (25). Each of these distances is several orders of magnitude greater than the expected ice draft, so even small errors in either of the range measurements drastically affect the accuracy of the resulting ice draft estimate. Consequently, the influence of the external factors on the right-hand side terms of (25) should be eliminated as accurately as possible.

An offset of over a meter between the raw range estimates based on ADCP and pressure data can be seen even during the OW conditions, when it cannot be explained by the ice presence (Fig. 5.11a). Several factors are expected to contribute to this offset. Sound speed variations throughout the thermocline is a major uncertainty that can potentially lead to a few percent error in ADCP range estimates, which translates to a few meters over 100 m range. As was shown in sections 3.1.1 and 3.1.2, substantial range biases (>1%) can also result from a finite width of the ADCP beam and the signal pre-processing procedures. Pressure record is affected by atmospheric pressure changes typically corresponding to a fraction of a meter depth offset. Additionally, the instrument tilt, misalignment, and sensor separation can also contribute to the difference between the range estimates. The following sections

quantify the effects of these factors on range estimate and outline the procedures used to eliminate or reduce them.

3.5.1 Pressure corrections

The Digiquartz pressure transducer has an accuracy of 0.01% (1 cm at 100m). It was calibrated before and after the cruise. The difference between the two calibrations of the pressure sensor was low (0.04%). We distributed the correction linearly throughout the record.

According to NCEP meteorological reanalysis, atmospheric pressure at the mooring site varied with an amplitude of about 0.2 dbar (corresponding to 20 cm of surface height). This variability was removed from the bottom pressure data prior to calculation of depth *H*. Time series of 4-times daily NCEP sea level pressure interpolated to the location of the moorings were used.

The instruments were turned on several weeks before the deployment. Consequently, the pressure record measured by the instruments on deck prior to deployment can be matched with the NCEP data to eliminate the systematic difference between these datasets (Fig. 5.13). The mean offset between the two records over a period of 1 day before the deployment was on the order of 0.1 dbar (10 cm of water column). This was subtracted from the measured bottom pressure data. Time series of measured pressure corrected this way coincided well with the NCEP record after the instruments were recovered (Fig. 5.13), suggesting that neither record drifted significantly over the 9-month deployment period.

3.5.2 Sound-speed corrections

The BT range as well as the WT bin positions reported by the instrument are calculated using the speed of sound c_{ADCP} based on the data of the instrument's low accuracy temperature sensor and fixed salinity. A more accurate estimate of sound speed at the bottom c_b was obtained using the CTD record of bottom temperature and salinity (Fig. 5.14). The difference between c_b and c_{ADCP} was generally less than 1.5 m/s (0.1%).

More importantly, the temperature and salinity changes in the thermocline lead to the vertical variation of sound speed by almost 2% (Fig. 5.15). The situation is further complicated by seasonal changes of surface layer temperature, evident from the satellite observations of sea surface temperature (Fig. 5.16). Vertical temperature and salinity profiles were measured before the deployment (Fig. 5.15a), but not during the experiment. We assume that the general shape of these profiles remained invariant during the experiment, but that the thermocline became less pronounced as the surface cooling progressed. A time-varying "thermocline strength" factor r can be derived as

$$r(t) = \frac{T_S(t) - T_b(t)}{T_{S,0} - T_{b,0}}, \tag{34}$$

where $T_b(t)$ is the bottom temperature measured by the mooring's CTD, $T_s(t)$ is the surface temperature, approximated by an exponential fit of the satellite SST data (Fig. 5.16), and $T_{b,0}$ and $T_{s,0}$ are the bottom and surface temperatures measured during the pre-deployment survey. Evolution of vertical profiles of water properties can then be approximated as following (using the temperature profile $T(z,t)$ as an example):

$$T(z,t) = T_b(t)+r(t)(T_0(z)-T_{b,0}). \quad (35)$$

Several profiles of sound speed calculated from temperature and salinity profiles approximated using (35), are shown in Fig. 5.15b. Even though this is just a model, it captures the gradual erosion of the warm surface layer, which is presumably the predominant feature.

Once the vertical sound speed profiles $c(z)$ have been reconstructed, the original ADCP range estimates h can be corrected:

$$h_c=(c_{eff}/c_{ADCP})h_p, \quad (36)$$

where h_p is the surface range corrected for signal pre-processing bias as described in the previous section, h_c is the surface range additionally corrected for sound speed variations, and c_{eff} is the effective sound speed given by

$$c_{eff} = H\left(\int_0^H c(z)^{-1}\,dz\right)^{-1}. \quad (37)$$

As the sound speed varies only by a few percent, we can expand it about its bottom value c_b: $c=c_b+c'$, where c' is a small depth-dependent correction. Then

$$c_{eff} = H\left(\int_0^H (c_b+c')^{-1}\,dz\right)^{-1} \approx c_b H\left(\int_0^H \left(1-\frac{c'}{c_b}\right)dz\right)^{-1} = c_b\left(1-\frac{\overline{c'}}{c_b}\right)^{-1} \approx c_b+\overline{c'} = \overline{c}, \quad (38)$$

where the overbar denotes a vertical average, so that $\overline{c} = \frac{1}{H}\int_0^H c(z)dz$. Consequently, a simple mean vertical sound speed $\overline{c}$ can be used instead of the harmonic mean (37). The inaccuracy of such substitution for a typical sound speed profile (Fig. 5.15b) is less than 0.1 m/s (<0.01%).

The effective sound speed obtained from (34), (35), and (38) differs from c_b by less than 0.5% (Fig. 5.17). This value is based on a relatively crude first-guess assumption of constant mixed layer depth. The uncertainty of c_{eff}, resulting from such assumption, can be estimated by considering two extreme cases: the bottom value of sound speed c_b extending to the surface (no mixed layer) and the surface value c_s extending to the bottom (deep mixed layer). The effective sound speed is consequently expected to lie between c_b and c_s, so that its maximum deviation from c_b is less than 2% (Fig. 5.17). The effects of changing mixed layer depth are not addressed in this study due to the lack of water column data. It should be noted, that in winter when the water column is homogeneous, sound speed at the surface is 0.13% lower than at the bottom due to the pressure effects (Fig. 5.17). However, since in this case sound speed variation with depth is known, c_{eff} can be obtained with good accuracy.

3.5.3 Beamwidth correction

As was shown in section 3.1.1, the finite width of an ADCP beam leads to the decrease in the effective beam angle and, consequently, to a negative bias in surface range estimate. This bias was corrected by accounting for the difference between the effective and nominal beam angles θ_{eff} and θ_0:

$$h_b = \frac{\cos\theta_{eff}}{\cos\theta_0} h_c, \tag{39}$$

where h_c is the surface range corrected for sound speed as described in the previous section, h_b is the range estimate additionally corrected for the beamwidth bias. For OW conditions, θ_{eff} is estimated using the model described in section 3.1.1. No in situ wind measurements were available for our experiment. Satellite scatterometer observations

were considered as a potential source of wind data. The QuickSCAT wind data generally agreed with NCEP reanalysis record for the mooring locations (not shown), but had significant gaps of coverage. Consequently, the 4-times-daily NCEP wind data were used, even though such a dataset is not well suited for characterization of local sea surface roughness. The same algorithm was used to compute θ_{eff} for IC conditions, but a constant W=10 m/s was used to approximate the roughness of new ice. Computed values of θ_{eff} used for the beamwidth correction are shown in Fig. 5.18. The mean effective beam angle was 19.2° during in autumn (September – December) when the average wind speed was 8 m/s. During the spring OW period (May-June), the mean value of θ_{eff} was slightly lower (19.0°) due to the weaker winds (5 m/s). During the ice-covered period the effective beam angle was set to 19.43°.

3.5.4 ADCP tilt, misalignment and instrument offset corrections

The distances to the surface measured by 4 beams may be different because of the instrument tilt. The RDI ADCPs have pitch and roll sensors, which theoretically can be used to correct for such tilt. In practice, however, accuracy of these sensors is insufficient. We used the distances to the open water surface h_i (i=1..4), obtained using the WT method for each of the 4 ADCP beams, to infer the actual instrument roll φ_r and pitch φ_p as follows:

$$\varphi_r = \arctan\left(\frac{h_1 - h_2}{h_1 + h_2}\right) / \tan\theta_0;$$
$$\varphi_p = \arctan\left(\frac{h_4 - h_3}{h_4 + h_3}\right) / \tan\theta_0, \tag{40}$$

where θ_0 is the nominal angle of ADCP beams to the vertical. (θ_0=20º for the RDI Workhorse instruments we used.) Here we use the convention of roll angle being positive when transducer #2 is higher than transducer #1, and pitch angle being positive when transducer #3 is higher than transducer #4 [*Gordon*, 1996]. After the tilt angles are determined, the ranges estimated using both BT and WT should be updated as follows:

$$h_{1\varphi} = h_1 \frac{\cos(\theta_0 + \varphi_r)}{\cos\theta_0}; h_{2\varphi} = h_2 \frac{\cos(\theta_0 - \varphi_r)}{\cos\theta_0};$$
$$h_{3\varphi} = h_3 \frac{\cos(\theta_0 - \varphi_p)}{\cos\theta_0}; h_{4\varphi} = h_4 \frac{\cos(\theta_0 + \varphi_p)}{\cos\theta_0}. \tag{41}$$

Range estimates h_i used in (40) and (41) should be already corrected for signal pre-processing, sound speed variation and finite beamwidth biases using (36) and (39), but the subscript "*b*" has been omitted for brevity.

Mean values of φ_r and φ_p inferred for the ice-free period were 0.63±0.10° and 0.27±0.08º correspondingly. For the comparison, roll and pitch values reported by ADCP sensors were 1.03±0.01º and 0.19±0.01º.

If the geometry of the instrument were perfect, all corrected range estimates $h_{i\varphi}$ would be equal on average. In our installation, however, mean OW values of $h_{1\varphi}$ and $h_{2\varphi}$ differed from the mean values of $h_{3\varphi}$ and $h_{4\varphi}$ by 14 cm, which is a statistically significant difference at a confidence level close to 100%. Consequently, we suspect that the transducer head of our instrument was slightly misaligned. A beam

transformation matrix stored in the instrument's memory is supposed to reflect such misalignment, however the matrix recorded in the log-files did not show any deviations from perfect configuration.

Range corrections due to the beam misalignment can be obtained in a procedure similar to the one used to determine pitch and roll angles above. We assume that the "true" range estimates h_i^* for the i-th beam are related to the tilt-corrected ranges $h_{i\varphi}$ as

$$h_i^* = Q_i h_{i\varphi}, \tag{42}$$

where Q_i are correction coefficients such that all $< h_i^* >$ are equal to each other. (Angled brackets indicate averaging over a clear OW period when the surface is more likely to be flat.) The Q_i are found by minimization of the sum of squares of mutual differences

$$F = \sum_{i,j} < \left(h_i^* - h_j^*\right)^2 > = \sum_{i,j} < \left(Q_i h_{i\varphi} - Q_j h_{j\varphi}\right)^2 > . \tag{43}$$

Minimization criteria

$$\frac{\partial F}{\partial Q_i} = 3Q_i < h_{i\varphi}^{\,2} > - \sum_j Q_j < h_{i\varphi} h_{j\varphi} > = 0 \tag{44}$$

lead to the system of equations

$$\begin{bmatrix} 3S_{11} & -S_{12} & -S_{13} & -S_{14} \\ -S_{12} & 3S_{22} & -S_{23} & -S_{24} \\ -S_{13} & -S_{23} & 3S_{33} & -S_{34} \\ -S_{14} & -S_{24} & -S_{34} & 3S_{44} \end{bmatrix} \begin{bmatrix} Q_1 \\ Q_2 \\ Q_3 \\ Q_4 \end{bmatrix} = 0 , \tag{45}$$

where $S_{ij} = < h_{i\varphi}\ h_{j\varphi} >$. The system is degenerate so an infinite number of solutions differing by an arbitrary multiplier can be found. We additionally require all Q_i to be

close to 1, thus selecting a minimal correction. The last criterion is equivalent to minimization of

$$G = \sum_i (Q_i - 1)^2 . \tag{46}$$

If Q_{i0} is an arbitrary solution of (45), then (46) is minimized by $Q_i = q\, Q_{i0}$, where q is given by

$$q = \frac{\sum_i Q_{i0}}{\sum_i Q_{i0}^{\,2}} . \tag{47}$$

Using (45) and (47), we found the optimal eam misalignment correction coefficients $Q_{1,2}$= 0.9993 and $Q_{3,4}$=1.0007. The correction is small, but it eliminates the difference between the mean OW range estimates.

It should be noted that the correction for instrument tilt and misalignment could be done in one step, using the range estimates h_{ib} not corrected for the tilt instead of $h_{i\varphi}$ in (42). In that case Q_i would also include tilt correction. There are two reasons these corrections should be treated separately: first, the instrument may be perfectly aligned and the relatively complicated procedure of determining Q_i will not be needed; second, instrument tilt correction must be performed separately in the case of non-fixed moored installations, since no time variation of Q_i is allowed. Even though instrument tilt and beam misalignment corrections are derived using only WT data, they were also used to correct BT range estimates.

The distances measured by the ADCP are referenced to the centers of its transducers. Since in our installation the pressure sensor was located 23 cm lower (Fig. 5.1b), this offset has also been taken into account.

4 Discussion

All the corrections described above total to a mean offset of –0.73 m (Table 5.1, Fig. 5.19). The aggregate correction varies in time with standard deviation of 0.25 m, chiefly due to the changes in surface roughness and atmospheric pressure. Despite all the corrections applied, the resulting ice draft (or, in OW case the difference between the distances to the surface derived from pressure sensor and ADCP) exhibits a noticeable positive offset of 0.5-1 m at both locations (Fig. 5.20). This offset is likely due to the hardware signal pre-processing bias (section 3.1.2) as well as inaccuracies in the beamwidth and sound-speed corrections. Presently, we consider this offset uncorrectable due to insufficient knowledge of the surface roughness, vertical sound speed profile and the parameters of hardware signal processing.

Similar uncorrectable offsets pose a serious problem in the analysis of specialized ice-profiling sonar data [*Melling et al.*, 1995], since even less information about the evolution of vertical profile of sound speed than in our case is typically available. This problem is usually circumvented by using the areas of open water passing over the mooring for establishing a "zero-draft" reference. Unfortunately, no open water was observed at the location of our moorings from mid-January to May 2000. The only reliable estimate of zero-draft (dashed lines in Fig. 5.20a) is available for the end of December, prior to ice cover establishment. The OW period immediately following the spring melt was also used, even though the apparent draft varied greatly during that time and the reliability of the spring estimate of zero-draft is questionable. Straight-line interpolation had to be used between these two reference periods. Ice-draft

estimates at the eastern mooring appear to be more consistent with a linear approximation of zero-draft (Fig. 5.20a).

Taking the zero-draft reference into account, typical ice drafts observed at the western and eastern moorings were 0.2-0.6 m and 0.3-0.8 m correspondingly (Fig. 5.20b). Mean January-May values were 0.38 m and 0.59 m correspondingly. A maximum ice draft of 1.5 m was observed at both the western and the eastern moorings just before the disappearance of the ice cover in May and June correspondingly. Such relatively low ice thicknesses are typical for the Okhotsk Sea, especially taking into account that the moorings were located within the polynya region [*Shcherbina et al.*, 2004; *Fukamachi et al.*, 2003; *Birch et al.*, 2000]. Unfortunately there are no concurrent direct observations of ice thickness in the northern Okhotsk Sea against which our estimates can be compared.

Another ice characteristic that can be derived from ADCP draft estimates is a measure of surface roughness. As mentioned earlier (see section 3), each ADCP ping provides 4 (8 in the presence of BT) estimates of ice draft. Due to the ADCP beam spreading, these estimates correspond to 4 points of a cross pattern on the ice surface. Horizontal separation of opposing beam footprints was 79 m and 103 m for the western and eastern mooring correspondingly. Consequently, the difference between the maximum and minimum draft estimates at each ping (Fig. 5.20c) can be used to characterize variability of surface topography at 50-100 m horizontal length-scale. As expected, the surface of ice is much more variable than open water surface, with a typical draft variability of 0.5-1 m. Early in the ice-covered period (February), the ice surface at the western site appears to be less rough than at the eastern one, consistent

with the polynya conditions inshore [*Shcherbina et al.*, 2004]. Later in the season the ice roughness at the two mooring sites is comparable. The apparent roughness scale of the open water surface in September-December was 0.2 m at both locations. This value is comprised of sea-surface height variability due to long-period waves and the noise in range estimates. Consequently, we assume that the upper limit of error in the ADCP draft estimate is on the order of 0.1 m.

5 Conclusions

Ice draft profiling with standard bottom moored ADCPs is possible, provided that bottom pressure is measured accurately at the same location. Ice draft is measured as the difference of the instrument depth derived from the pressure record and the distance to the lower ice surface measured with ADCP. The latter estimate is obtained by fitting a modified Gaussian profile to the vertical profile of echo amplitude that exhibits a prominent peak due to surface reflection. Gaussian peak width and height as well as its deviation from observed data can be used for quality control of the range estimate. Such "water tracking" method provides 4 estimates of distance to the surface per ping (for 4-beam instruments). These estimates are inherently noisy, and need to be filtered for incorrectly detected peak locations. Additionally, corrections for atmospheric pressure, sound speed variation, finite beamwidth, instrument tilt, beam misalignment, and vertical sensor offset need to be applied. Instrument tilt and beam misalignment corrections can be determined using the water-tracking results during the open-water period. On the other hand, atmospheric pressure, sound-speed, and beamwidth corrections need to be determined based on external data. This class of corrections poses a significant challenge, since their effect on draft estimate is most

pronounced (adding up to over 1.5 m in our experiment), while the external parameters used to derive these corrections are poorly known (see sections 3.5.2 and 3.5.3). The resolution of the final draft estimate is on the order of 0.1 m, but large unexplained positive biases exist in both our datasets. Hardware signal processing may be potentially responsible for a large part of this bias. The exact value of the signal processing offset is difficult to obtain due to insufficient information regarding the filtering procedure. The relative importance of such bias is expected to be less in the regions of thicker ice cover.

Based on the present analysis of the factors, contributing to the errors and biases in estimating ice draft from an ADCP, the following recommendations can be offered for future experiments intending to use moored ADCPs for ice profiling:

1. The relatively wide sloping beam of an ADCP is a handicap for ice profiling, as the resulting bias is large and variable. Better understanding of the influence of surface roughness on the shape and location of the surface echo amplitude peak, as well as better parameterization of such roughness is necessary for reliable draft estimation.
2. The effect of hardware signal pre-processing may be large (on the order of 1 m), but its exact magnitude and dependence on surface conditions are unknown. Further investigation of the ADCP hardware is necessary to accurately correct for such effect.
3. Bottom tracking mode (BT) is not necessary for ice profiling, as water-tracking (WT) is capable of measuring the distance to the surface with better accuracy.

4. The vertical bin size of 4 m used in our installation resulted in a surface echo amplitude peak spanning about 5-10 bins, which is sufficient for modified Gaussian profile fitting. However higher vertical resolution can greatly increase the reliability of such a fit and the overall accuracy of the method. Data storage constraints which typically limit the resolution of long-term deployments, including our case, are becoming progressively less important in modern instruments.
5. An accurate surface pressure record close to the ADCP is greatly preferred. In the absence of such record (as in the case of our experiment), large-scale reanalysis pressure data may be used for atmospheric pressure correction. However, the effects of such substitution are difficult to predict. In either case, extending the mooring pressure record several days before the deployment and after the recovery allows establishment of the surface pressure offset (see section 3.5.1).
6. As much knowledge of the evolution of the vertical sound speed profile should be obtained to allow accurate draft correction, especially in regions of unbroken ice cover.

Incorporating a dedicated ice profiler into an experiment can potentially be infeasible or impractical, especially since it may require installation of two separate moorings to avoid interference between the IPS and ADCP systems. With the use of correction procedures outlined in this study, ice-draft profiling can be expected to augment any moored ADCP observations in high-latitude conditions with little or no additional cost. Future experiments designed with the ADCP ice profiling in mind

should, however, address the weaknesses of this procedure by following the above recommendations. In that case, the accuracy of ice profiling can be potentially improved over the present 10-cm baseline.

Acknowledgements: This work was supported through the National Science Foundation OCE-9811958 and by Hokkaido University (ship support). Technical support was provided by the Oceanographic Data Facility and the Instrument Development Group at Scripps Institution of Oceanography (SIO), and by the captain and crew of the R/V Professor Khromov. We thank Martin Visbeck, Peter Spain, and Steve Maier for stimulating discussion.

References:

Birch, R., D. Fissel, H. Melling, K. Vaudrey, K. Schaudt, J. Heideman, and W. Lamb, Ice-profiling sonar., *Sea Tech.*, 41, 48-52, 2000.

Chapman, R. P. and H. D. Scott, Backscattering strength of young sea ice, *J. Acoust. Soc. Am.*, 36, 2417-2418, 1964a.

Chapman, R. P. and H. D. Scott, Surface backscattering strengths measured over an extended range of frequencies and grazing angles, *J. Acoust. Soc. Am.*, 36, 1735-1737, 1964b.

Cox, C. and W. Munk, Measurement of the roughness of the sea surface from photographs of the sun's glitter, *J. Opt. Soc. Am.*, 44, 838-850, 1954.

Fukamachi, Y., G. Mizuta, K. I. Ohshima, H. Melling, D. Fissel, and M. Wakatsuchi, Variability of sea-ice draft off Hokkaido in the Sea of Okhotsk revealed by a moored ice-profiling sonar in winter of 1999, *Geophysical Research Letters*, 30(7), 1376, doi:10.1029/2002GL016197, 2003.

Gordon, R. L., *Acoustic Doppler Current Profilers Principles of Operation: A Practical Primer.*, RD Instruments, 1996.

Macpherson, J. D., The effect of ice on long range underwater sound propagation, *J. Brit. IRE*, 26, 293-297, 1963.

Melling, H., Sound scattering from sea ice: aspects relevant to ice-draft profiling by sonar, *J. Atmos. Oceanic Technol.*, 15, 1023-1034, 1998.

Melling, H., P. Johnston, and D. Riedel, Measurements of the underside topography of sea ice by moored subsea sonar, *J. Atmos. Oceanic Technol.*, 12, 589-602, 1995.

Shcherbina, A. Y., L. D. Talley, and D. L. Rudnick, Dense water formation on the northwestern shelf of the Okhotsk Sea. Part I: direct observations of brine rejection, *J. Geophys. Res.*, in press, 2004.

Urick, R. J., The process of sound scattering at the ocean surface and bottom, *J. Mar. Res.*, 15, 134, 1956.

Urick, R. J., Principles of underwater sound, McGraw-Hill, New York , 1975.

Visbeck, M. and J. Fischer, Sea surface conditions remotely sensed by upward-looking ADCPs, *J. Atmos. Oceanic Technol.*, 12, 141-149, 1995.

Visbeck, M., Deep velocity profiling using lowered acoustic Doppler current profilers: bottom track and inverse solutions, *J. Atmos. Ocean. Tech*, 19, 794-807, 2002.

Tables and figures:

Correction	Mean offset (m)	Standard deviation (m)
Atmospheric pressure	0.01	0.07
Pressure offset	-0.07	0
Beamwidth	-0.47	0.18
Sound speed	0.03	0.13
Sensor offsets	-0.23	0
Total:	-0.73	0.25
Signal pre-processing*	-0.98	0.10

Table 5.1 Magnitudes of the corrections applied to the ice draft estimated from ADCP data. * Estimated signal pre-processing bias is included for reference only; no correction for this bias was performed (see section 3.1.2).

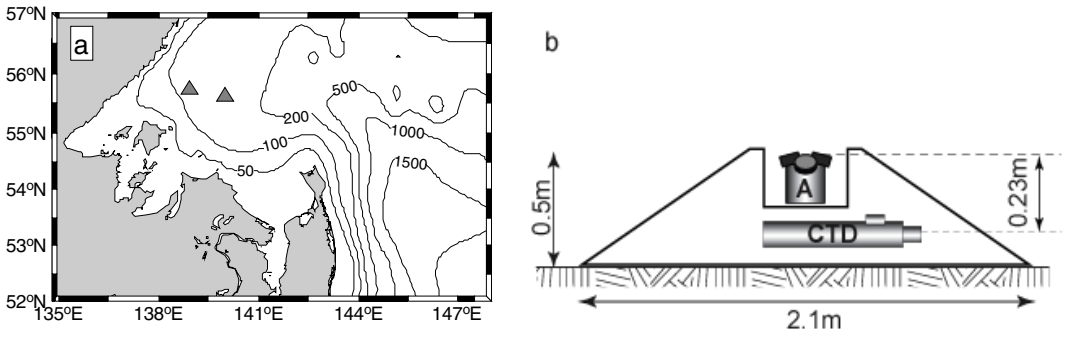

Fig. 5.1 (a) Map of northwestern Okhotsk Sea showing the mooring location (triangles). (b) Schematics of bottom moorings, showing the relative locations of the upward-looking ADCP (A) and the CTD package within the conical hull of a mooring.

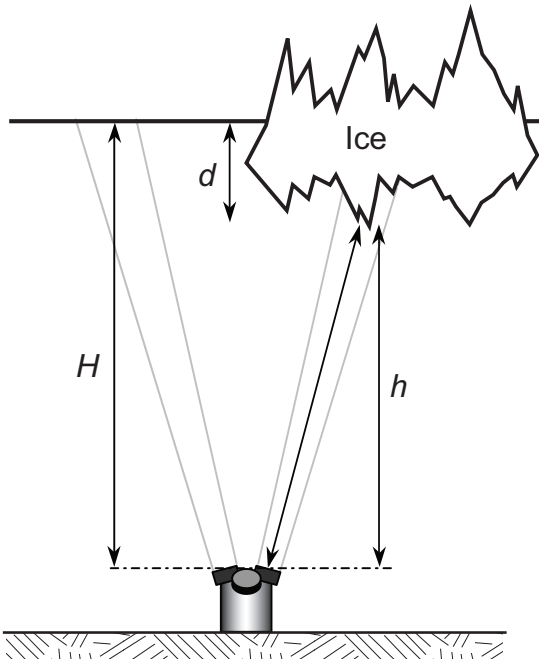

Fig. 5.2 Schematics of ADCP ice draft profiling.

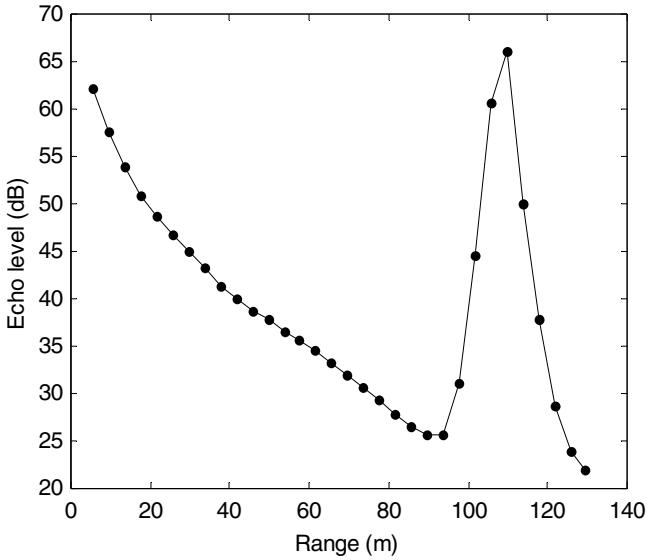

Fig. 5.3 Typical profile of ADCP echo level as a function of distance above the instrument. Water depth is approximately 110 m.

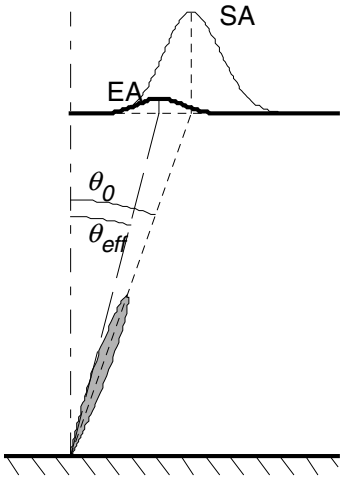

Fig. 5.4 Schematics of the beamwidth bias origination. Emission pattern of an ADCP beam (shaded) has a finite beamwidth, resulting in a relatively wide insonified footprint on the surface. Reflection form the inner edge of the footprint is stronger (see text for details), so the echo intensity distribution (EA) is shifted relative to the distribution of the incoming sound intensity (SA). As a result, the effective beam angle θ_{eff} is smaller than the nominal beam angle θ_0. Beamwidth is exaggerated by a factor of 2 for clarity, and the effect of sidelobes is neglected.

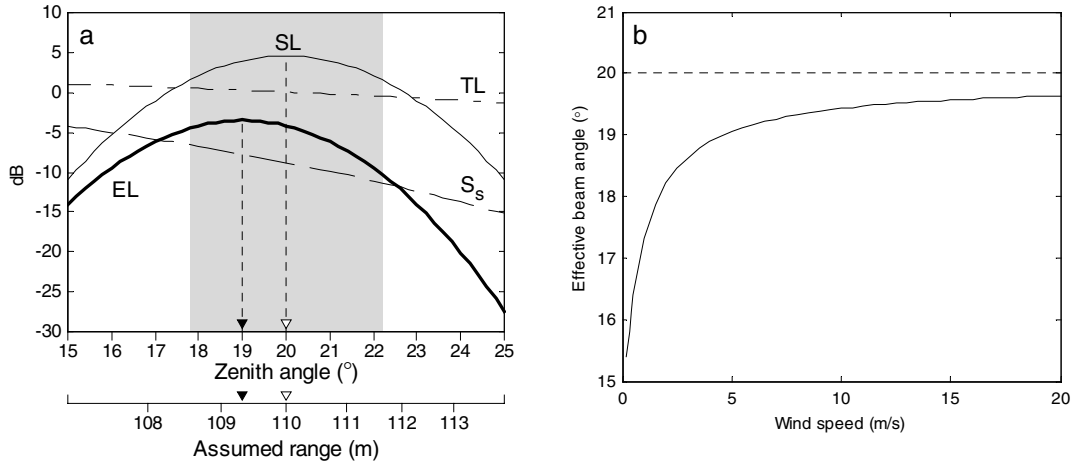

Fig. 5.5 Model of beamwidth bias. (a) Distribution of source level (SL), transmission loss (TL), surface scattering strength (S_s), and echo level (EL) across the ADCP beam in meridional direction (beamwidth, defined by -3 dB drop in SL is shaded). The lower horizontal axis shows the range inferred from the echo return time. Nominal beam angle and true distance to the surface are marked by white triangles. Black triangles mark the "effective beam angle", defined by the maximum echo level, and the corresponding (biased) range estimate. (b) Dependence of effective beam angle on wind speed (solid line). Nominal beam angle is shown by dashed line.

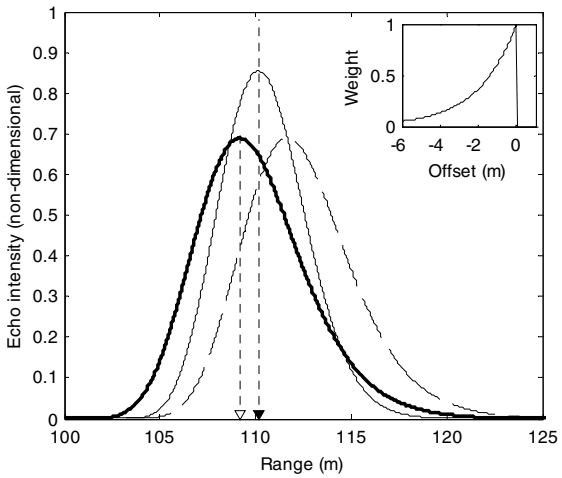

Fig. 5.6 Illustration of the effects of echo amplitude signal processing on hypothetic raw echo intensity signal (thin solid line). Results of low-pass filter application (dashed line) and subsequent shift (thick line) are shown. Time axis is converted to range for convenience. Black and white triangles show the locations of the maxima or the raw and processed signal, respectively. Insert shows the distribution of weights of RC filter (τ=2 m), applied to the signal.

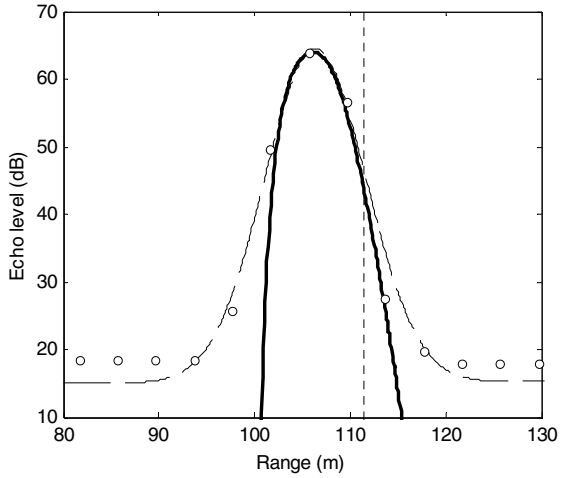

Fig. 5.7 Comparison of the modeled shape of the near-surface echo level profile (thick line) with the observed (circles). Model parameters (source level, water depth, and windspeed) were subjectively adjusted for the best fit. Vertical dotted line marks the water depth used in the model. Modified Gaussian fit is shown by dashed line.

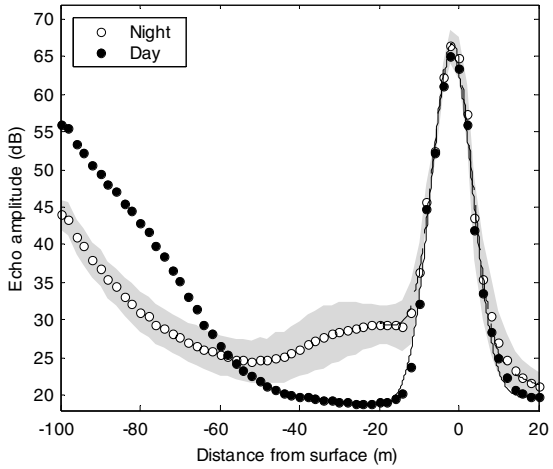

Fig. 5.8 Influence of near-surface plankton congregation on the vertical structure of echo amplitude. Profiles of echo amplitude at night (plankton-up, open circles) and at daytime (plankton-down, solid circles) are shown. One standard deviation is shown by gray shading. Thin lines show modified Gaussian approximation of the peak shape, fitted to the data using least-squares.

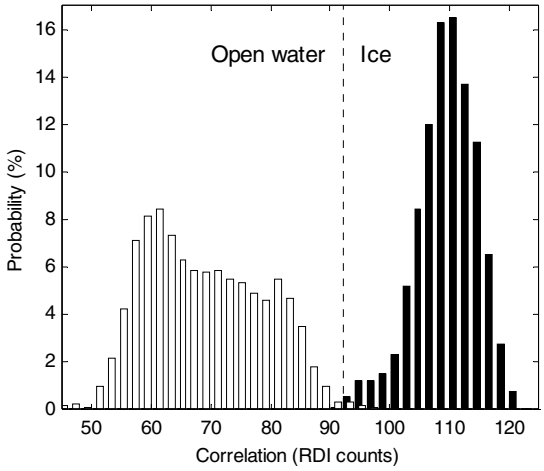

Fig. 5.9 Distribution of ADCP signal correlation during "definitely open-water" (Oct. 15 - Nov.15, open bars) and "definitely ice-covered" (Feb. 15 - Mar. 15, filled bars) periods. Vertical dotted line shows the threshold value C_{ice}. Data from the first bin above the mean sea surface level are shown.

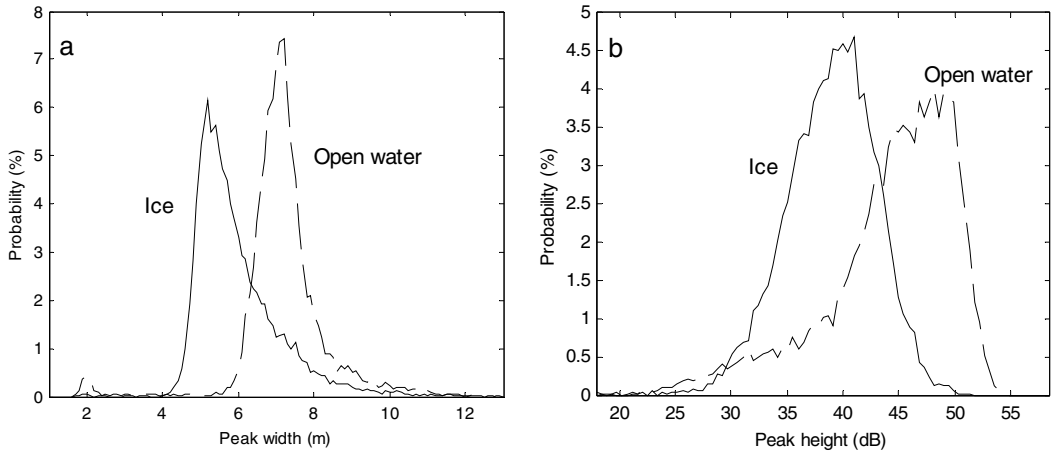

Fig. 5.10 Distribution of (a) the width and (b) the height of the surface peak for ice covered (solid line) and open water (dashed line) conditions. Ice detection is based on echo correlation.

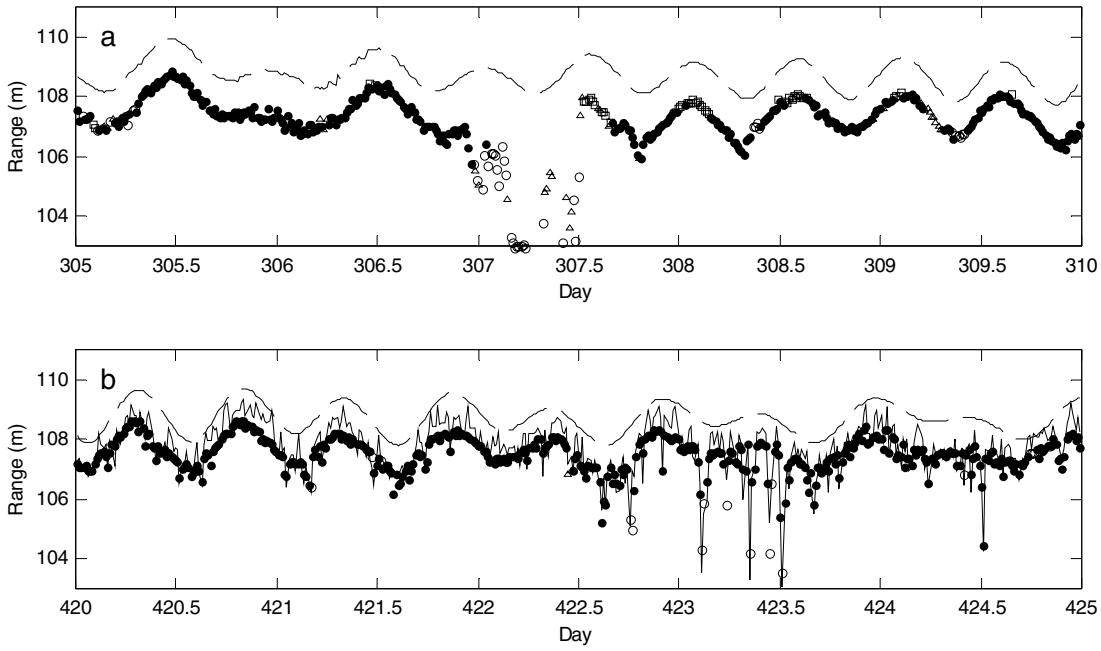

Fig. 5.11 Performance of the WT surface detection algorithm in (a) open-water (Nov. 2-7, 1999) and (b) ice-covered (Feb. 25 – Mar. 1, 2000) conditions, compared to range estimate based on bottom pressure (dashed line). Black dots mark the useable range estimates, and open symbols represent the values discarded based on peak width (open circles), peak height (open triangles), and misfit (open squares) criteria. BT range estimates are shown by thin by thin solid line when available (only in ice-covered conditions). Raw uncorrected data of beam #1 are shown.

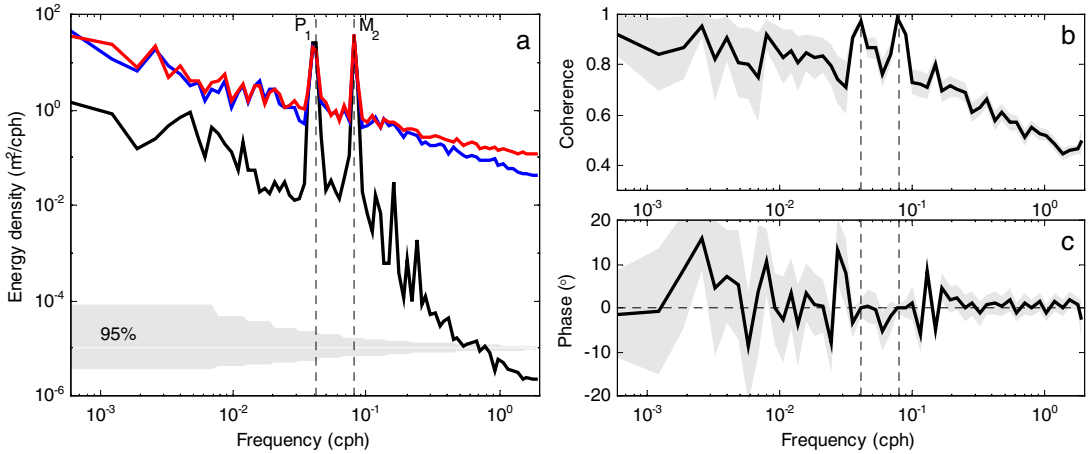

Fig. 5.12 (a) Power spectra of wintertime (January – May) range estimates based on pressure (black), water-track (blue) and bottom-track (red) data. (b) Squared coherence and (c) phase of the bottom-track and water-track range estimates over the same period. 95% confidence intervals (shading) and 2 major tidal frequencies (vertical dashed lines) are shown.

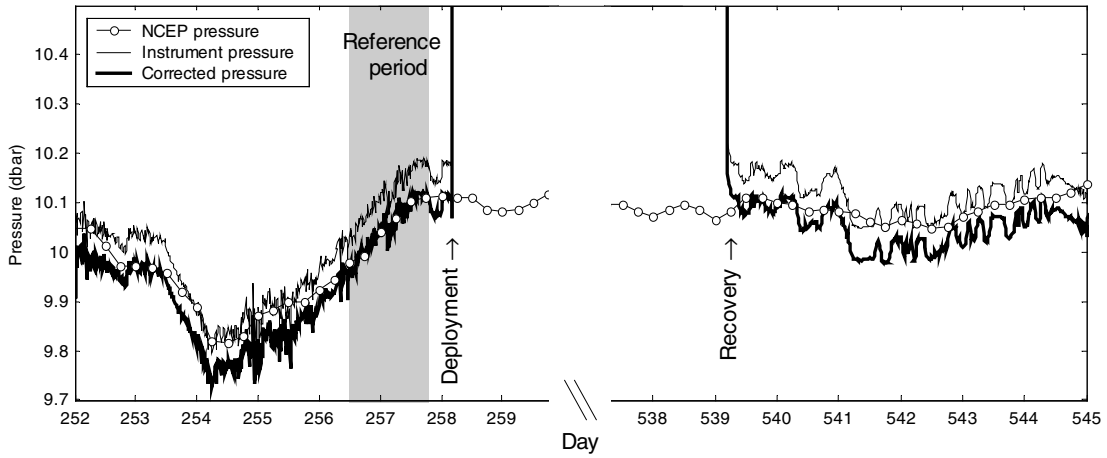

Fig. 5.13 Pressure sensor surface calibration. NCEP reanalysis sea-level pressure interpolated at the site of the mooring (open circles), raw pressure record (thin black line) and corrected pressure (thick black line) are shown. Reference period over which the offset was calculated is shown by gray shading. Periods before deployment and after recovery are shown. Significant deviation of the corrected pressure from NCEP record before day 256 and after day 541 may be due to the geographical separation of the instrument from the mooring site onto which NCEP data were interpolated.

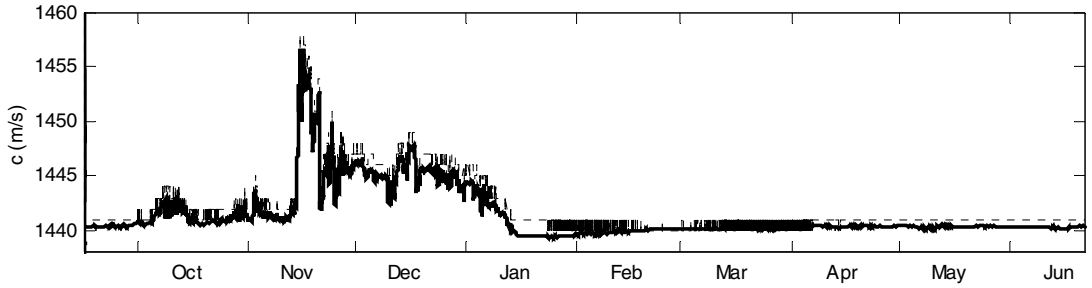

Fig. 5.14 Sound speed reported by ADCP (c_{ADCP}, dashed line) and calculated using the measured temperature and salinity (c_{b} thick solid line).

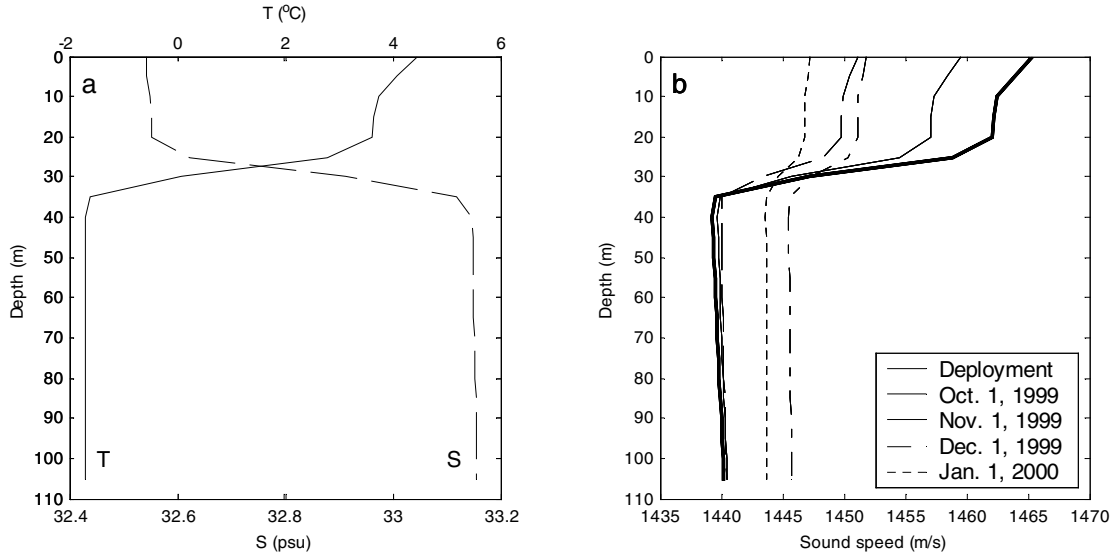

Fig. 5.15 Thermocline sound speed correction. (a) Vertical profiles of temperature (solid line) and salinity (dashed line) at the mooring site on September 16 1999. (b) Vertical profile of sound speed calculated from the temperature and salinity data for September 16 1999 (thick line) and sound speed profiles inferred using thermocline correction (thin solid and dashed lines). See text for details.

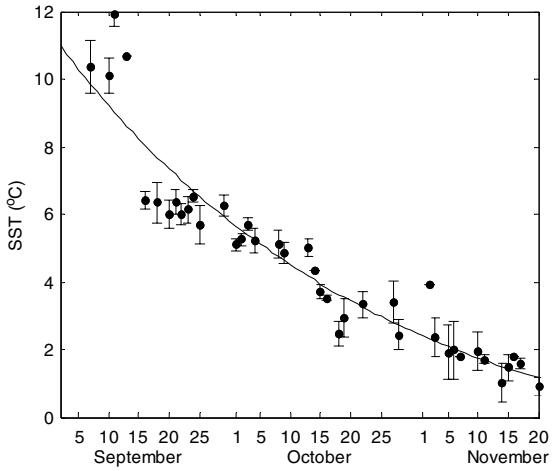

Fig. 5.16 Surface temperature calibration. Average AVHRR sea surface temperature within 20-km radius around the mooring site (dots) and one standard deviation (errorbars) are shown. Solid line shows an exponential fit to this data.

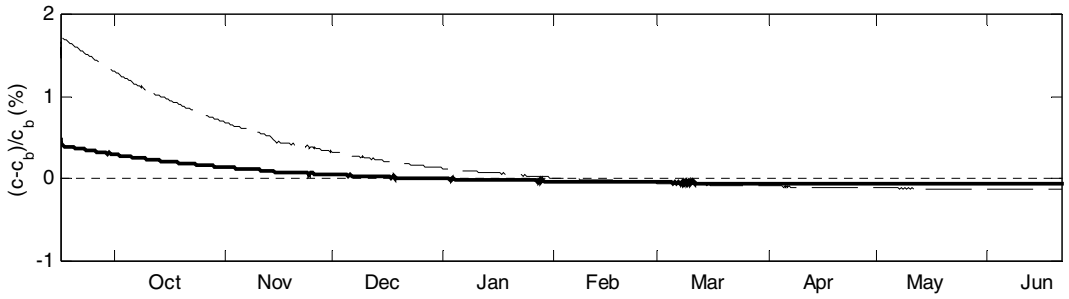

Fig. 5.17 Deviation of the effective sound speed c_{eff} (solid line) and its upper bound, given by the surface sound speed c_s (dashed line), from the bottom value c_b.

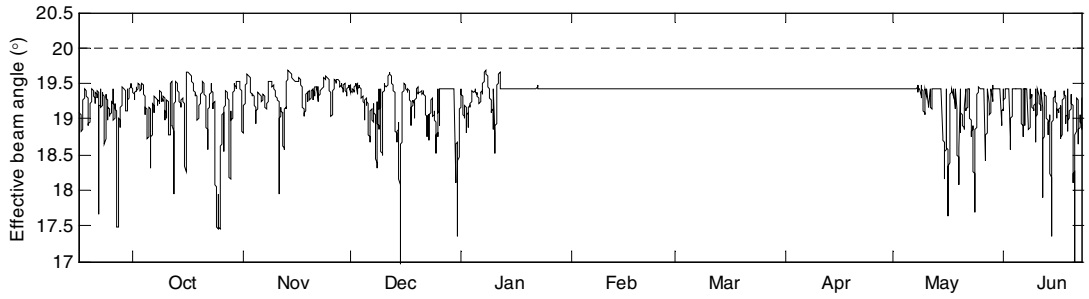

Fig. 5.18 Effective beam angle (solid line), computed using the model of beamwidth bias for the surface conditions estimated at the mooring site. Nominal beam angle is shown by dashed line.

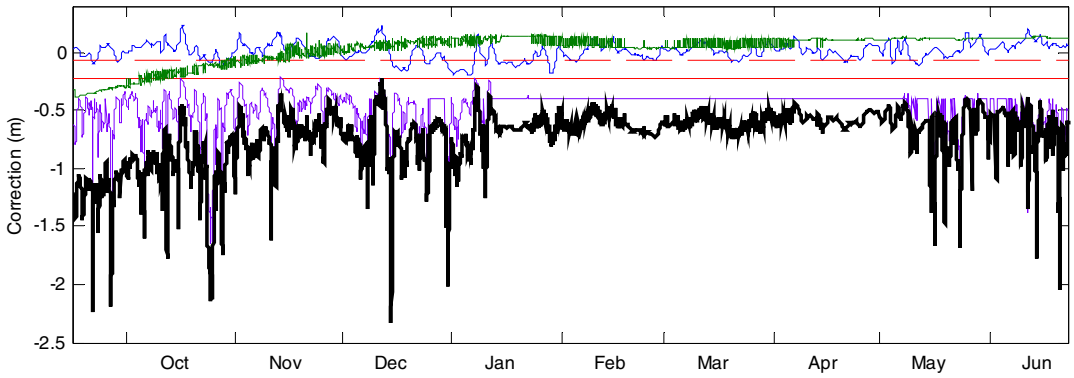

Fig. 5.19 Summary of corrections applied to the measured ADCP range. Corrections for atmospheric pressure (blue), sound speed (green), beamwidth (purple), pressure offset (red dashed line), transducer offset (solid red line) are shown, as well as the sum of all corrections (thick black line).

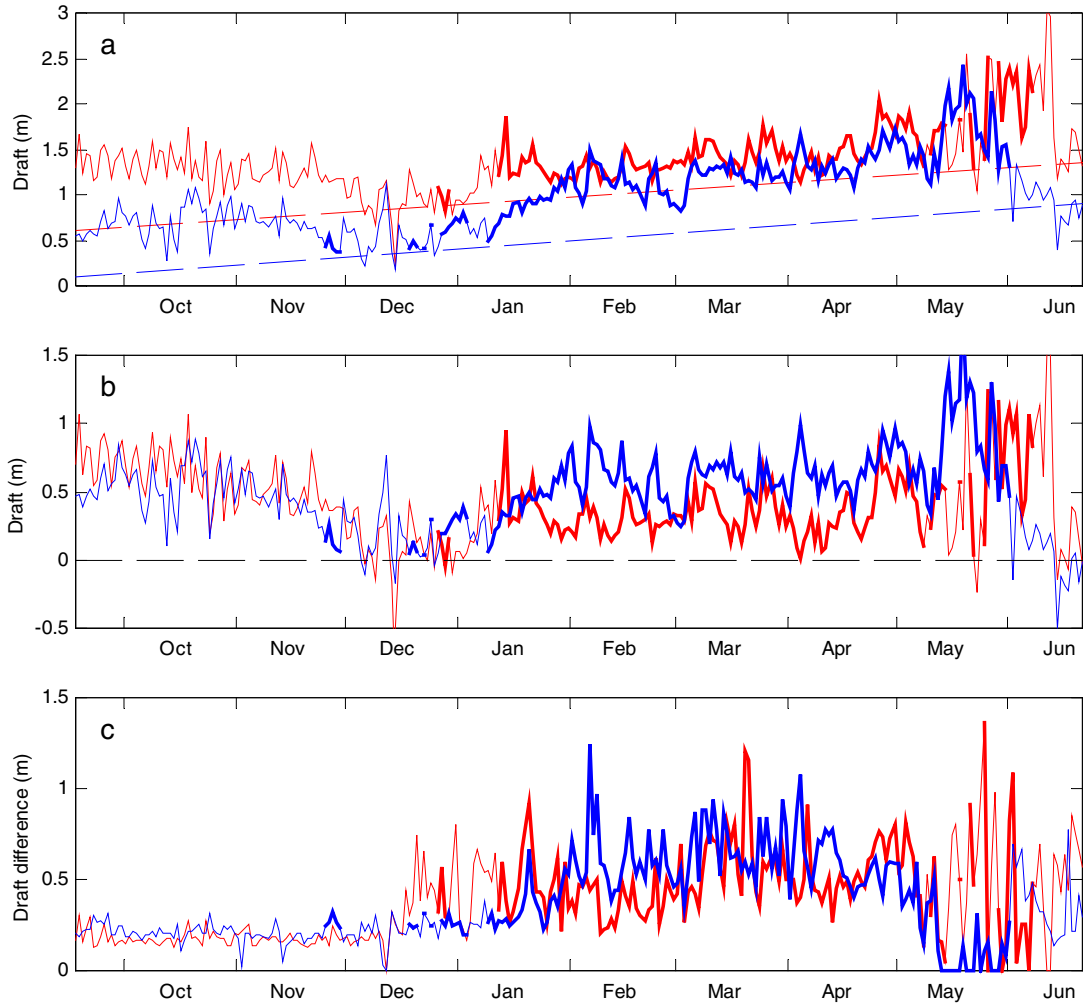

Fig. 5.20 (a) Raw ADCP ice draft, (b) ice draft relative to zero-draft estimate, and (c) surface roughness at the western (red line) and the eastern (blue line) moorings. Surface roughness is defied as the difference between the maximum and the minimum simultaneous draft, estimated using 4 ADCP beams. Daily median estimates using all beams and both WT and BT methods (where available) are plotted. Thinner lines indicate open-water conditions, determined by the echo correlation criterion. In open-water conditions "ice draft" is the difference between the distances to the surface derived from pressure sensor and ADCP. Dashed lines in (a) show zero-draft estimates for the two moorings.